Insights to structure-property relationships in ionic liquids using cyclic perfluoroalkylsulfonylimides

Younes K. J. Bejaoui,[a] Frederik Philippi,[b] Hans-Georg Stammler,[c] Krzysztof Radacki,[a] Ludwig Zapf,[a] Nils Schopper,[a] Kateryna Goloviznina,[d] Kristina A. M. Maibom,[a] Roland Graf,[a] Jan A. P. Sprenger,[a] Rüdiger Bertermann,[a] Holger Braunschweig,[a] Tom Welton,[b] Nikolai V. Ignat´ev,[a,e] Maik Finze[a]*

[a]Julius-Maximilians-Universität Würzburg, Institut für Anorganische Chemie, Institut für nachhaltige Chemie & Katalyse mit Bor (ICB), Am Hubland, 97074 Würzburg, Germany. E-mail: maik.finze@uni-wuerzburg.de

[b]Imperial College London, Department of Chemistry, Molecular Sciences Research Hub, White City Campus, London W12 0BZ, UK.

[c]Universität Bielefeld, Fakultät für Chemie, Lehrstuhl für Anorganische Chemie und Strukturchemie (ACS), Centre for Molecular Materials (CM2), Universitätsstr. 25, D-33615 Bielefeld, Germany.

[d]Sorbonne Université, CNRS, Physicochimie des Électrolytes et Nanosystèmes Interfaciaux, F-75005 Paris, France.

[e]Consultant, Merck KGaA, 64293 Darmstadt, Germany. E-mail: nikolai.ignatiev@external.merckgroup.com

Supporting Information

Table of Contents

Analytical Instruments and Details

X-Ray diffractions studies were carried out on a XtaLAB Synergy, Dualflex, HyPix diffractometer equipped using Cu-α radiation (micro-focus sealed X-ray tube, λ = 1.54184 Å) with the exception of the X-Ray diffractions study of [EMIm]**5cPFSI**. [EMIm]**5cPFSI** was examined on a Rigaku Supernova diffractometer using Mo Kα (λ = 0.71073 Å) radiation. Except for [EMIm]**5cPFSI**, all crystal structures were examined using *ShelXle*[1], [EMIm]**5cPFSI** was examined using Olex2[2]. All structures were solved with the ShelXT[3] structure solution program using Intrinsic Phasing and refined with the ShelXL[1] refinement package using Least Squares minimisation.[4, 5] All non-hydrogen atoms were refined anisotropically. Pictures of molecular structures were drawn with the program Diamond 4.6.8.[6] or CrystalExplorer Version 21.5.[7]

Cyclic voltammetry experiments were performed with a PGSTAT30 potentiostat (Metrohm Autolab B.V., Netherlands). A standard three-electrode cell configuration with Argon atmosphere was employed. The data evaluation was performed with Nova 2.0 Software. As the working electrode a ESA EE047 Glassy-Carbon electrode in glass with an inner diameter of 3 mm and outer diameter of 6 mm and an electrode area of 7.1 mm^2 was used. A RE-7 *non aqueous reference electrode* (Ag/Ag^+) out of Vycor-glas, filled with a 0.1 $mol \cdot L^{-1}$ [$n$$Bu_4N$][$PF_6$]/0.01 $mol \cdot L^{-1}$ $AgNO_3$-acetonitrile solution and a silver wire, served as reference electrode. The counter electrode was a platin wire with 5 cm length, 0.5 mm diameter and 78.7 mm^2. If not stated otherwise the ionic liquids were studied as neat liquids. The examined acetonitrile solutions of the ionic liquids had a concentration of 0.1 $mol \cdot L^{-1}$. The potential was retroactively internally referenced against ferrocene.

^1H, $^{13}C\{^1H\}$, ^{15}N and ^{19}F NMR spectra were recorded at 25 °C of acetone-d6 solutions or of neat ionic liquids with DMSO-d6 filled inlet. The NMR spectra were recorded on a Bruker Avance Neo 400, Bruker Avance III Nanobay 400 or a Bruker Avance 500 spectrometer. The NMR signals are referenced against TMS (^1H and ^{13}C), CH_3NO_2 (^{15}N) and $CFCl_3$ (^{19}F). Chemical shifts were calibrated against the residual solvent signal, respectively (δ(^1H): acetone-d6 2.05 ppm, DMSO-d6 2.50 ppm; δ(^{13}C): acetone-d6 206.26 ppm, DMSO-d6 39.52 ppm.[8]

Viscosities and densities were measured with a rolling-ball viscosimeter Lovis 2000 ME at an 60° angle in conjunction with a DMA 4100 M density meter (Anton Paar GmbH, Austria).

Thermal analyses were performed with a DSC 204 F1 Phoenix (Netzsch) in the temperature range of −180 to 500 °C with a heating rate of 10 °C · min^{-1}.

The water content of the ILs were determined by Karl-Fischer-Titration with a Metrohm 831 KF Coulometer. Elemental analysis was performed on an Elementar Varion Micro Cube analyser.

ESI mass spectra were recorded on a Thermo Scientific Extractive Plus mass spectrometer equipped with an Orbitrap mass analyser.

IR spectra were recorded at room temperature with a Bruker Alpha-FT-IR spectrometer with an apodized resolution of 4 cm^{-1} in the attenuated total reflection (ATR) mode in the region of 4000–400 cm^{-1} using a diamond crystal.

Raman spectra were recorded at room temperature on a Bruker MultiRAM FT spectrometer with an apodized resolution of 4 cm^{-1} in the region of 4000–400 cm^{-1}. The Raman samples were contained in melting point capillaries and were excited with 1064 nm line of a Nd/YAG laser.

Density functional calculations (DFT) Density functional calculations (DFT)[9] using the hybrid functional PBE0[10] and *def2*-TZVPP basis set[11] in the Karlsruhe *def2* basis set family were performed using Biovia

Tmolex 2021 (version 21.0.1) from Dassault Systèmes.[12] All ground-state structures represent true minima on the respective hypersurface with no imaginary frequencies.

MD simulations

Methods

Force field development

The CL&Pol polarisable force field[13, 14] was used for modelling ionic liquids. The $[BMPL]^+$, $[EMIm]^+$, **TFSI** ions were taken without any changes.
The force field for the new **5cPFSI** anion was based on the existing CL&P model for linear perfluoroalkanesulfonylamides (https://github.com/paduagroup/clandp).[15] The majority of non-bonded and bonded interaction parameters corresponded to that of **TFSI** anion, with some modification described below. The partial charges on the carbon atoms were set to 0.19 (C_{1F} atom type of CL&P) to guarantee an integer negative charge of the anion. The parameters for the C-C bond, S-C-C and F-C-C angles, O-S-C-C, N-S-C-C, S-C-C-F, F-C-C-F dihedrals were taken from longer perfluoroalkanesulfonylamides (such as bis(pentafluoroethylsulfonyl)imide, [**BETI**]$^-$). The coefficients of a new S-C-C-S dihedral were set to zero, since the geometry of the anion is maintained by bonds and angles of the cyclic backbone. Next, explicit polarisation effects were added in the form of Drude dipoles. Atomic polarisabilities were taken from the work of Schröder[16]. Following the CL&Pol methodology[13, 17], the non-bonded attractive interactions of the **5cPFSI** anion with the pyrrolidinium and imidazolium cations were scaled to avoid double counting of induction effects. The fragment approach was considered: $[BMPL]^+$ was composed of dimethylpyrrolidinium $[MMPL]^+$ and n-C_4H_{10} fragments, while $[EMIm]^+$ and **5cPFSI** were treated as entire ions. The scaling coefficients were similar to those with the **TFSI** anion, being equal to $k([EMIm]^+ \ldots$ **5cPFSI**$) = 0.65$, $k([MMPL]^+ \ldots$ **5cPFSI**$) = 0.77$, and $k(C_4H_{10} \ldots$ **5cPFSI**$) = 0.65$.

Simulation Setup

MD simulations for the four ionic liquids [BMPL]**5cPFSI**, [EMIm]**5cPFSI**, [BMPL]**TFSI**, and [EMIm]**TFSI** were run at 298.15 K using the LAMMPS software package as described previously.[18, 19] Briefly, we ran minimization, annealing at 600 K in NPT, box size determination over 10 loops, compression to average box size, and equilibration for 4 ns prior to production. The production runs themselves were 15 ns, with position data recorded every 1 ps. Radial, spatial and combined distribution functions were calculated using the TRAVIS software package,[20, 21] code version Jan 01 2019. In addition, we used the prealpha software package to calculate the Coulomb interaction energy, charge arm lengths and α_2 parameters. Source code, executable, input files and manual are available on Github (https://github.com/FPhilippi/prealpha).

Liquid Structure

Radial Distribution Functions

The radial distribution functions calculated using the centre of mass for the ions are shown in **Figure S1** to **Figure S3**.

In the cation-cation radial distribution functions, **Figure S1**, short contacts indicating π-stacking are observed for the $[EMIM]^+$ based ionic liquids (*cf.* subsection *Cation Cation interactions* for π-stacking).

The anion-anion radial distribution functions, **Figure S2**, reveal a tendency of the **5cPFSI** anions to produce a more well-defined liquid phase (sharper and more peaks) compared to ionic liquids with the **TFSI** anions. This is likely due to the flexibility of the latter; for a discussion of the structural motifs giving rise to these peaks see subsection *Cation Cation interactions*.

Finally, the cation-anion radial distribution functions, **Figure S3**, show well defined extrema, as expected for ionic systems. For [BMPL]**5cPFSI**, the first shell is particularly well structured (*cf.* Section 0). This is also visible in the Coulomb interaction energy, **Figure S4**. Here, the pyrrolidinium ionic liquids are more structured in the sense that they have a larger Debye length; see also reference[22].

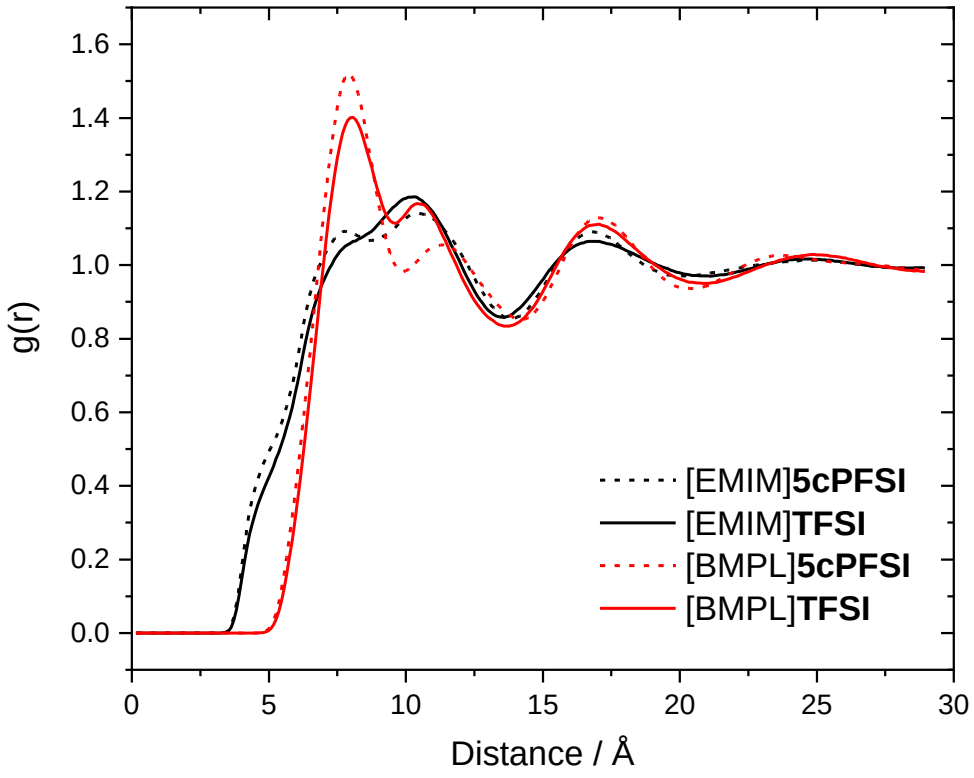

Figure S1: Cation-cation radial distribution functions.

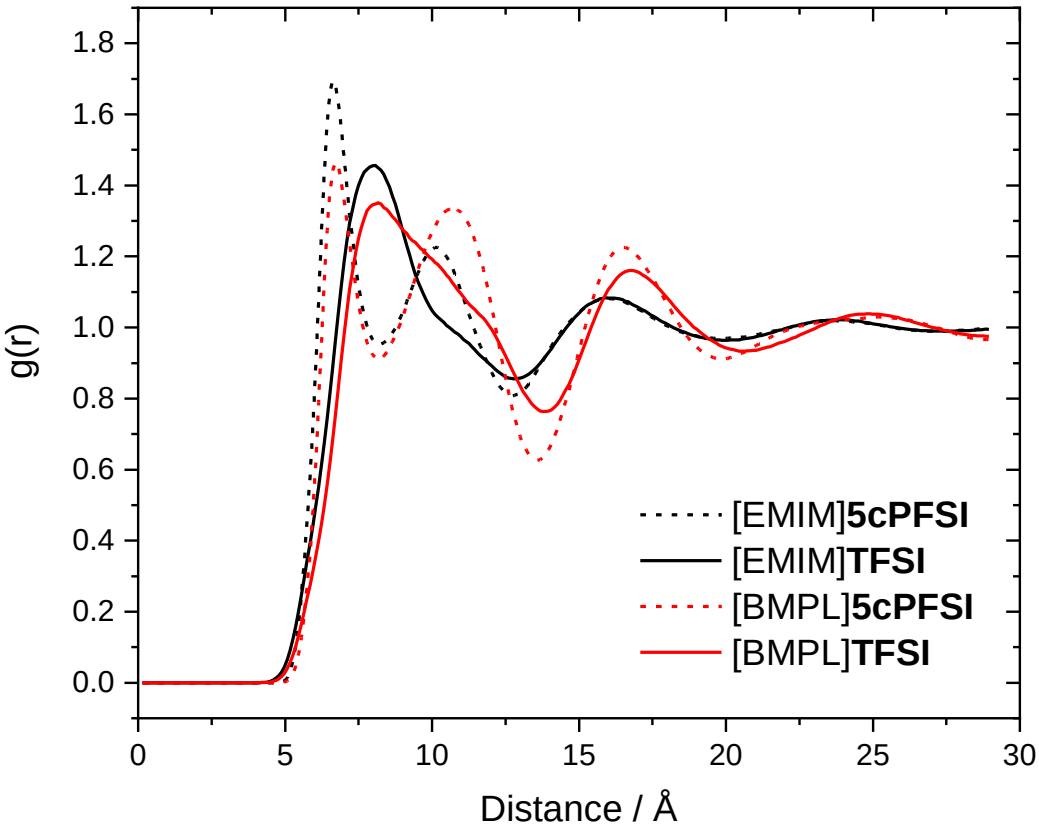

Figure S2: Anion-anion radial distribution functions.

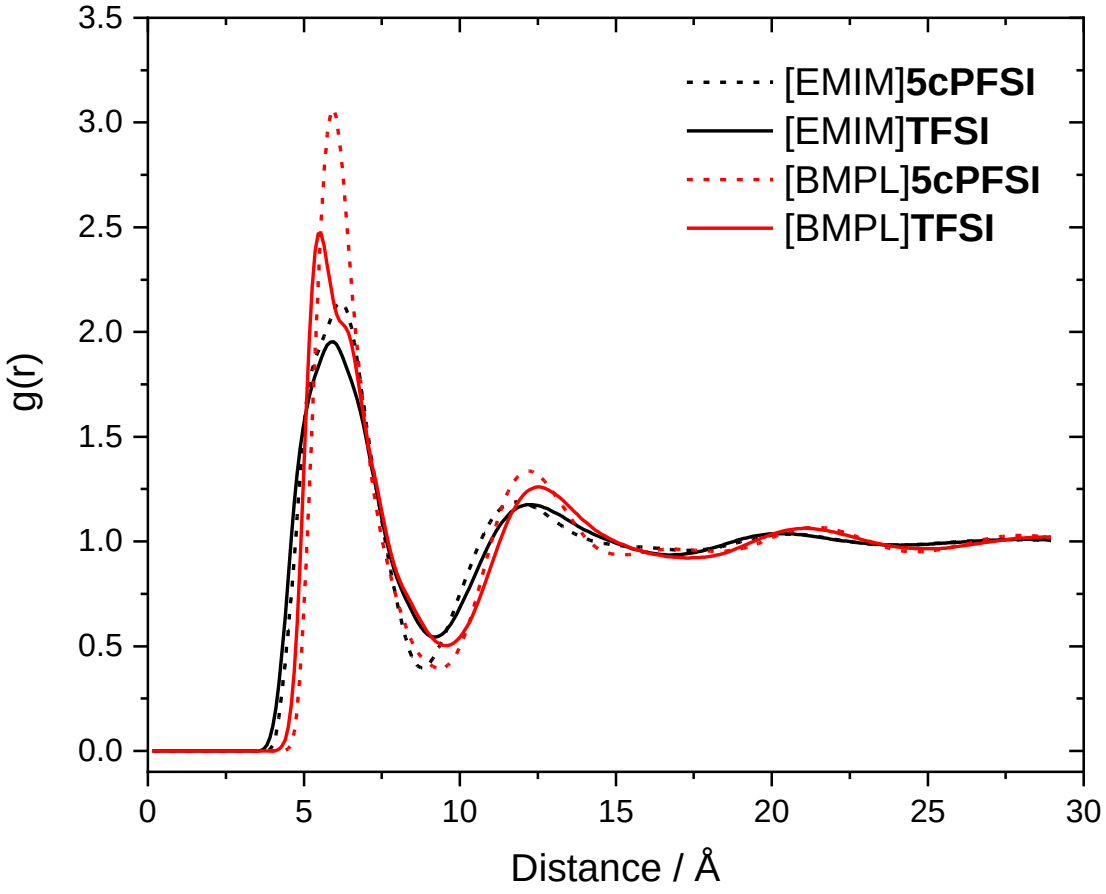

Figure S3: Cation-anion radial distribution functions.

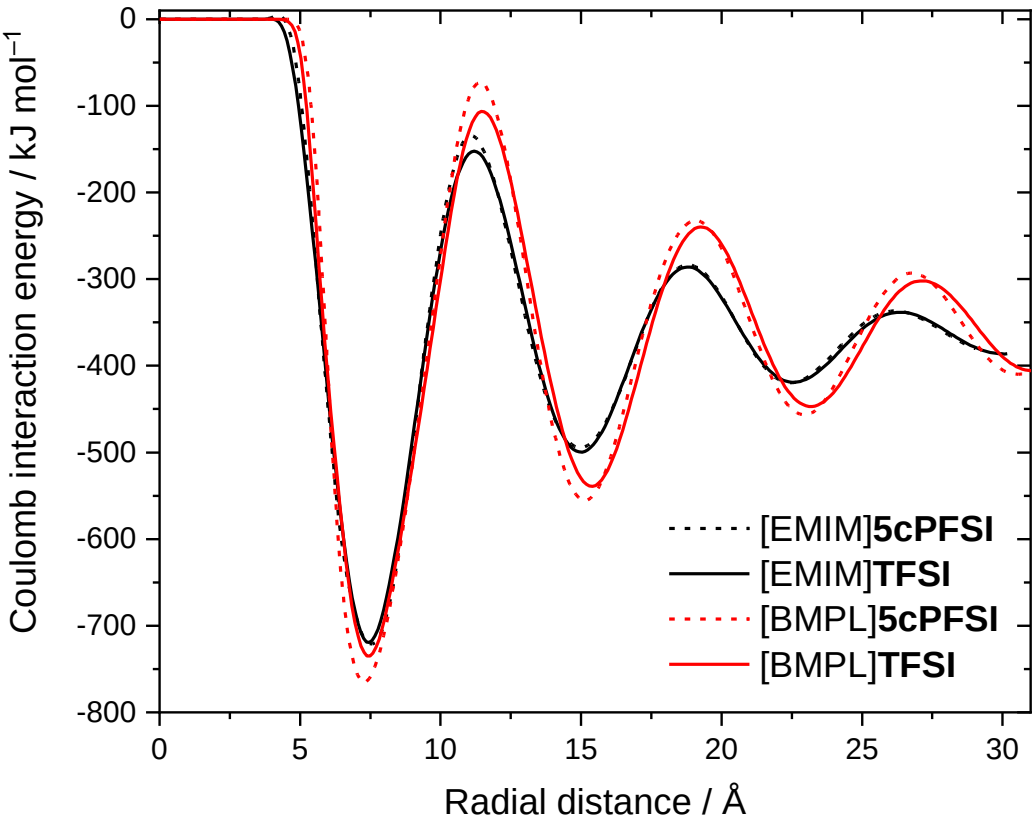

Figure S4: Coulomb interaction energy obtained from radial integration, using the centre of mass.

For the sake of completeness, the cation-cation radial distribution function was recalculated using the centre of ring (imidazolium or pyrrolidinium backbone atoms, equal weight to all atoms) rather than the centre of mass, **Figure S5**. Importantly, the close contacts remain for the imidazolium cations.

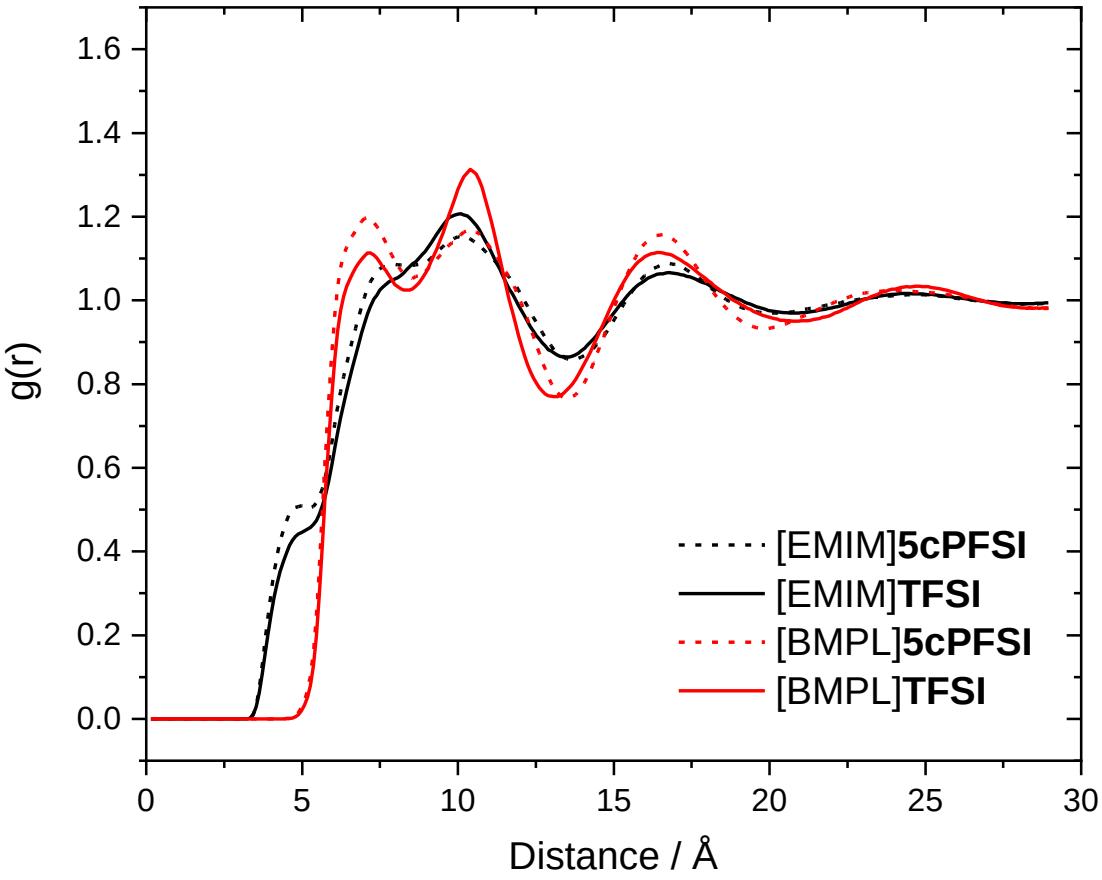

Figure S5: Cation-cation radial distribution functions, using the centre of ring.

Anion-Anion close contacts

The ionic liquids with the rigid, cyclic anions showed more pronounced anion-anion close contacts in their radial distribution functions, especially with the imidazolium cation (**Figure S2**). We thus performed a more detailed analysis of the statistical structure of the bulk ionic liquid [EMIM]**5cPFSI**.

The corresponding spatial distribution function, **Figure S6**, shows that given a central **5cPFSI** anion, other anions reside preferentially on the fluorinated side. Some anions are also found on the side of the nitrogen atom, however this is less pronounced (not visible with the threshold used in **Figure S6**).

Figure S7 shows the corresponding atom-resolved spatial distribution functions, which give more insight into mutual orientation. The anion-anion contacts are not isotropic; specifically the intermolecular contacts preferably involve fluorine-fluorine contacts.

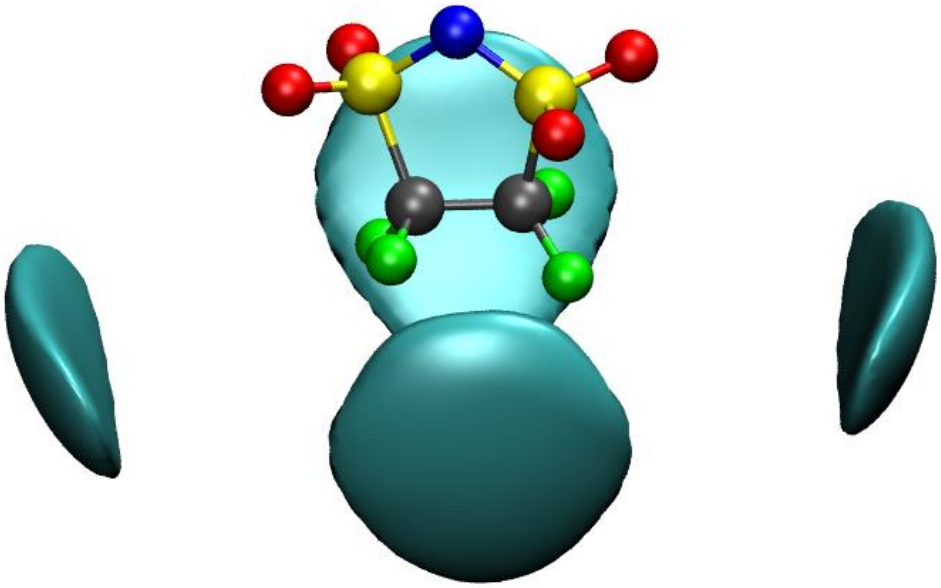

Figure S6: spatial distribution of **5cPFSI** around **5cPFSI** using the centre of mass, isosurface drawn at 60% of maximum value.

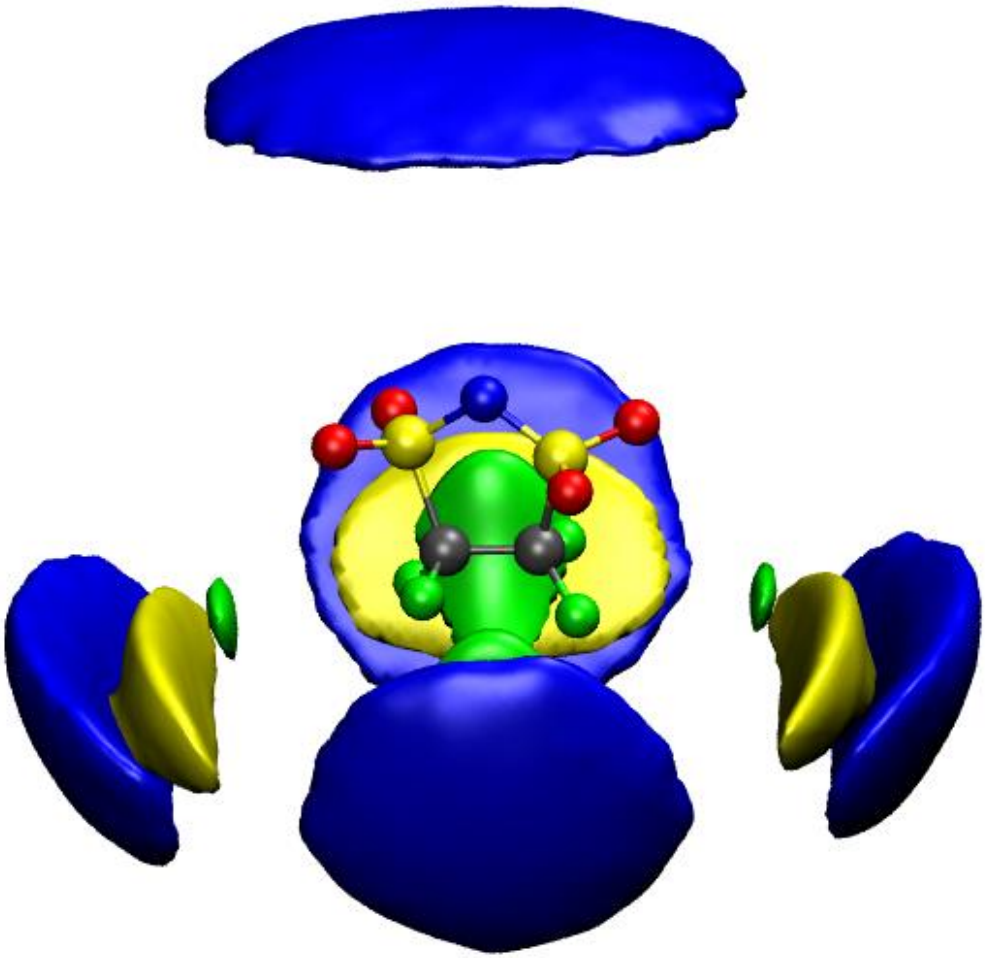

Figure S7: Atom resolved spatial distribution function for **5cPFSI** around **5cPFSI**. Isosurfaces for S, N, F atoms are drawn at 75% of the maximum value, C and O are not shown. Here, the CPK colour scheme is used for atoms and isosurfaces (green = F, black = C; yellow = S, red = O, blue = N).

To further substantiate the observation of an antiparallel orientation, we recorded histograms binned by two dimensions: a) the centre of mass distance between the anions; b) and the angle between the vectors defined in **Figure S8**. Indeed, the antiparallel orientation is observed unambiguously in the resulting histogram, **Figure S9**.

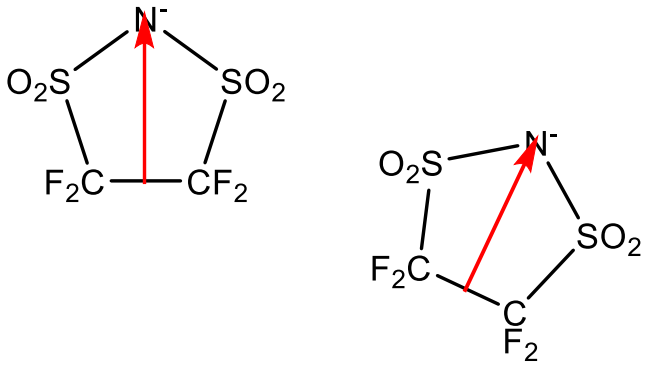

Figure S8: Definition of vectors for the relative orientation of anions. The base of the vector is defined as the centre of mass of the two carbon atoms, the nitrogen atom is the tip of the vector.

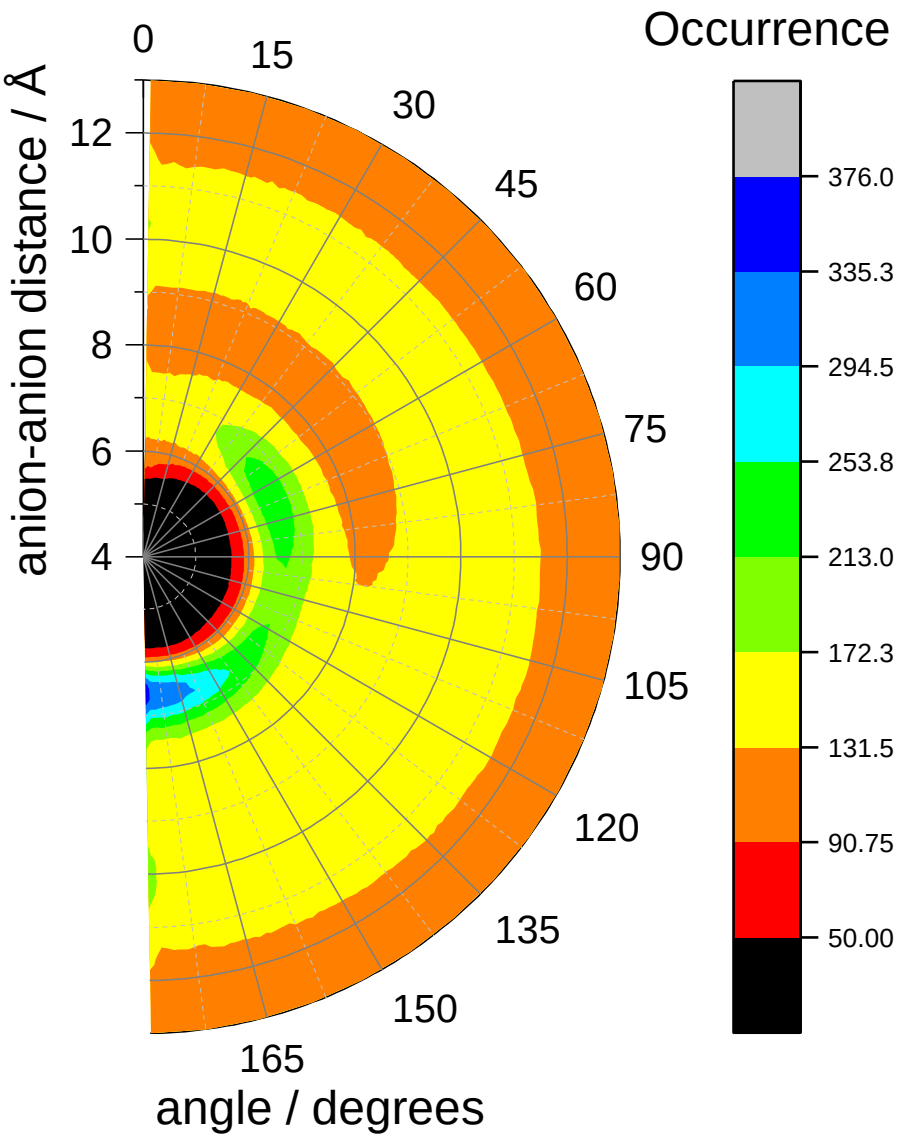

Figure S9: Histogram of anion-anion close contacts, demonstrating the anisotropy (blue region corresponds to antiparallel vectors)

While **Figure S9** shows the antiparallel orientation, it does not contain any spatial information (the coordinating anion might be found anywhere on a sphere with a certain distance to the reference anion, as long as the orientation is correct). Hence, we also obtained the histogram binned by two different dimensions, a) the angle between the two red vectors in **Figure S8** and b) the angle between the red vector in **Figure S8** (for the reference anion) and the vector connecting the centres of mass for reference and observed anion. This histogram, **Figure S11**, gives a more detailed insight into the intramolecular coordination environment. The four prevalent structures (*i.e.* maxima in the histogram) correspond to the mutual orientations shown schematically in **Figure S10**. Only pairs within 8.2 Å were considered based on the minimum in the anion-anion RDF; for the sake of completeness the histogram was constructed again, considering only the one nearest anion neighbour as opposed to every anion within the distance threshold, **Figure S12**. The distribution did not change qualitatively.

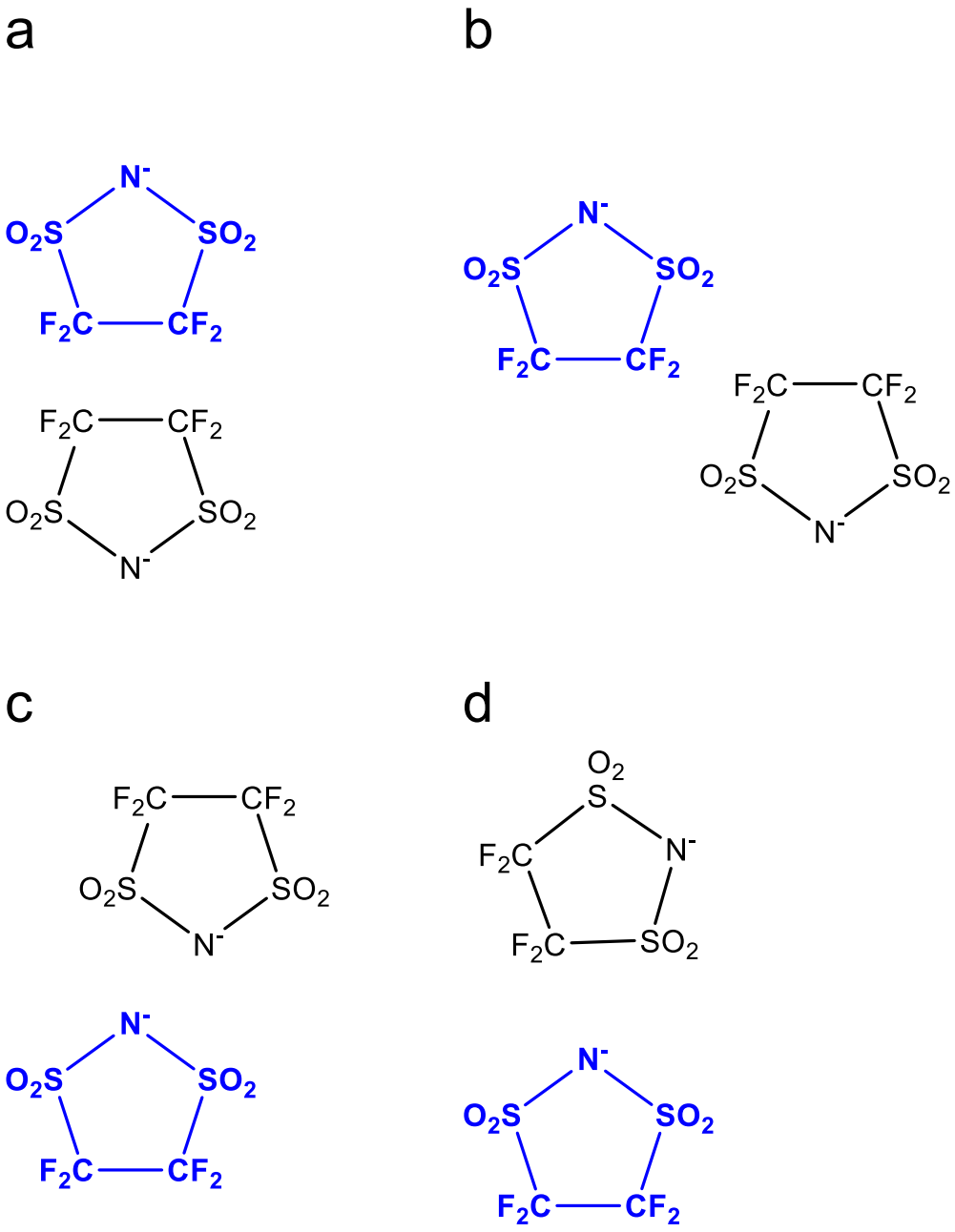

Figure S10: Schematic representation of the structures from **Figure S11**.

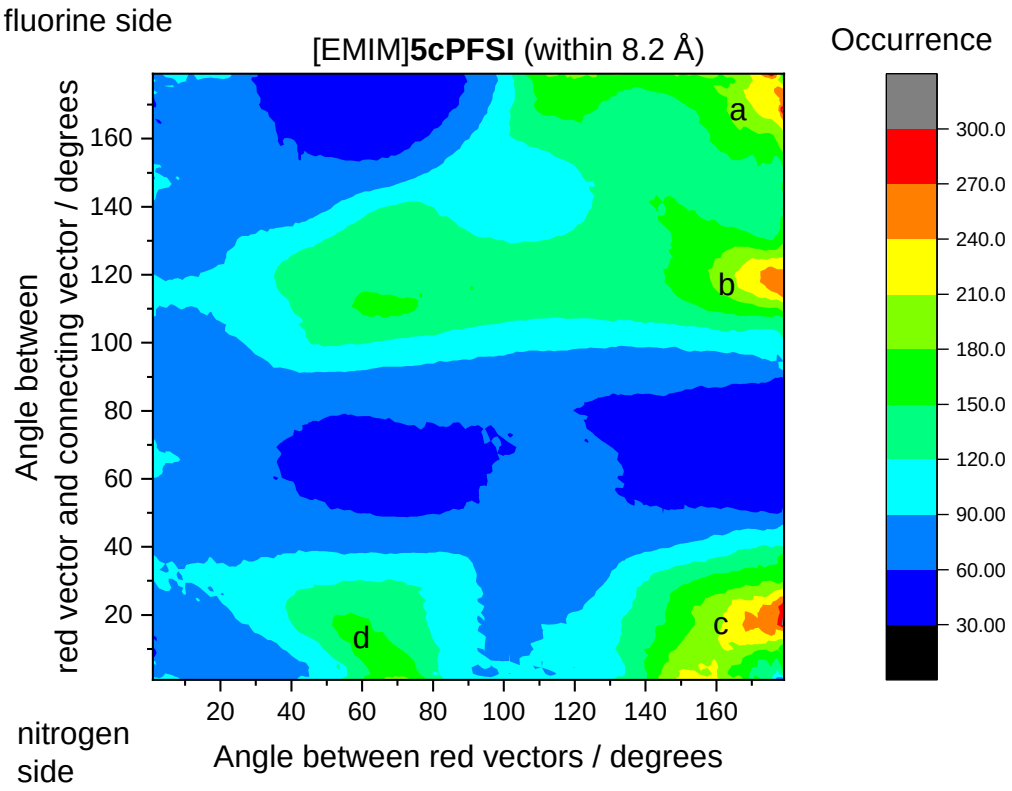

Figure S11: Histogram of occurrences of relative anion-anion orientations. The x axis shows the angle between the two red vectors in **Figure S8**. The y axis shows the angle between the red vector in **Figure S8** for the reference anion, and the vector connecting the centres of mass for reference and observed anion.

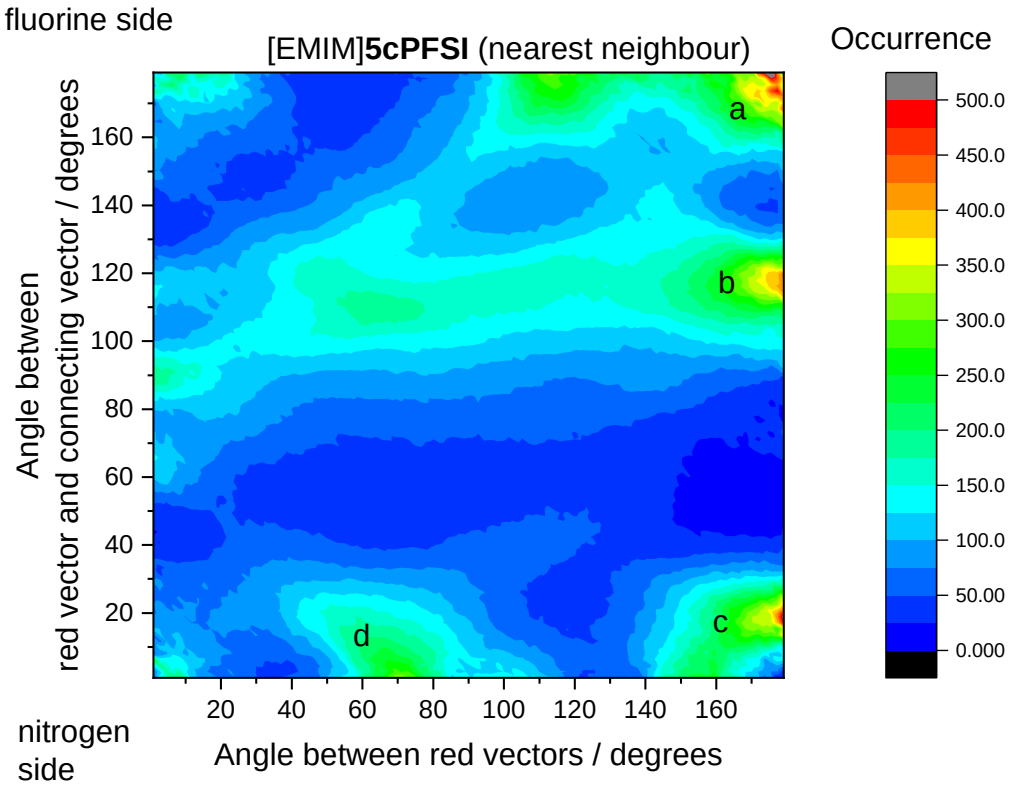

Figure S12: Same as **Figure S11**, but using only the nearest anion neighbour instead of every neighbour within 8.2 Å.

Structuring in [BMPL]**5cPFSI**

As can be seen from the radial distribution functions, the ionic liquid [BMPL]**5cPFSI** has a very well-defined structure. High values of the radial distribution function correspond to energetically deeper wells in the potential energy surface. Correspondingly, barriers are higher for the transition between these wells, which in turn impedes structural relaxation. This has an impact on transport properties such as diffusion (translational motion) or viscosity (momentum transport). The spatial distribution function for the distribution of **5cPFSI** around a central $[BMPL]^+$ reference cation shows this as well, **Figure S13**. For comparison, the spatial distribution function for the much more flexible **TFSI** anion (same print levels, same orientation), **Figure S14**, shows less well-defined minima.

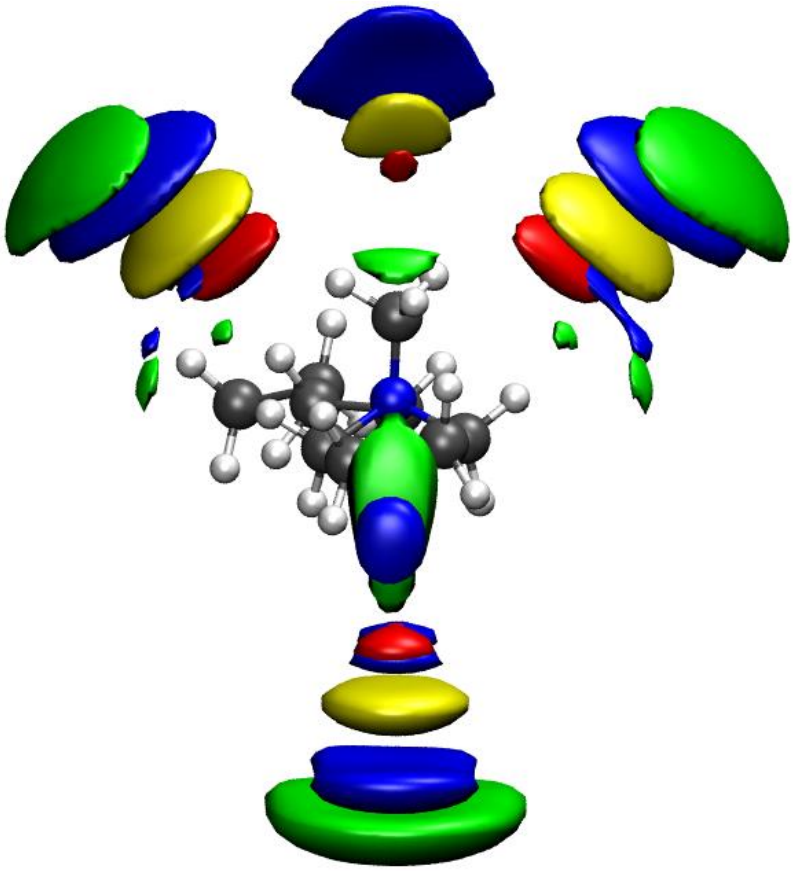

Figure S13: Atom resolved spatial distribution function for **5cPFSI** around $[BMPL]^+$. View: Methyl group points up, butyl chain points back out of the paper plane. O,S,N are shown at 60% of the maximum value, F at 75%, carbons are not shown.

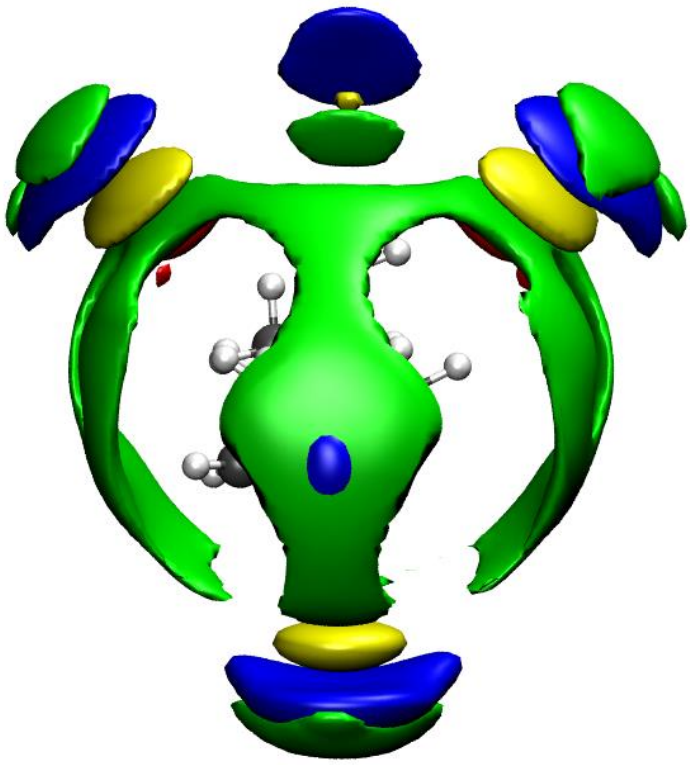

Figure S14: Same as **Figure S13**, but for **TFSI** around $[BMPL]^+$.

The comparison across **Figure S13** and **Figure S14** is not ideal since **TFSI** has more fluorine atoms than **5cPFSI**, which is not accounted for here. Thus, **Figure S15** shows the centre of mass distributions of anions around a central $[BMPL]^+$ reference cation. The spatial distribution functions are overlayed, and the difference is clearly visible. Similar observations can be made comparing the [EMIM]**5cPFSI** and [EMIM]**TFSI** ionic liquids, **Figure S16**. The qualitative differences in the spatial distribution functions are smaller for $[EMIM]^+$, but the absolute maximum values are bigger for the **5cPFSI** anion in both cases, indicating a well-defined structure in line with the radial distribution functions.

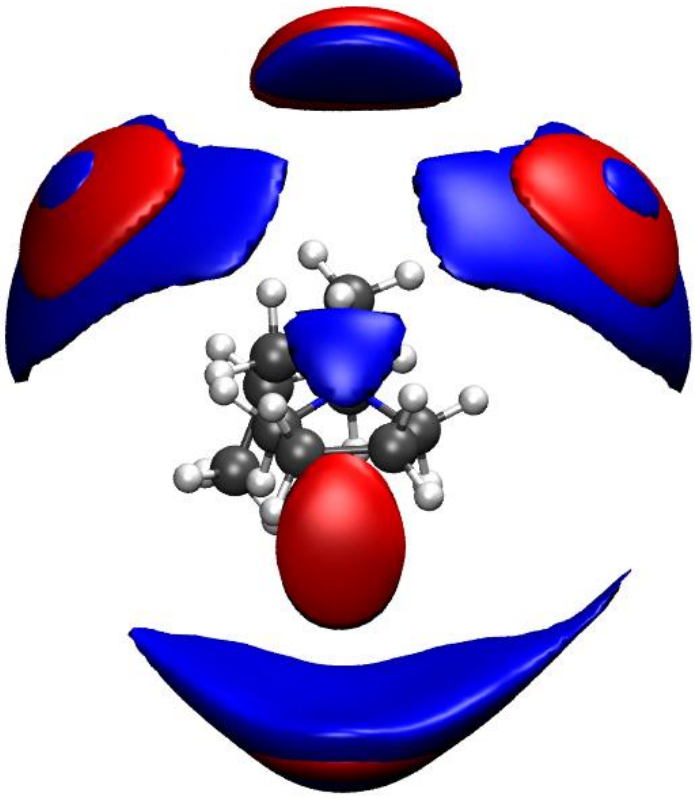

Figure S15: Centre of mass distribution of **TFSI** anions (blue) and **5cPFSI** anions (red) in their respective ionic liquids with the $[BMPL]^+$ cation. Both isosurfaces are drawn at 50% of the maximum value.

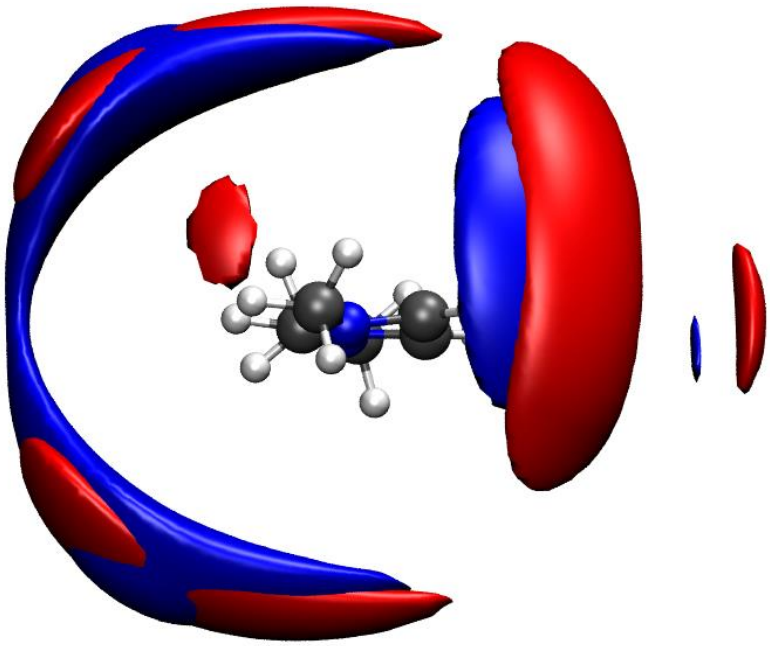

Figure S16: Same as **Figure S15**, but with the $[EMIM]^+$ cation. **TFSI** is blue, **5cPFSI** is red, both are drawn at 50% of the maximum value. The orientation of the cation is as follows: view on the methyl group, the ethyl chain goes back out of the paper plane, the C2 carbon is on the left.

The quantitative differences in the spatial distribution functions for **TFSI** and **5cPFSI** in **Figure S15** are visible in the potential of mean force for the movement of the anions around the cation, **Figure S17**. The points in space corresponding to the reaction coordinate in **Figure S17** are shown in **Figure S18**. The lowest energy path in the potential of mean force in three dimensions has been calculated using a nudged elastic band optimiser as described in reference[23].

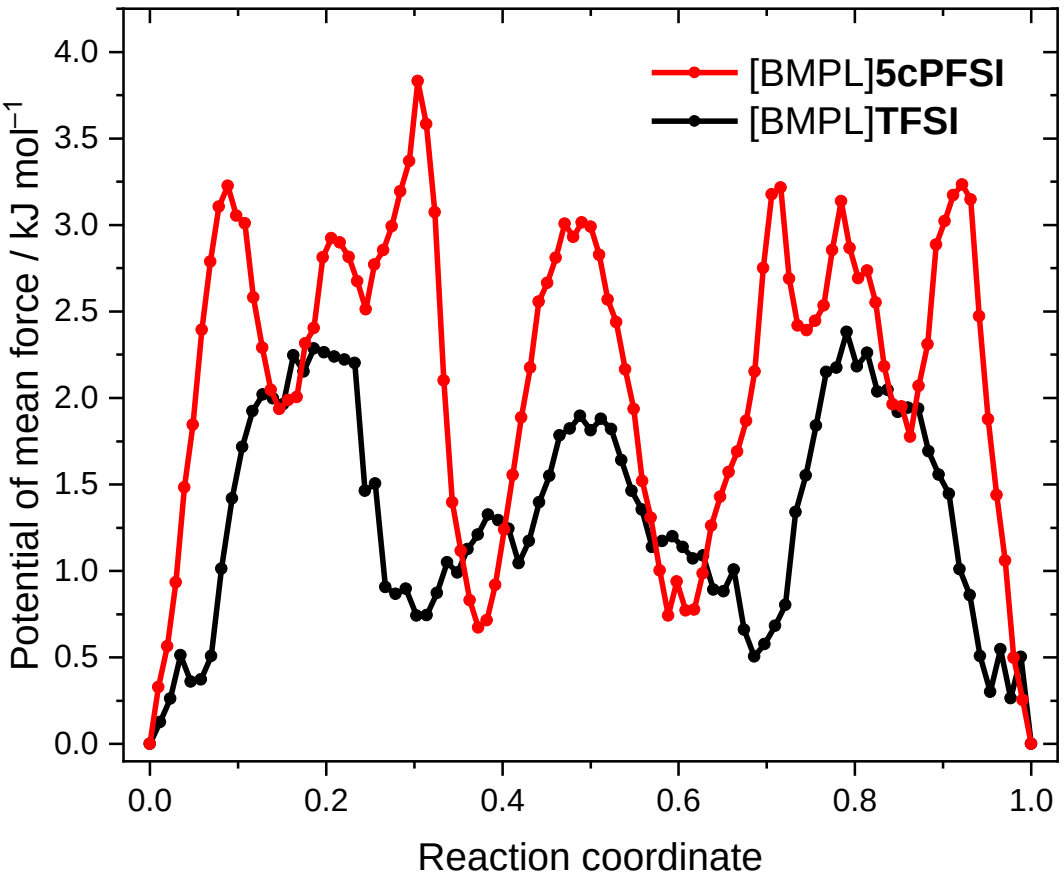

Figure S17: Potential of mean force for movement of the anions (centre of mass) around the $[BMPL]^+$ cation.

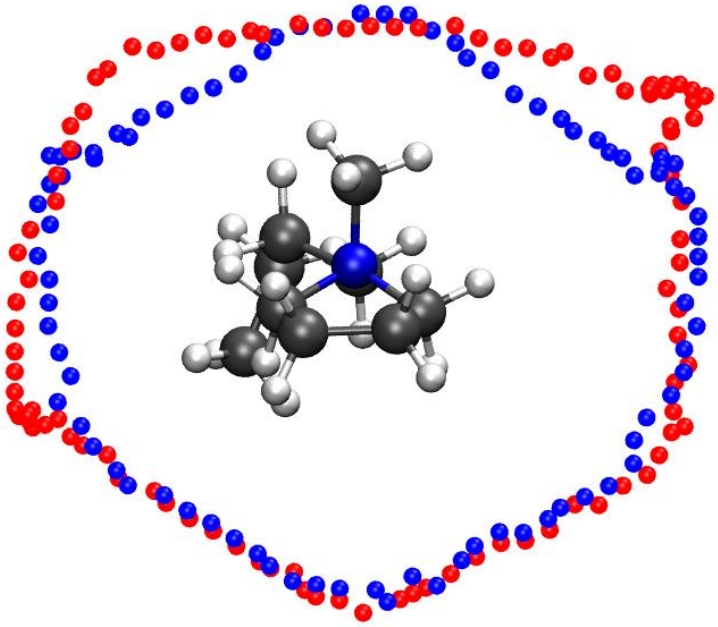

Figure S18: The points used for the PMF path in **Figure S17**.

Charge Arm Distribution

Briefly, the charge arm is a simple measure for charge asymmetry / anisotropic electrostatic interactions in ionic systems and is mathematically equivalent to a dipole moment calculated in the centre of mass reference frame. Here we only demonstrate that the charge arm distribution is not significantly impacted by the counter ion, see **Figure S19** for cations and **Figure S20** for anions. For details, see[22].

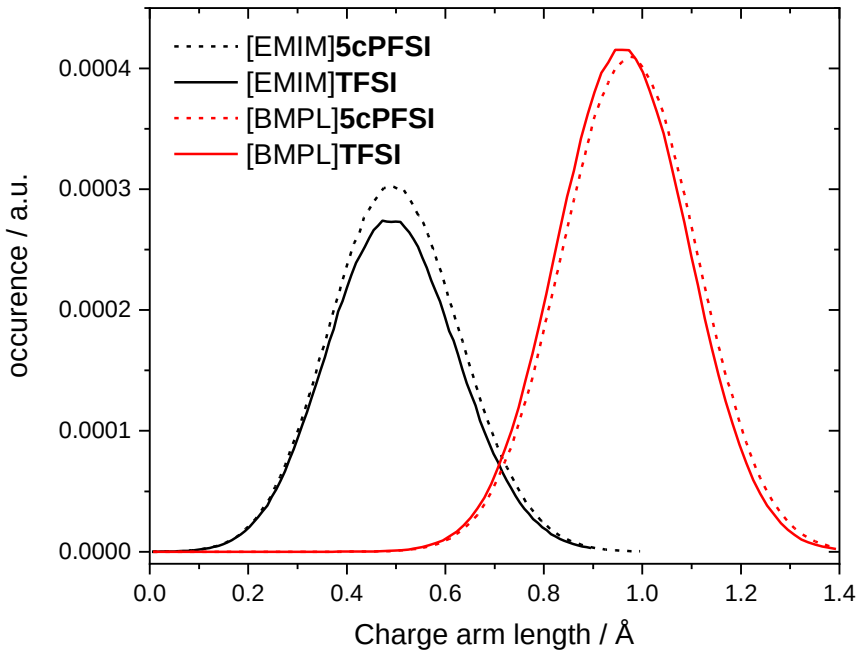

Figure S19: Charge arm distribution of the cations.

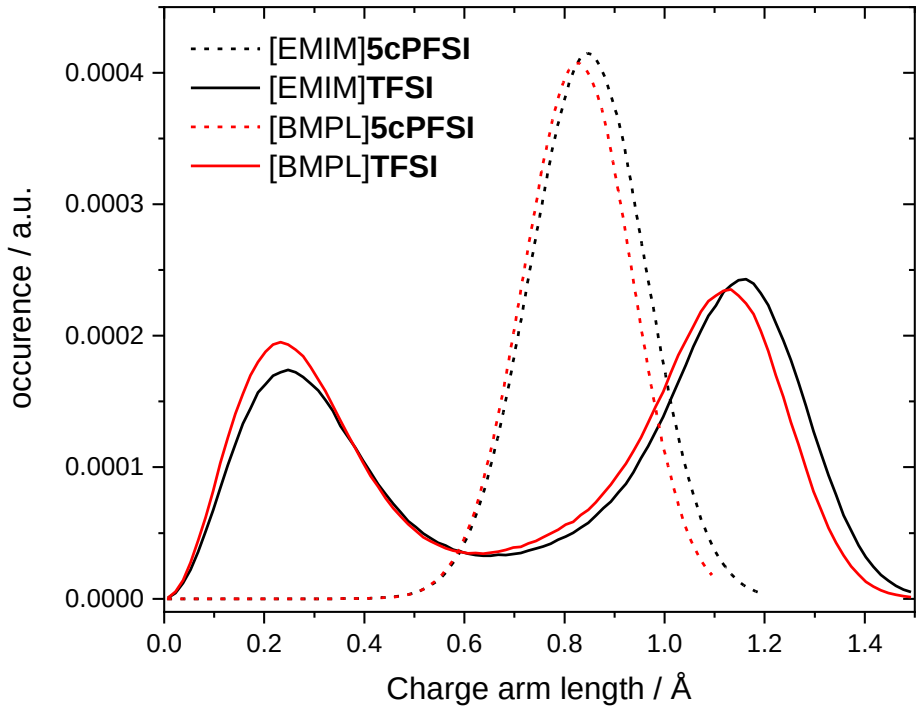

Figure S20: Charge arm distribution of the anions. For **TFSI**, there are two peaks due to cis and trans conformers.

Cation Cation interactions / π stacking

Pronounced π-stacking was observed in some of the crystal structures. This is also the case in the MD simulation of the liquids, see **Figure S21** for an exemplary snapshot. Here we demonstrate using combined distribution functions that π-stacking is present in both simulations of imidazolium ionic liquids, [EMIM]**TFSI** and [EMIM]**5cPFSI**, **Figure S22** and **Figure S23**, respectively. In these distribution functions, the first channel is the distance between the centres of ring (x-axis, centre of ring defined by backbone atoms with equal weight). The second channel is the angle between the vectors normal to the plane (y-axis, defined *via* the three carbon atoms in the imidazolium ring). In both ionic liquids, pronounced features for close contacts (near 4 Å) are visible for parallel and antiparallel angles between the normal plane, as expected for π-stacking. Naturally, the normal vector does not give information about the mutual rotation of the two ring systems. To this end, we also calculated the corresponding combined distribution functions using the vectors connecting the nitrogen atoms, **Figure S24** and **Figure S25**. The antiparallel geometry – as was observed in the crystal structure of [EMIM]**5cPFSI** – is also found in the bulk liquid simulations. Interestingly, parallel arrangements were equally likely, but not arrangements with intermediate angles.

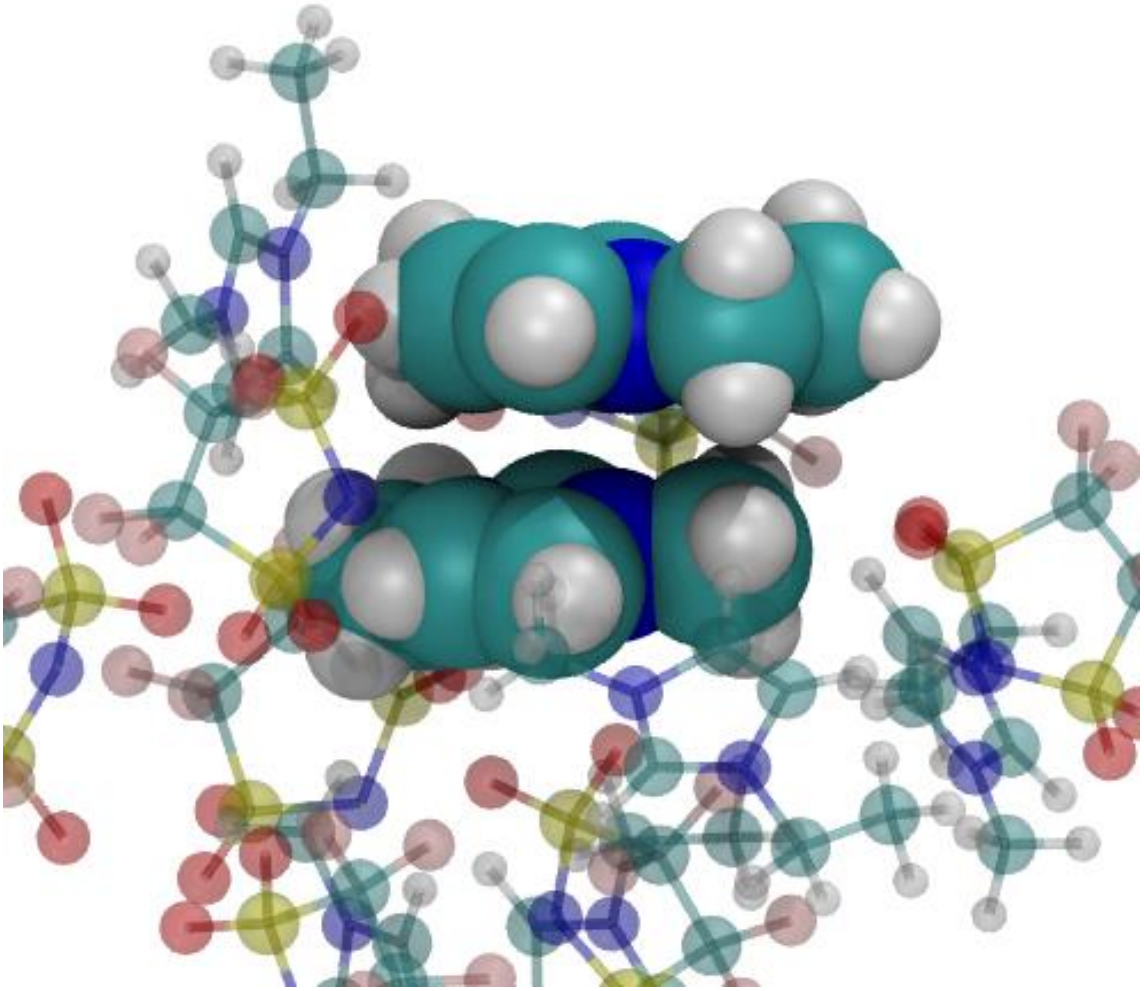

Figure S21: Example of π-stacking between imidazolium cations in close contact.

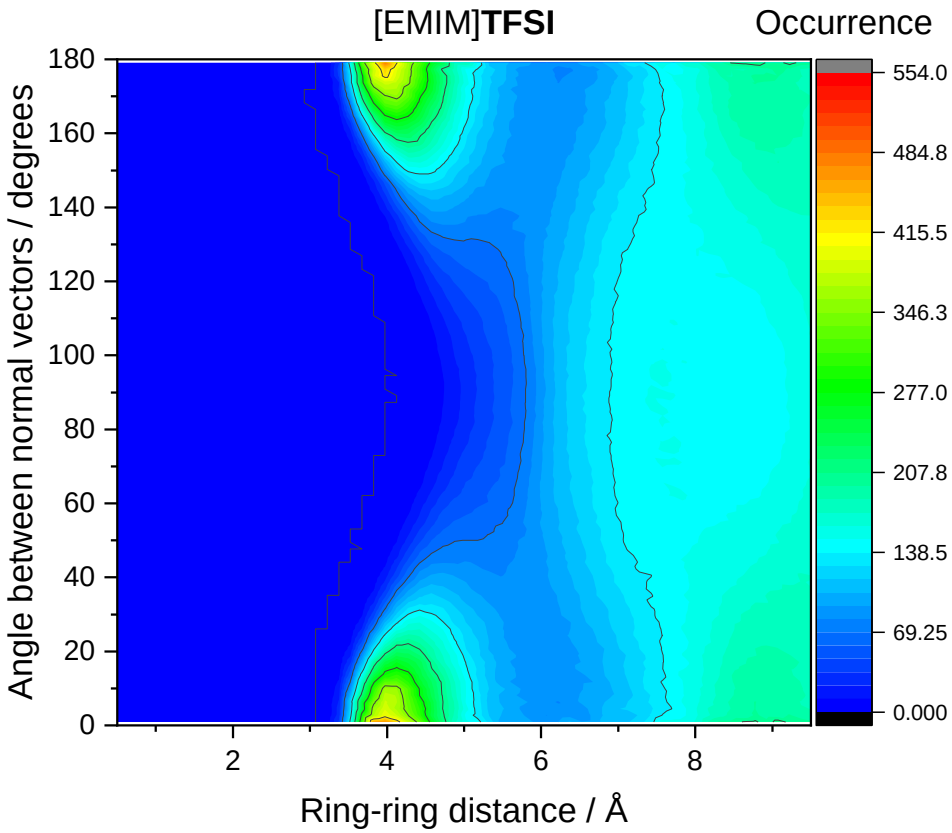

Figure S22: Combined distribution function showing the π stacking of cations in [EMIM]**TFSI**.

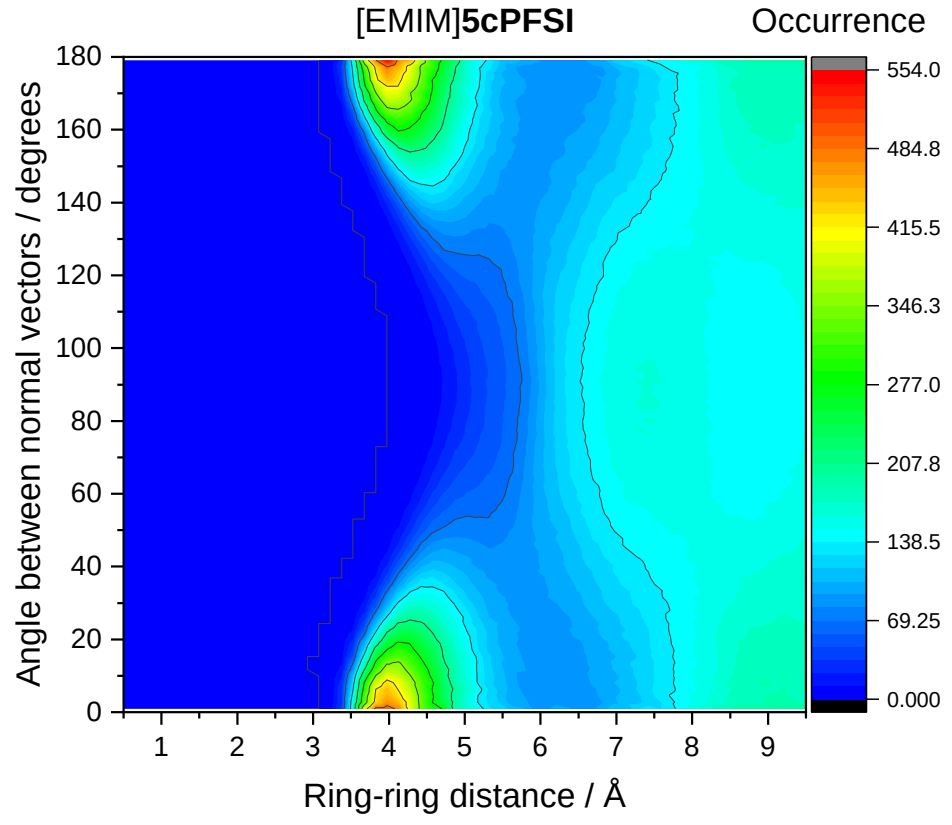

Figure S23: Combined distribution function showing the π stacking of cations in [EMIM]**5cPFSI**.

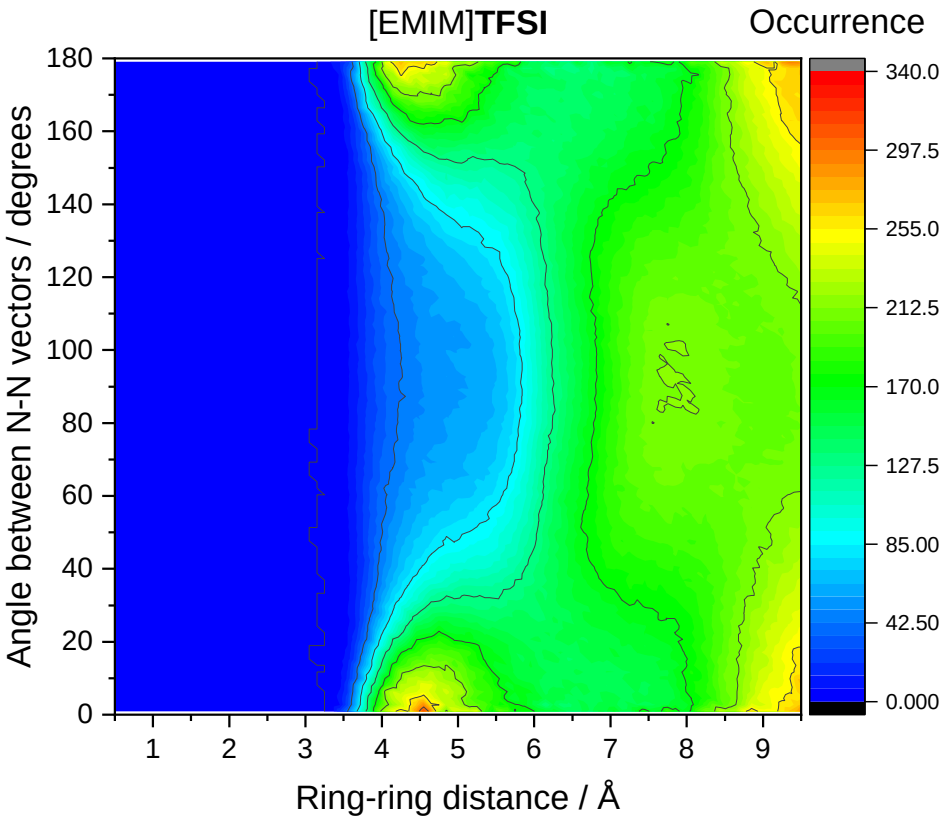

Figure S24: Analogous to **Figure S22**, using the N-N vector instead of the normal vector for the second channel (y axis).

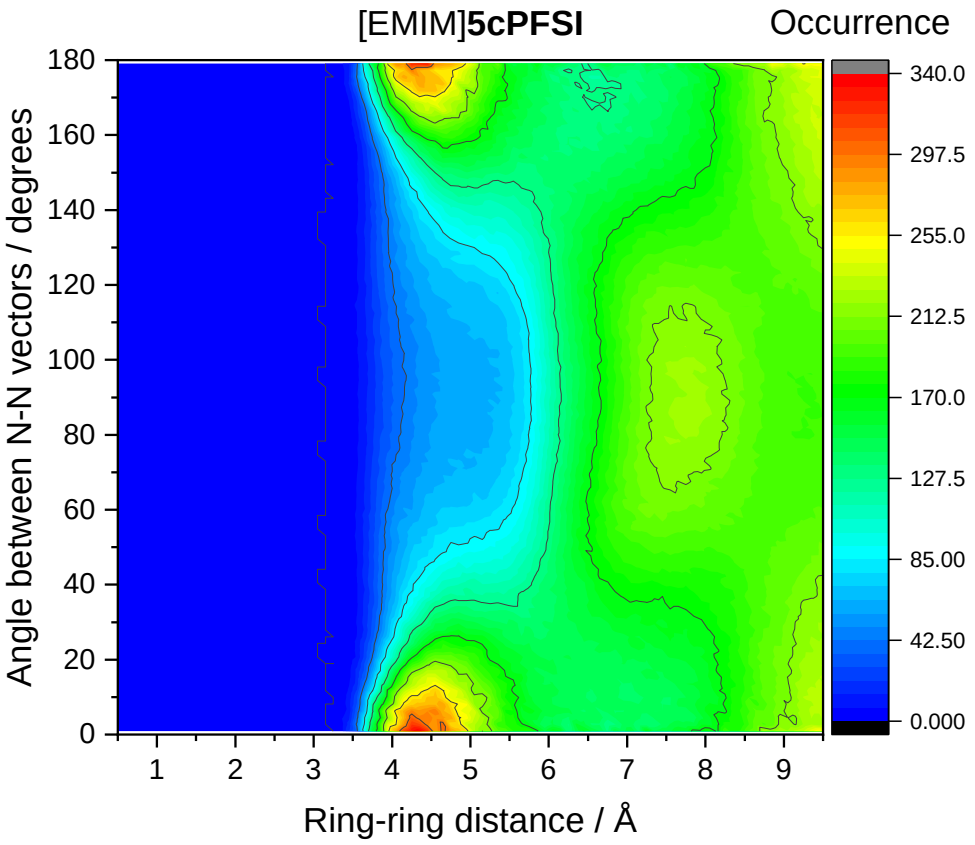

Figure S25: Analogous to **Figure S23**, using the N-N vector instead of the normal vector for the second channel (y axis).

Liquid Dynamics

Dynamical Heterogeneity

The liquid dynamics will be discussed only briefly here, since we already discussed several experimental transport properties in the main manuscript. However, the simulations also give access to the non-gaussian parameter shown in **Figure S26** for the cation diffusion and in **Figure S27** for the anion diffusion. It is clear that the degree of dynamical heterogeneity is highest for [BMPL]**5cPFSI**, in line with the pronounced structuring in this ionic liquid.

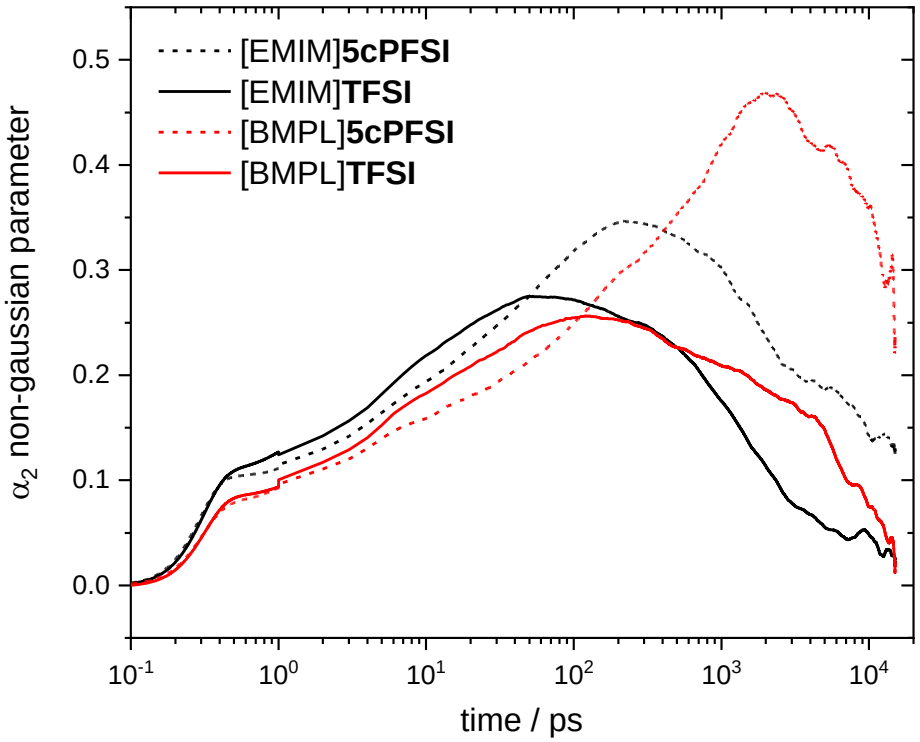

Figure S26: Non-gaussian (α_2) parameter for the cations.

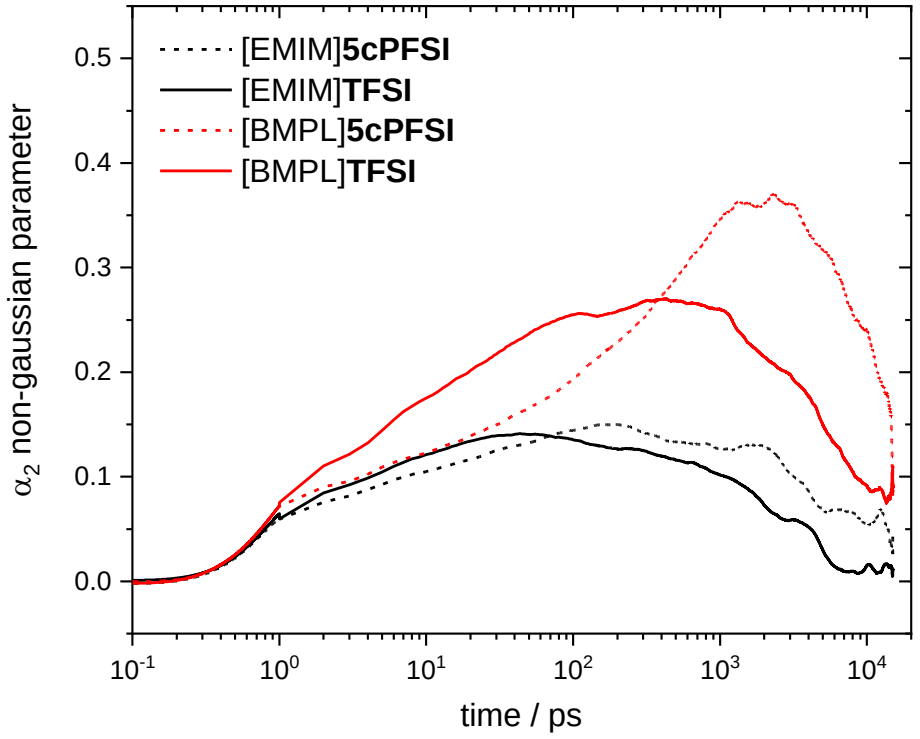

Figure S27: Non-gaussian (α_2) parameter for the anions.

IR and Raman Spectra

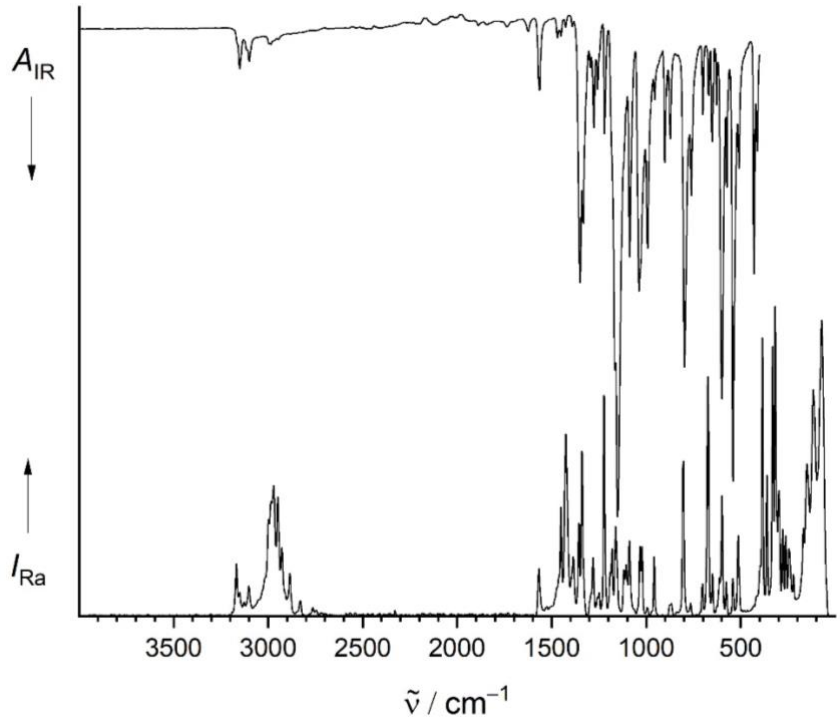

Figure S28: IR (top) and Raman (bottom) spectra of solid [EMIm]**6cPFSI**.

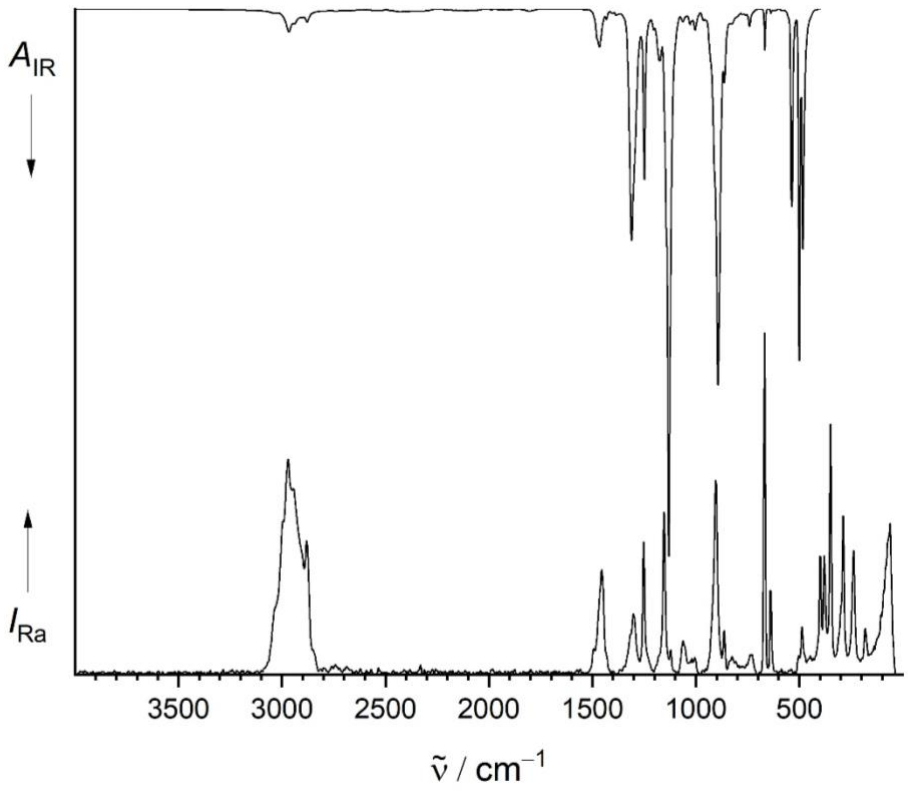

Figure S29: IR (top) and Raman (bottom) spectra of solid [BMPL]**4cPFSI**.

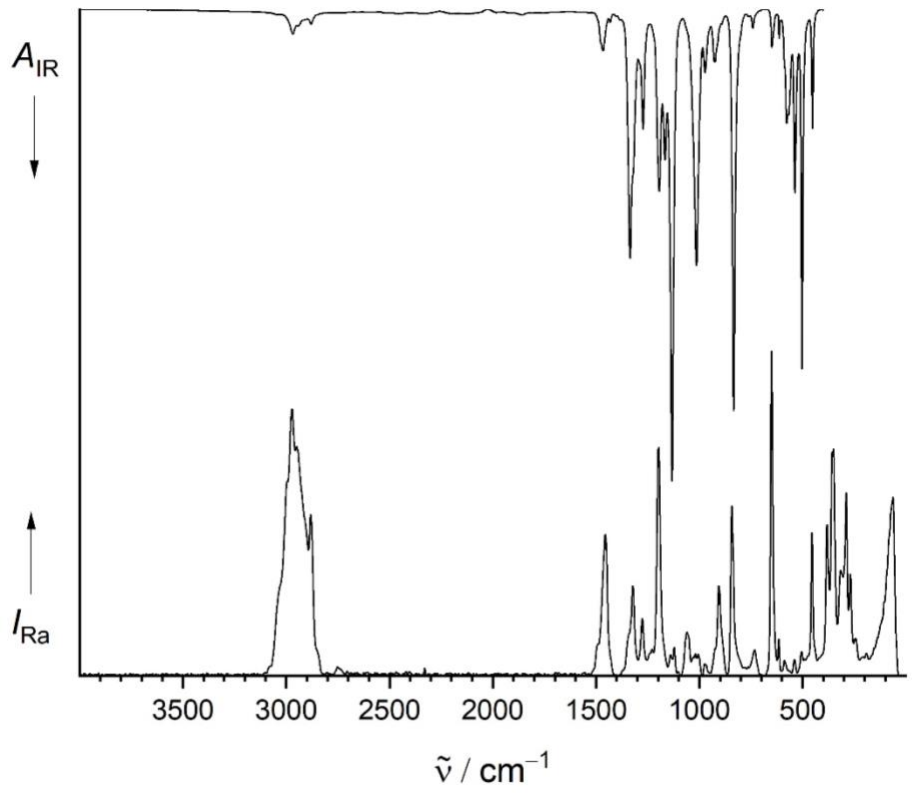

Figure S30: IR (top) and Raman (bottom) spectra of liquid [BMPL]**5cPFSI**.

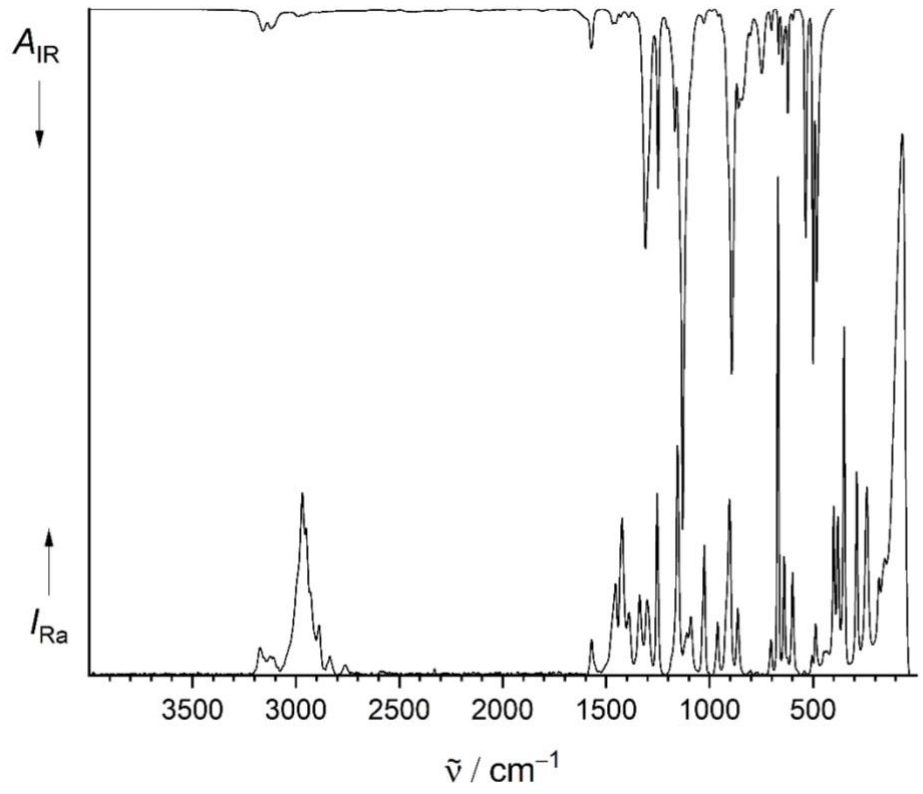

Figure S31: IR (top) and Raman (bottom) spectra of liquid [EMIm]**4cPFSI**.

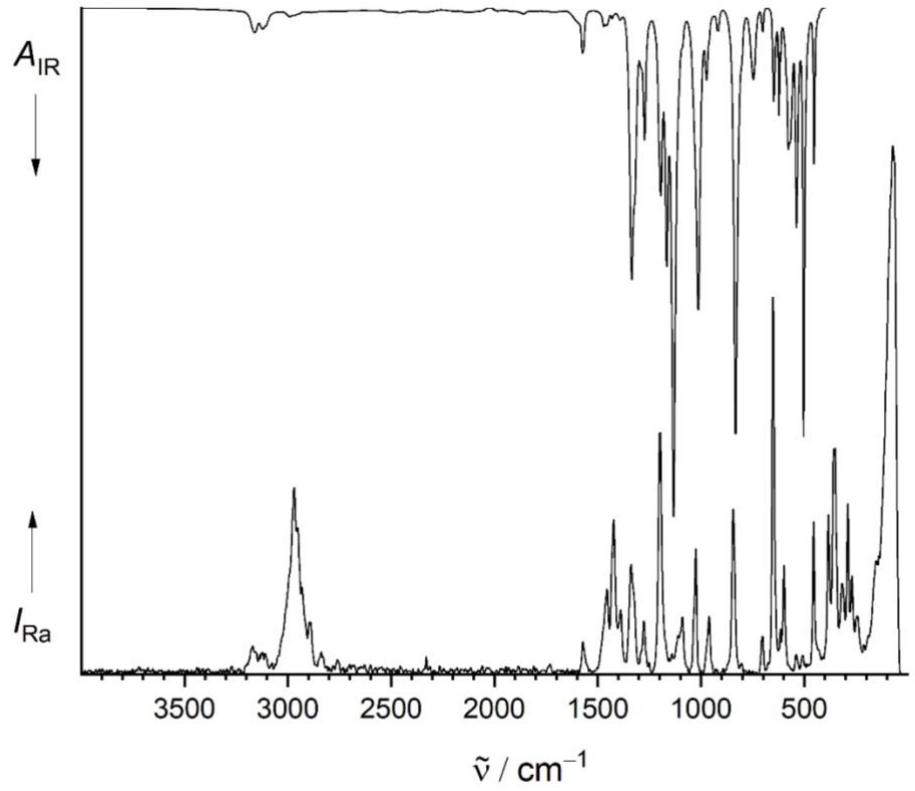

Figure S32: IR (top) and Raman (bottom) spectra of liquid [EMIm]**5cPFSI**.

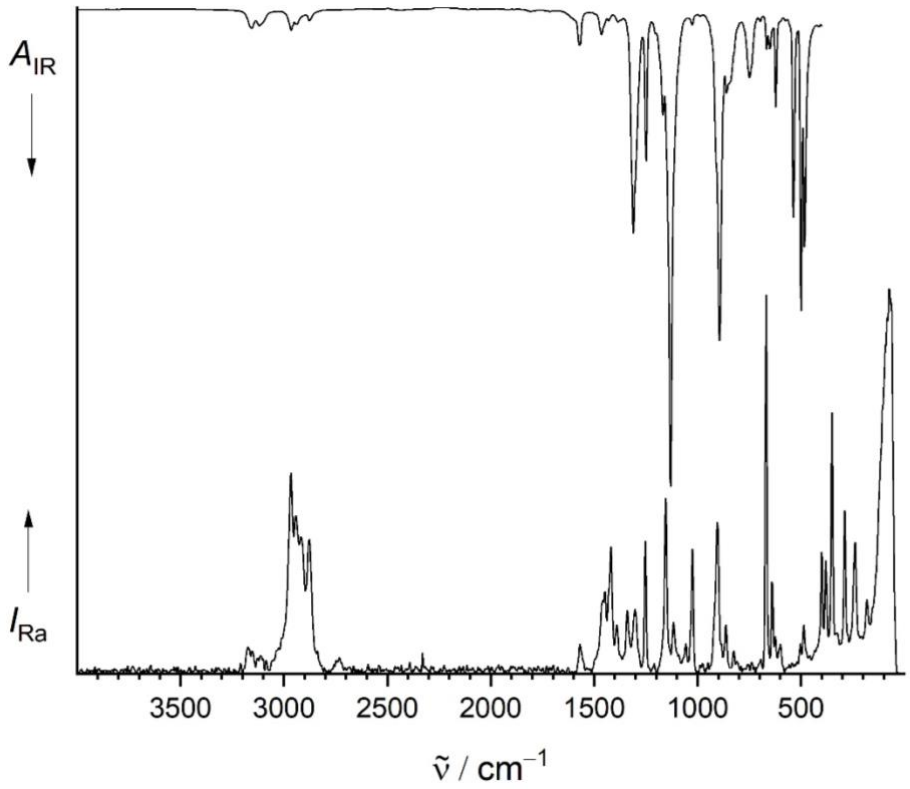

Figure S33: IR (top) and Raman (bottom) spectra of solid [BMIm]**4cPFSI**.

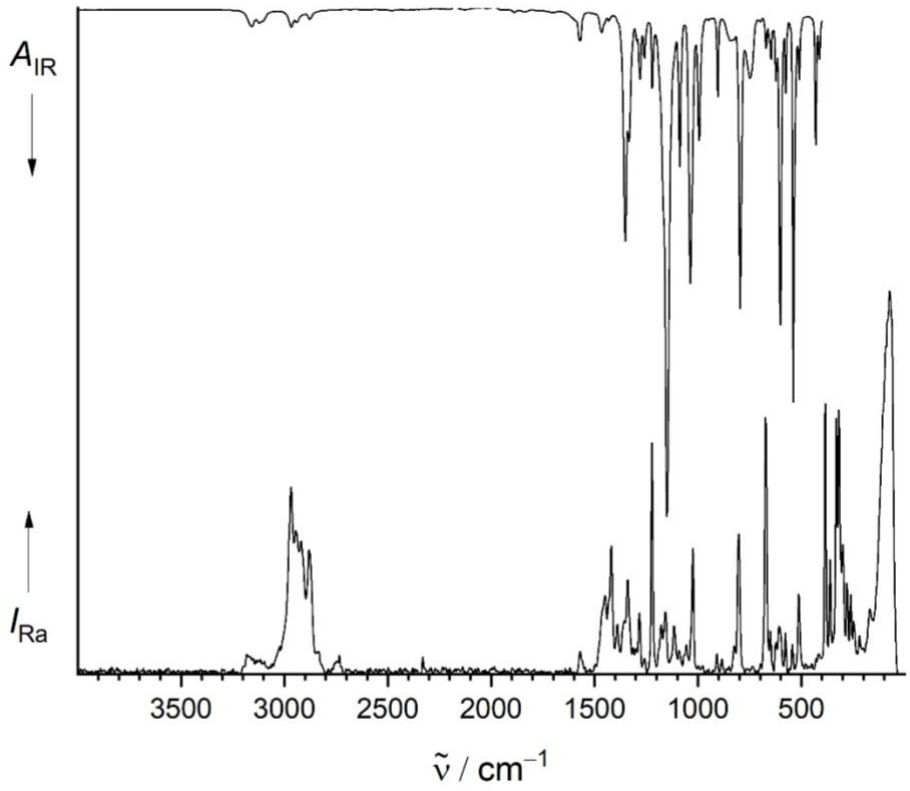

Figure S34: IR (top) and Raman (bottom) spectra of solid [BMIm]**6cPFSI**.

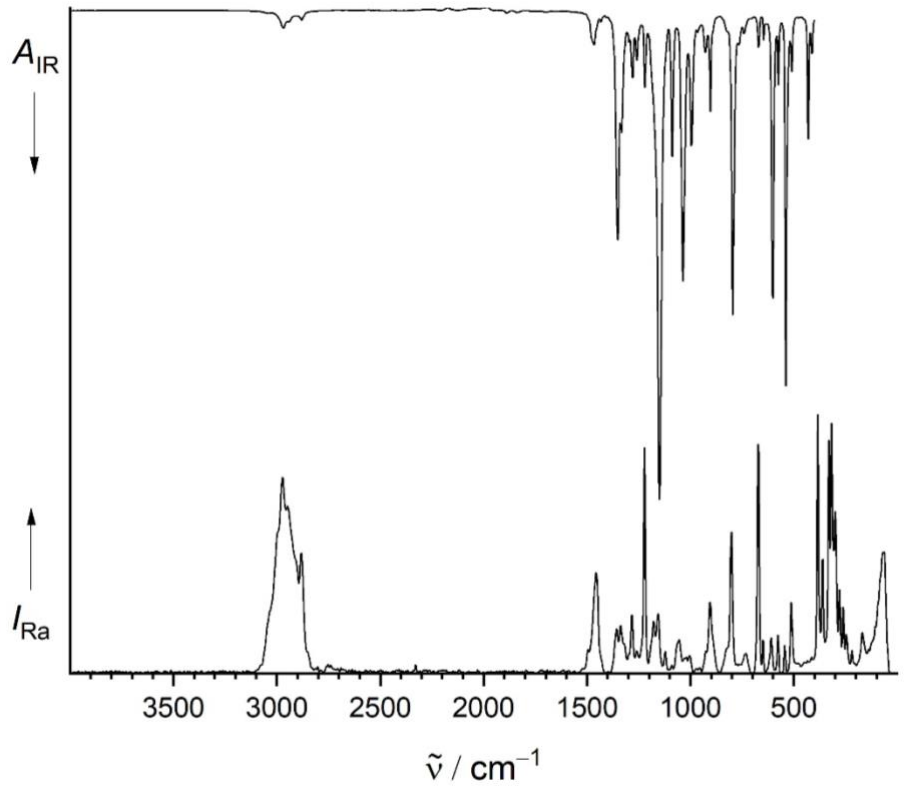

Figure S35: IR (top) and Raman (bottom) spectra of solid [BMPL]**6cPFSI**.

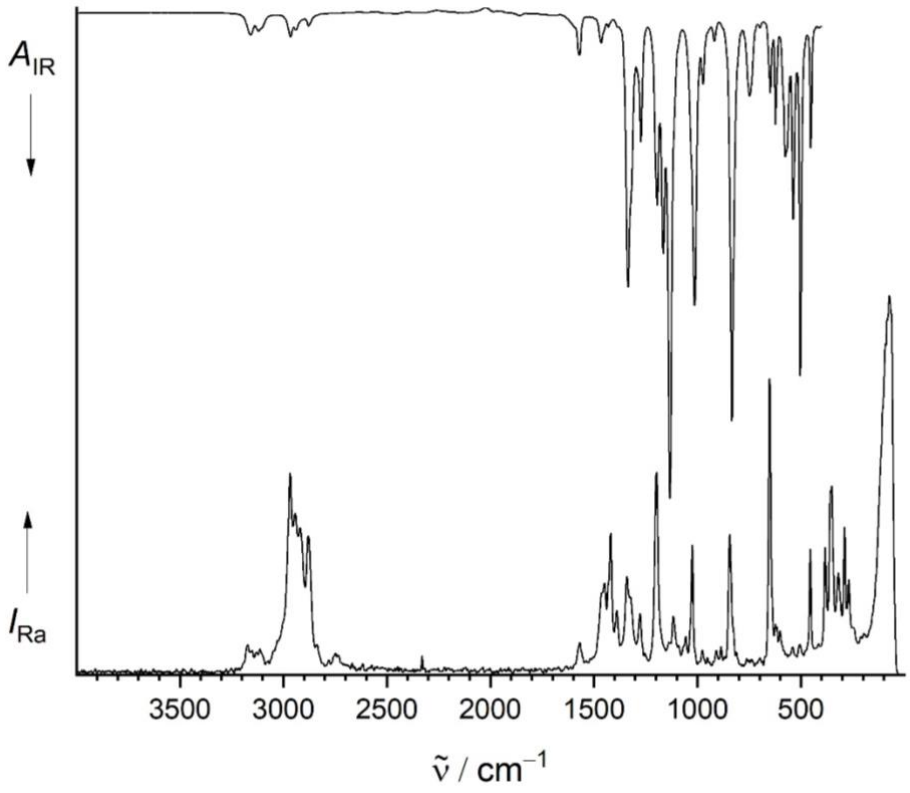

Figure S36: IR (top) and Raman (bottom) spectra of liquid [BMIm]**5cPFSI**.

Viscosity, Conductivity, Density and Diffusion

Table S1: Temperature dependent dynamic viscosities (η) in mPa·s.

T / °C	[EMIm]**4cPFSI**	[EMIm]**5cPFSI**	[EMIm]**TFSI**	[BMIm]**4cPFSI**	[BMIm]**5cPFSI**	[BMIm]**6cPFSI**	[BMIm]**TFSI**	[BMPL]**4cPFSI**	[BMPL]**5cPFSI**	[BMPL]**6cPFSI**	[BMPL]**TFSI**
20	50.4	53.0	37.8	93.8	85.0	250.3	62.0	129.6	143.5	469.2	98.8
23	45.2	48.2	34.4	82.3	75.7	209.8	55.6	111.8	123.0	387.5	87.2
25	41.8	44.8	32.0	74.3	69.5	186.3	50.7	101.8	112.8	343.6	79.5
30	34.5	37.7	26.8	59.1	56.5	140.7	41.0	82.8	91.2	251.7	63.1
40	24.3	27.9	19.6	38.9	38.7	85.8	28.1	55.9	63.7	143.4	42.4
50	18.1	21.1	15.2	27.3	27.9	55.9	20.3	39.4	43.4	90.0	30.0
60	14.0	16.4	11.9	20.1	20.8	38.7	15.2	29.2	32.2	60.0	16.3
70	11.1	13.1	9.6	15.4	16.7	28.1	11.9	22.3	24.5	42.0	12.6
80	9.0	10.7	7.9	12.2	13.3	21.2	9.4	17.6	19.2	30.6	10.0

Table S2: Temperature dependent specific conductivities (σ) in $mS \cdot cm^{-1}$ determined by impedance spectroscopy.

T / °C	[EMIm]**4cPFSI**	[EMIm]**5cPFSI**	[EMIm]**TFSI**	[BMIm]**4cPFSI**	[BMIm]**5cPFSI**	[BMIm]**TFSI**	[BMPL]**5cPFSI**	[BMPL]**6cPFSI**	[BMPL]**TFSI**
20	4.37	2.84	7.22	1.99	1.84	3.11	1.13	0.34	1.36
25	5.23	3.29	8.38	2.44	2.20	3.74	1.36	0.45	1.65
30	6.08	3.78	9.64	3.00	2.58	4.44	1.64	0.57	1.99
35	7.20	4.29	10.97	3,59	3.02	5.16	1.96	0.72	2.35
40	8.29	4.86	12.42	4.17	3.57	6.01	2.31	0.89	2.78
45	9.46	5.59	13.91	4.83	4.01	6.91	2.69	1.07	3.24
50	10.69	6.07	15.49	5.57	4.66	7.88	3.11	1.29	3.72
55	12.01	6.75	17.15	6.38	5.06	8.91	3.61	1.53	4.18
60	13.40	7.71	18.86	7.19	5.70	9.86	4.09	1.79	4.81
65	14.86	8.21	20.61	8.33	6.48	10.97	4.64	2.08	5.29
70	16.39	9.01	22.51	9.04	6.93	12.13	5.24	2.38	5.91
75	18.02	9.75	23.44	10.04	7.89	13.05	5.90	2.72	6.56
80	19.69	10.57	25.24	11.17	8.39	14.24	6.70	3.08	7.23

Table S3: Temperature dependent densities (ρ) in $g \cdot cm^{-3}$.

T / °C	[EMIm]**4cPFSI**	[EMIm]**5cPFSI**	[EMIm]**TFSI**	[BMIm]**4cPFSI**	[BMIm]**5cPFSI**	[BMIm]**6cPFSI**	[BMIm]**TFSI**	[BMPL]**5cPFSI**	[BMPL]**6cPFSI**	[BMPL]**TFSI**
20	1.4696	1.5268	1.5243	1.3823	1.4369	1.4942	1.4425	1.3911	1.4487	1.3993
23	1.4666	1.5239	1.5213	1.3796	1.4342	1.4913	1.4396	1.3886	1.446	1.3966
25	1.4646	1.522	1.5192	1.3777	1.4323	1.4894	1.4377	1.387	1.4443	1.3949
30	1.4598	1.5172	1.5142	1.3732	1.4278	1.4847	1.4329	1.3828	1.4399	1.3904
40	1.4502	1.5077	1.5041	1.3643	1.4189	1.4752	1.4233	1.3745	1.4312	1.3816
50	1.4408	1.4983	1.4941	1.3555	1.41	1.4659	1.4138	1.3664	1.4225	1.3728
60	1.4315	1.489	1.4843	1.3469	1.4012	1.4567	1.4045	1.3583	1.4139	1.3642
70	1.4224	1.4799	1.4745	1.3383	1.3925	1.4475	1.3951	1.3503	1.4055	1.3556
80	1.4134	1.4708	1.4648	1.3299	1.3839	1.4385	1.3859	1.3424	1.3971	1.347

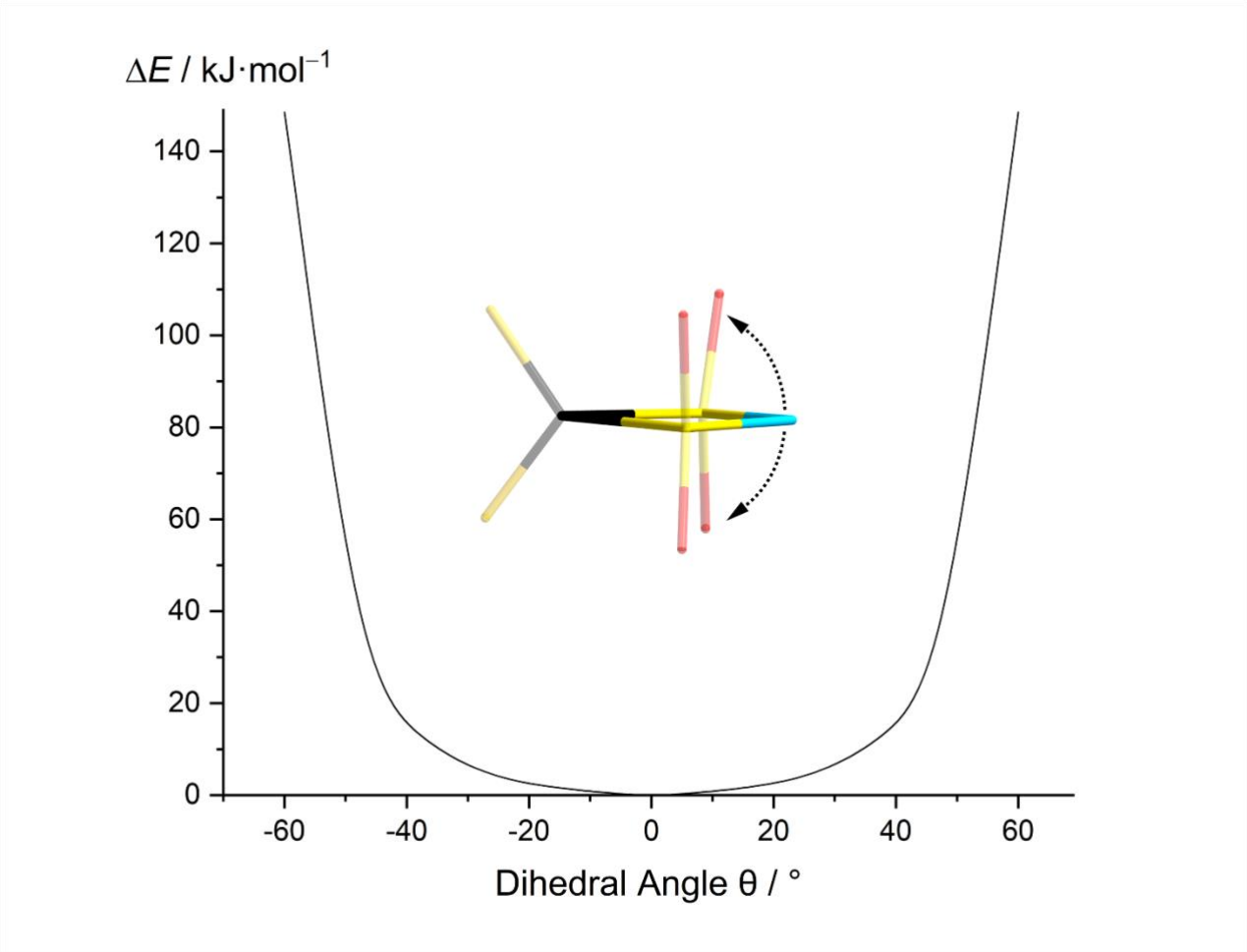

Figure S37: Change in energy for the twisting of the C−S−N−S dihedral angle in an isolated **4cPFSI** anion.

Ion Diffusion

Table S4: Temperature dependent translational self-diffusion coefficients D in $m^2 \cdot s^{-1}$ determined via PFGSTE NMR spectroscopy of the ions in neat ILs.

	[EMIm]$^+$							
T / °C	**4cPFSI**		**5cPFSI**		**6cPFSI**		**TFSI**	
	cation	anion	cation	anion	cation	anion	cation	anion
20	$3.006 \cdot 10^{-11}$	$2.388 \cdot 10^{-11}$	$3.007 \cdot 10^{-11}$	$1.939 \cdot 10^{-11}$	-	-	$4.418 \cdot 10^{-11}$	$2.545 \cdot 10^{-11}$
40	$6.618 \cdot 10^{-11}$	$5.484 \cdot 10^{-11}$	$6.256 \cdot 10^{-11}$	$4.176 \cdot 10^{-11}$	-	-	$8.990 \cdot 10^{-11}$	$5.431 \cdot 10^{-11}$
60	$1.177 \cdot 10^{-10}$	$9.823 \cdot 10^{-11}$	$1.072 \cdot 10^{-10}$	$7.276 \cdot 10^{-11}$	-	-	$1.509 \cdot 10^{-10}$	$9.361 \cdot 10^{-11}$
80	$1.906 \cdot 10^{-10}$	$1.605 \cdot 10^{-11}$	$1.722 \cdot 10^{-10}$	$1.191 \cdot 10^{-10}$	-	-	$2.405 \cdot 10^{-10}$	$1.546 \cdot 10^{-11}$
	[BMIm]$^+$							
	4cPFSI		**5cPFSI**		**6cPFSI**		**TFSI**	
	cation	anion	cation	anion	cation	anion	cation	anion
20	$1.440 \cdot 10^{-11}$	$1.180 \cdot 10^{-11}$	$1.590 \cdot 10^{-11}$	$1.179 \cdot 10^{-11}$	$6.449 \cdot 10^{-12}$	$4.315 \cdot 10^{-12}$	$2.16 \cdot 10^{-11}$	$1.62 \cdot 10^{-11}$
40	$3.724 \cdot 10^{-11}$	$3.158 \cdot 10^{-11}$	$3.782 \cdot 10^{-11}$	$2.881 \cdot 10^{-11}$	$2.004 \cdot 10^{-11}$	$1.354 \cdot 10^{-11}$	$5.16 \cdot 10^{-11}$	$3.95 \cdot 10^{-11}$
60	$7.096 \cdot 10^{-11}$	$6.177 \cdot 10^{-11}$	$7.429 \cdot 10^{-11}$	$5.720 \cdot 10^{-11}$	$4.581 \cdot 10^{-11}$	$3.266 \cdot 10^{-11}$	$9.57 \cdot 10^{-11}$	$7.52 \cdot 10^{-11}$
80	$1.282 \cdot 10^{-10}$	$1.013 \cdot 10^{-10}$	$1.239 \cdot 10^{-10}$	$9.887 \cdot 10^{-11}$	$8.509 \cdot 10^{-11}$	$8.509 \cdot 10^{-11}$	$1.64 \cdot 10^{-10}$	$1.30 \cdot 10^{-10}$
	[BMPL]$^+$							
	4cPFSI		**5cPFSI**		**6cPFSI**		**TFSI**	
	cation	anion	cation	anion	cation	anion	cation	anion
20	-	-	$9.716 \cdot 10^{-12}$	$8.090 \cdot 10^{-12}$	$3.209 \cdot 10^{-12}$	$2.345 \cdot 10^{-12}$	$1.328 \cdot 10^{-11}$	$1.091 \cdot 10^{-11}$
40	-	-	$2.329 \cdot 10^{-11}$	$1.937 \cdot 10^{-11}$	$1.096 \cdot 10^{-11}$	$8.275 \cdot 10^{-12}$	$3.281 \cdot 10^{-11}$	$2.757 \cdot 10^{-11}$
60	-	-	$4.437 \cdot 10^{-11}$	$3.722 \cdot 10^{-11}$	$2.611 \cdot 10^{-11}$	$2.035 \cdot 10^{-11}$	$6.421 \cdot 10^{-11}$	$5.491 \cdot 10^{-11}$
80	-	-	$7.962 \cdot 10^{-11}$	$7.009 \cdot 10^{-11}$	$5.299 \cdot 10^{-11}$	$4.152 \cdot 10^{-11}$	$1.166 \cdot 10^{-10}$	$1.018 \cdot 10^{-10}$

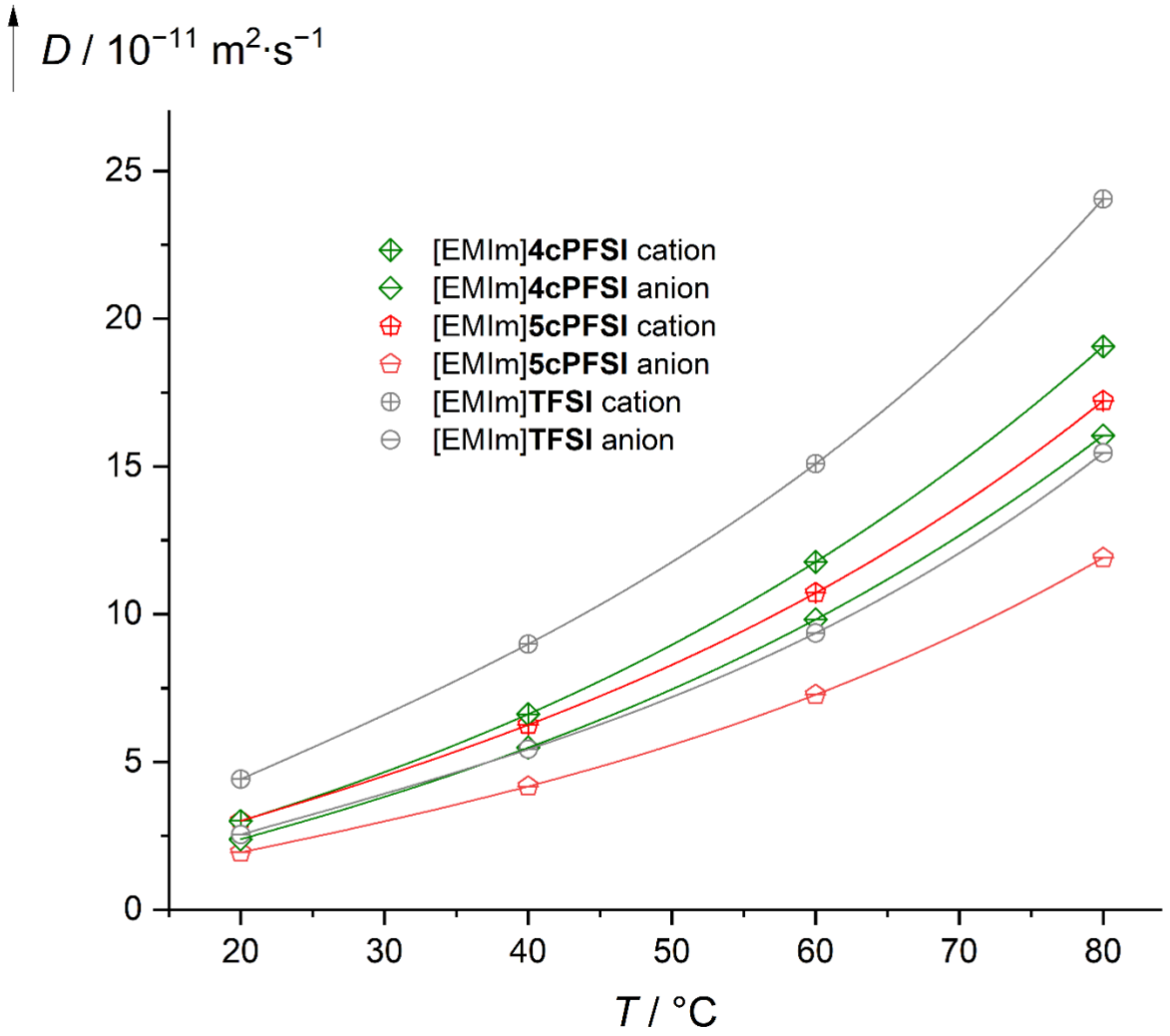

Figure S37: Translational self ion diffusion coefficients of the neat [EMIm]-RTILs at different temperatures determined via PFGSTE NMR spectroscopy.

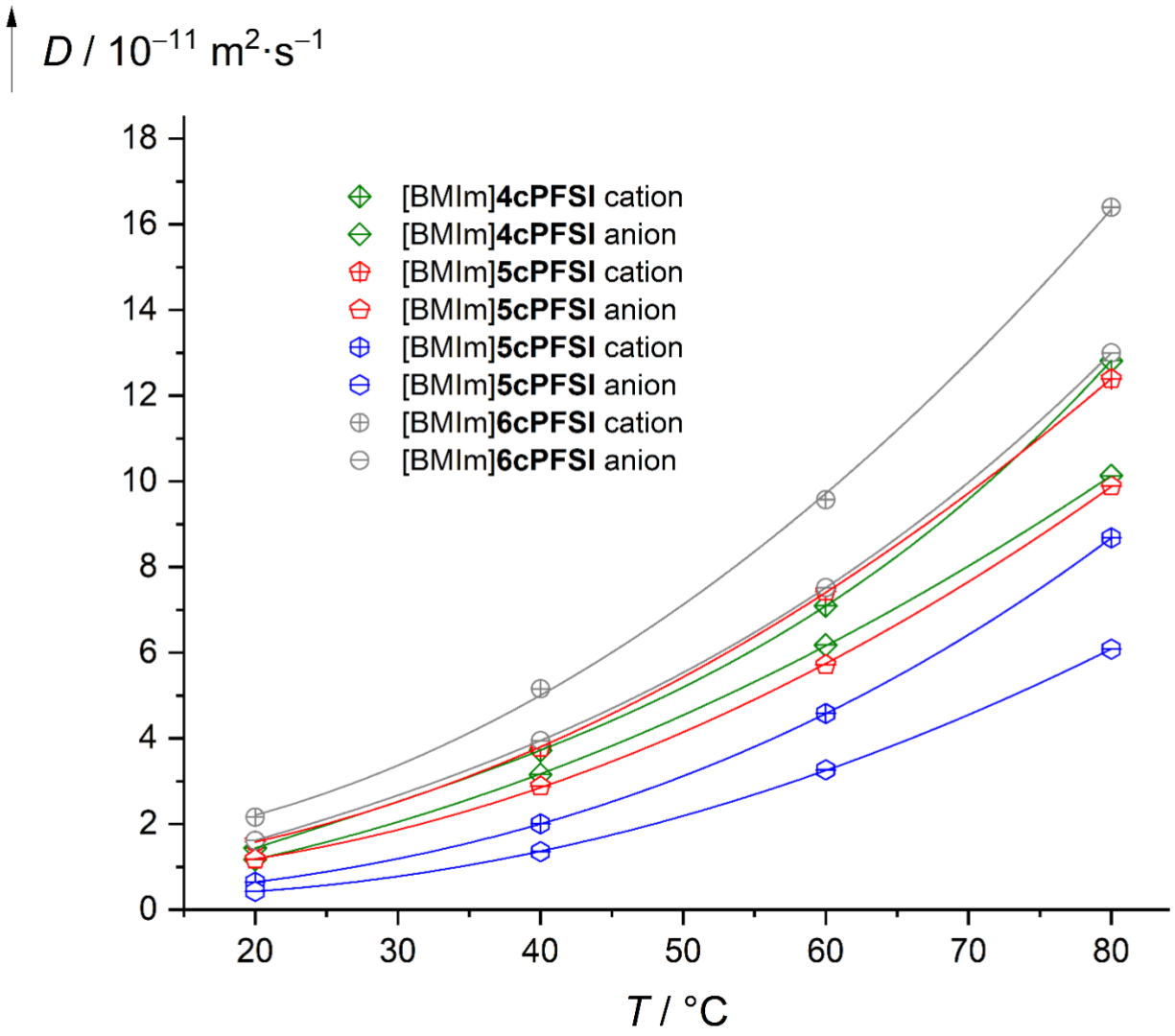

Figure S38: Translational self ion diffusion coefficients of the neat [BMIm]-RTILs at different temperatures determined via PFGSTE NMR spectroscopy.

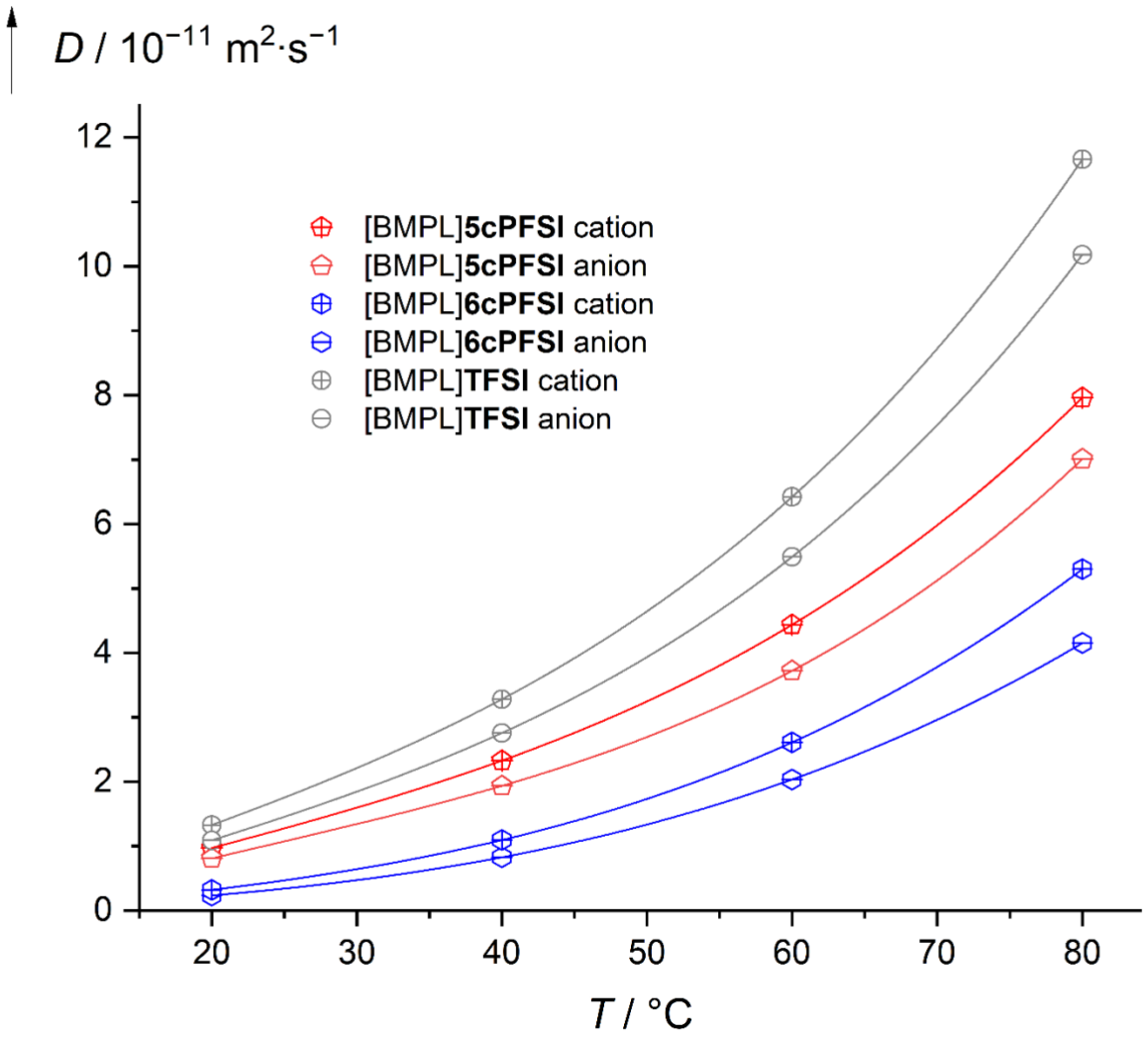

Figure S40: Translational self ion diffusion coefficients of the neat [BMPL]-RTILs at different temperatures determined via PFGSTE NMR spectroscopy.

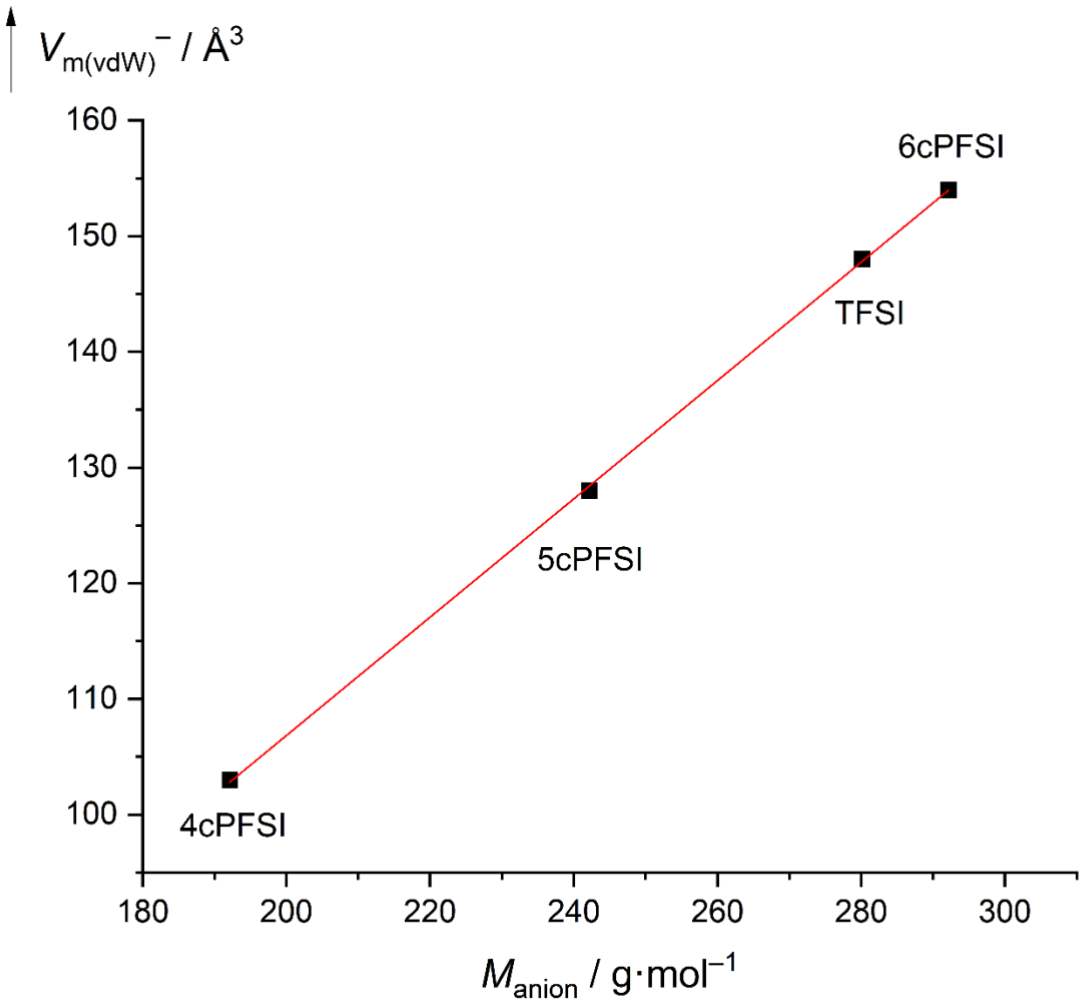

Figure S41: Linear increase of anion volume $V_{m(vdW)}^-$ (Olex2) with increasing anion mass M_{anion} (see Table 2).

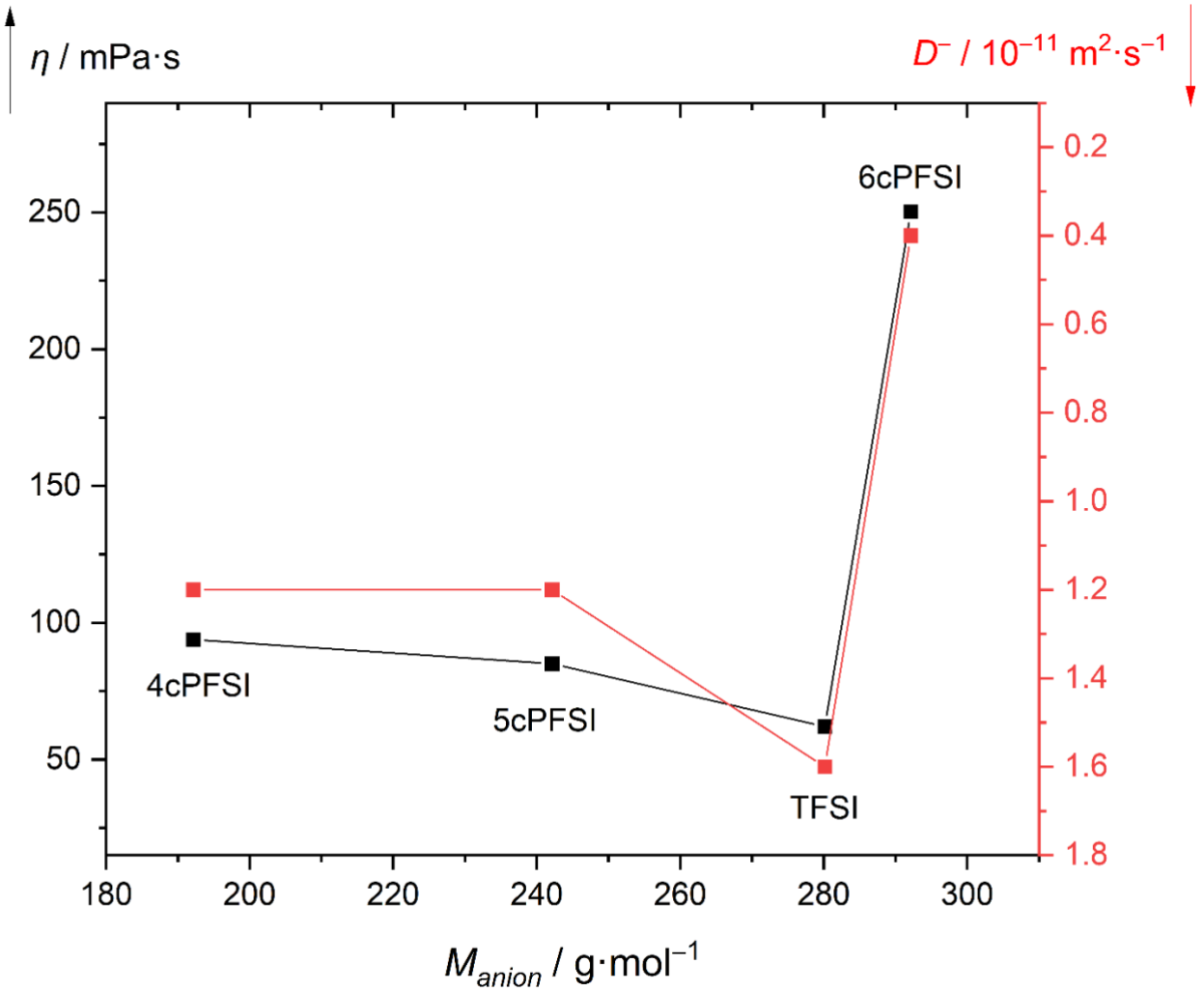

Figure S42: Dynamic viscosity η and diffusion coefficients of the anion D^- of the neat [BMIm]-ionic liquids in relation to the molar mass of the anion at 20 °C.

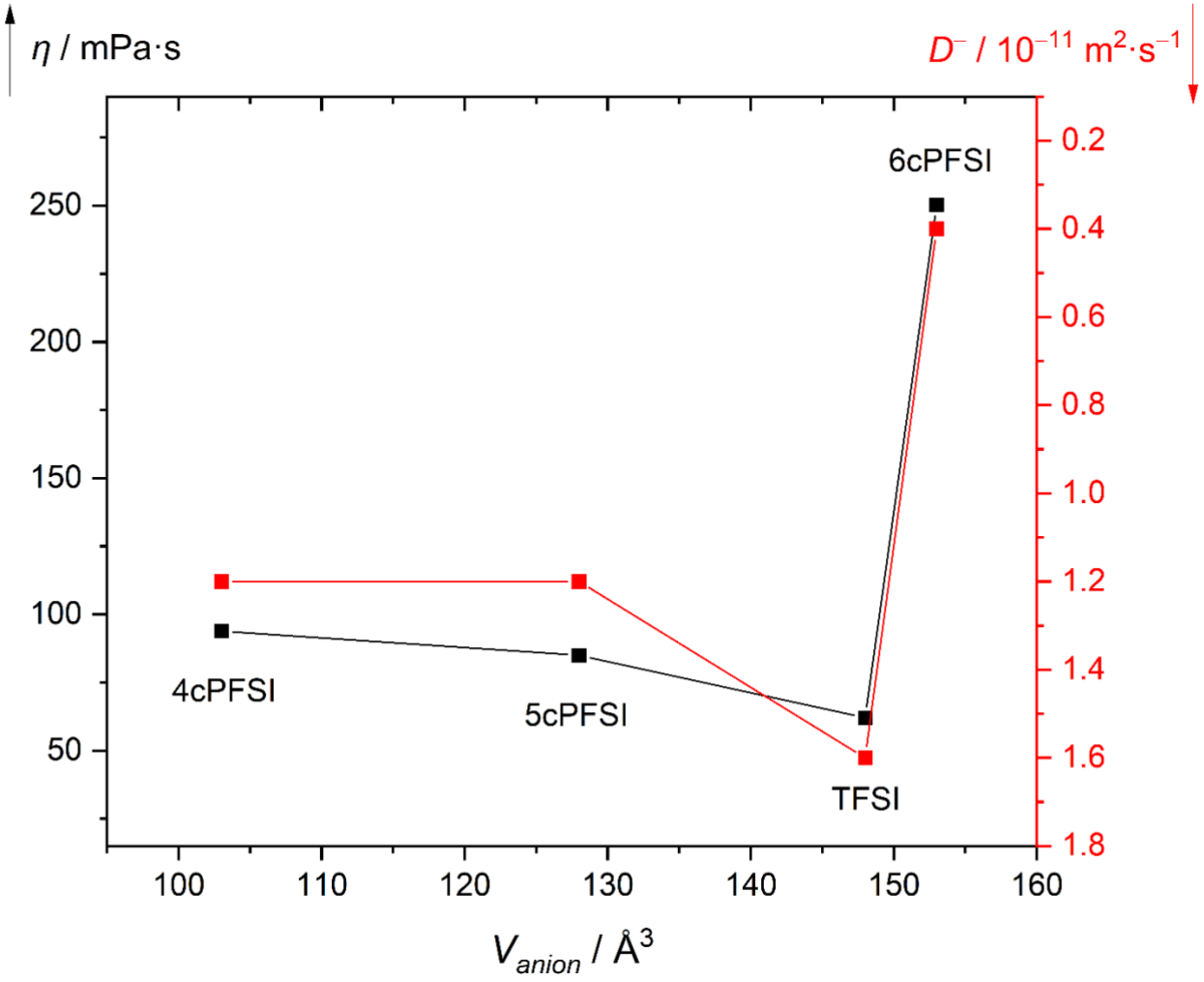

Figure S39: Dynamic viscosity η and diffusion coefficients of the anion D^- of the neat [BMIm]-ionic liquids in relation to the volume $V_{m(vdW)}^-$(Olex2) of the anion at 20 °C.

Crystallographic Data

Crystal Growth

Single crystals of [EMIm]**4cPFSI** were obtained by storing a liquid sample of [EMIm]**4cPFSI** at 15 °C for several days. Single crystals of [EMIm]**6cPFSI**, [BMIm]**6cPFSI**, [BMPL]**4cPFSI** and [BMPL]**6cPFSI** were obtained by slow vapour evaporation of a saturated acetone solution of the respective salt. Single crystals of [BMIm][Ag(**4cPFSI**)$_2$] and [BMPL][Ag(**4cPFSI**)$_2$] were obtained by slow cooling of a hot saturated aqueous solution of the respective salt to room temperature and [EMIm][Ag(**4cPFSI**)$_2$] crystallized from an aqueous solution at room temperature.

A single crystal of $C_8H_{11}F_4N_3O_4S_2$ ([EMIm]**5cPFSI**]) – that is liquid at room temperature – was grown *in situ* at 258.8 K by manually generating a crystal seed, afterwards cooled to 240 K with 1 K/h, to 190 K with 50 K/h and to 100 K 360 K/h. For X-Ray diffraction studies suited single crystals of [BMIm]**4cPFSI**, [BMIm]**5cPFSI**, [BMIm]***cis*TFSI** and [BMPL]**5cPFSI** were prepared in a similar fashion to the single crystal of [EMIm]**5cPFSI**. The general procedure of this process was previously reported.[24-29] Samples of the respective ionic liquid were loaded into glass capillaries with 0.28 mm inside diameter. The filled capillaries were cooled on the diffractometer in a nitrogen gas stream from an Oxford cryosystem attachment. The following steps until data collection were monitored manually under an optical microscope with polarizer. After repeated freezing and heating of the samples to a polycrystalline state the samples were heated just below their respective melting points to slow down nucleation. Manual local heating in the next step with a thin copper wire reduced the number of crystalline domains ideally so that only a single seed is left. By slow cooling the crystal slowly grows until a single specimen fills the entire cooled area, afterwards it was cooled to 100 K for data collection. (In the case of [BMPL]**5cPFSI** a precautionary collected dataset at 238.5 K gave data of better quality than the dataset at 100 K, presumably because of crystal cracking in the capillary at temperatures under 238.5 K.)

CCDC 2155593, 2222987–2222997 and 2236907 contain the supplementary crystallographic data for this paper. These data can be obtained free of charge from The Cambridge Crystallographic Data Centre via www.ccdc.cam.ac.uk/conts/retrieving.html

Table S5: Selected crystal data and details of the refinement of the crystal structures of perfluorosulfonimide salts in this study.

	[EMIm]**4cPFSI**	[EMIm]**5cPFSI**	[EMIm]**6cPFSI**	[BMIm]**4cPFSI**	[BMIm]**5cPFSI**	[BMIm]**6cPFSI**
Formula	$C_7H_{11}F_2N_3O_4S_2$	$C_8H_{11}F_4N_3O_4S_2$	$C_9H_{11}F_6N_3O_4S_2$	$C_9H_{15}F_2N_3O_4S_2$	$C_{10}H_{15}F_4N_3O_4S_2$	$C_{11}H_{15}F_6N_3O_4S_2$
M_W	303.31	353.32	403.33	331.36	381.37	431.38
T (K)	100.0(1)	100.0(1)	100.0(4)	100(2)	100(2)	100(2)
Crystal system	triclinic	triclinic	triclinic	orthorhombic	triclinic	orthorhombic
Crystal group	*P–1*	*P–1*	*P–1*	Pbca	*P–1*	$Pca2_1$
a (Å)	7.9455(2)	8.3226(4)	10.1756(2)	8.97620(10)	8.13260(10)	18.1649(3)
b (Å)	8.6095(2)	9.9577(5)	11.1177(2)	18.01580(10)	11.59110(10)	8.37470(10)
c (Å)	9.9932(2)	10.0572(5)	14.7584(3)	35.4048(2)	17.27710(10)	23.0541(5)
α(°)	95.988(2)	91.536(4)	71.995(2)	90	104.2340(10)	90
β (°)	110.473(2)	113.802(5)	74.529(2)	90	95.3260(10)	90
γ(°)	105.270(2)	111.884(5)	89.874(2)	90	92.3130(10)	90
Volume ($Å^3$)	603.04(3)	692.05(7)	1524.43(6)	5725.43(8)	1568.45(3)	3507.12(10)
Z	2	2	4	16	4	8
ρ (calcd) ($Mg \cdot m^{-3}$)	1.670	1.696	1.757	1.538	1.615	1.634
μ (mm^{-1})	4.413	0.450	4.062	3.770	3.717	3.573
F(000)	312	360.0	816	2752	784	1760
No. of collected reflections	12566	13781	31730	81088	78666	48562
No. of unique reflections	2520	4485	6388	6246	6305	7532
R(int)	0.0324	0.0227	0.0435	0.0848	0. 0559	0.0693
No. of parameters / restraints	175 / 18	192 / 0	437 / 0	532 / 714	419 / 0	474 / 1
$R1$ ($I > 2\sigma(I)$)	0.0325	0.0379	0.0356	0.0455	0.0530	0.0577
*wR*2 (all)	0.0822	0.0430	0.0989	0.1335	0.1503	0.1676
GOF on F^2	1.053	1.096	1.085	1.056	1.083	1.073
Largest diff. peak / hole / e $Å^{-3}$	0.380 / −0.443	0.59 / −0.37	0.684 / −0.591	0.473 / −0.523	0.950 / −0.723	0.479 / −0.540
CCDC no.	2222987	2155593	2222988	2222989	2222991	2222990

Table S5 (continued): Selected crystal data and details of the refinement of the crystal structures of perfluorosulfonimide salts in this study.

	[BMIm]**TFSI**	[BMIm][Ag(**4cPFSI**)$_2$]	[BMPL]**4cPFSI**	[BMPL]**5cPFSI**	[BMPL]**6cPFSI**	[BMPL][Ag(**4cPFSI**)$_2$]	[EMIm][Ag(**4cPFSI**)$_2$]
Formula	$C_{20}H_{30}F_{12}N_6O_8S_4$	$C_{10}H_{15}AgF_4N_4O_8S_4$	$C_{10}H_{20}F_2N_2O_4S_2$	$C_{11}H_{20}F_4N_2O_4S_2$	$C_{12}H_{20}F_6N_2O_4S_2$	$C_{11}H_{20}AgF_4N_3O_8S_4$	$C_8H_{11}AgF_4N_3O_8S_4$
M_W	838.74	631.37	334.40	383.40	434.42	634.41	603.32
T (K)	100.0(1)	99.9(6)	100.0(1)	238.5(1)	100.0(1)	100.0(1)	100.0(1)
Crystal system	monoclinic	monoclinic	orthorhombic	monoclinic	triclinic	triclinic	triclinic
Crystal group	$P2_1/n$	$P2_1$	$P2_12_12_1$	$P2_1/n$	*P–1*	*P–1*	*P–1*
a (Å)	12.06090(10)	5.66760(10)	9.23070(10)	8.25097(18)	8.98100(10)	9.5881(2)	5.90590(10)
b (Å)	8.45970(10)	16.1685(2)	9.63750(10)	10.3115(2)	9.36560(10)	10.8805(2)	8.2250(2)
c (Å)	34.0782(2)	11.19100(10)	16.68630(10)	19.7803(5)	11.9008(2)	11.46900(10)	10.7395(2)
α(°)	90	90	90	90	70.2070(10)	87.9790(10)	103.427(2)
β (°)	93.1180(10)	98.4150(10)	90	98.622(2)	75.4030(10)	78.6440(10)	101.901(2)
γ(°)	90	90	90	90	71.8690(10)	64.936(2)	107.938(2)
Volume (Å^3)	3471.91(5)	1014.46(2)	1484.43(2)	1663.88(6)	882.98(2)	1061.04(3)	460.500(18)
Z	4	2	4	4	2	2	1
ρ (calcd) (Mg·m^{-3})	1.605	2.067	1.496	1.531	1.634	1.986	2.176
μ (mm^{-1})	3.59	12.638	3.614	3.485	3.532	12.068	1.635
F(000)	1712	628	704	796	448	636	298
No. of collected reflections	15297	30101	15901	21683	51553	42613	45791
No. of unique reflections	15297	3859	3115	3488	3811	4446	4882
R(int)	0.10	0.1177	0.0420	0.1804	0.1347	0.2085	0.0606
No. of parameters / restraints	491 / 97	283 / 1	183 / 0	210 / 0	237 / 0	430 / 498	166 / 0
$R1$ (I > 2σ(I))	0.0994	0.0379	0.0279	0.0906	0.0698	0.0556	0.0273
$wR2$ (all)	0.2149	0.1064	0.0718	0.2872	0.1931	0.1553	0.0723
GOF on F^2	2.948	1.037	1.063	1.150	1.062	1.063	1.042
Largest diff. peak / hole / e Å^{-3}	0.990 / −1.029	1.285 / −0.733	0.284 / −0.407	0.642 / −0.580	1.229 / −0.613	1.368 / −2.373	1.143 / –0.768
CCDC no.	2222992	2222993	2222994	2222995	2222996	2222997	2236907

Table S6: Selected averaged bond lengths [Å] and angles [°] of specified anions in the crystalline state of respective salts.

	[EMIm]$^+$				[BMIm]$^+$					[BMPL]$^+$			
	4cPFSI	**5cPFSI**	**6cPFSI**	[Ag(**4cTFSI**)$_2$]$^-$	**4cPFSI**^{a}	**5cPFSI**^{a}	**6cPFSI**	***cis*TFSI**	[Ag(**4cTFSI**)$_2$]$^-$	**4cPFSI**	**5cPFSI**	**6cPFSI**	[Ag(**4cTFSI**)$_2$]$^-$
S−N	1.605(2)	1.5874(1)	1.583(2)	1.6223(12)	1.602(2)	1.590(2)	1.584(6)	1.576(3)	1.623(6)	1.611(2)	1.581(4)	1.586(3)	1.619(3)
S=O	1.439(2)	1.4324(1)	1.430(1)	1.435(2)	1.435(2)	1.428(2)	1.425(5)	1.432(3)	1.433(7)	1.437(2)	1.417(4)	1.430(3)	1.426(3)
S−C	1.855(2)	1.8523(1)	1.837(2)	1.8546(2)	1.851(2)	1.853(4)	1.840(9)	1.835(5)	1.851(8)	1.859(2)	1.840(4)	1.845(3)	1.842(3)
C−F	1.331(2)	1.3407(1)	1.347(3)	1.317(2)	1.329(2)	1.335(4)	1.345(9)	1.324(6)	1.32(1)	1.328(3)	1.321(5)	1.349(4)	1.319(4)
C−C	-	1.5468(1)	1.544(3)	-	-	1.556(5)	1.537(9)	-	-	-	1.529(6)	1.543(4)	-
Ag−N	-	-	-	2.1446(12)	-	-	-	-	2.149(6)	-	-	-	2.138(3)
S−C−S	83.91(7)	-	-	85.79(5)	83.88(8)	-	-	-	85.7(3)	83.92(2)	-	-	85.9(1)
S−N−S	101.22(8)	112.933(4)	120.29(9)	102.05(7)	101.10(9)	113.06(15)	119.7(4)	127.26(18)	101.7(3)	101.1(1)	113.2(2)	119.8(2)	101.7(2)
N−Ag−N	-	-	-	180	-	-	-	-	178.7(3)	-	-	-	166.6(1)
∑(ring)	359.95(14)	519.792(4)	664.11(9)	359.9(1)	359.66(8)	521.1(3)	665.9(4)	-	359.9(4)	359.0(1)	522.9(3)	663.2(3)	359.82(2)

^{a}Crystallographically independent anion with disorder disregarded.

Hirshfeld Surface Analysis

Table S7: Relative percentage contributions of selected cation-anion; anion-anion and cation-cation contacts to the whole Hirshfeld surface of the ion.

	[EMIm]$^+$				[BMIm]$^+$				[BMPL]$^+$			
	4cPFSI	**5cPFSI**	**6cPFSI**	***cis*TFSI**	**4cPFSI**	**5cPFSI**	**6cPFSI**	***cis*TFSI**	**4cPFSI**	**5cPFSI**	**6cPFSI**	***trans*TFSI**
S=O···H	50.3	43.5	35.5	34.1/35.5	52.2/54.3	42.5/43.6	35.1	34.1/35.5	46.1	44.2	35.1	37.5
S−N···H	7.3	6.1	5.2	3.8/3.9	9.4/9.8	4.3/4.5	3.5	3.8/3.9	10.5	5.9	3.5	4.1
C−F···H	17.2	26.2	29.5	31.7/30.5	19.4/19.4	23.3/21.1	41.7	31.7/30.5	19.0	38.0	41.7	48.1
C−F···F	2.6	10.8	18.2	19.2/19.9	4.0/3.9	15.5/11.7	11.5	19.2/19.9	0.0	0.0	11.5	9.3
C−H···H	35.2	24.8	20.2	21.5/22.5	44.4/43.5	39.8/39.9	39.6	22.5/21.5	57.5	41.2	39.6	28.4

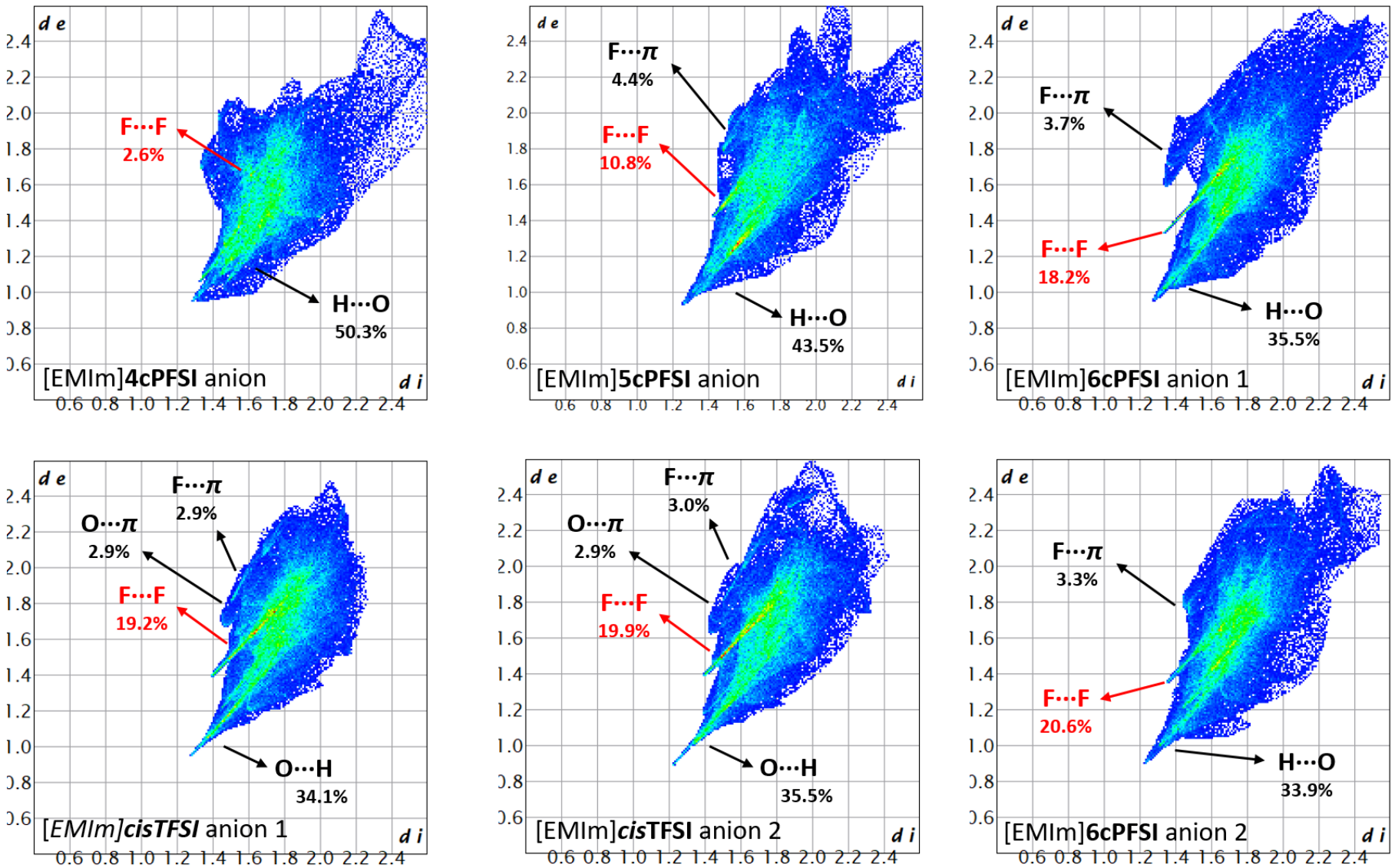

Figure S40: 2D fingerprint plots of the anions in [EMIm]-ILs in this study.

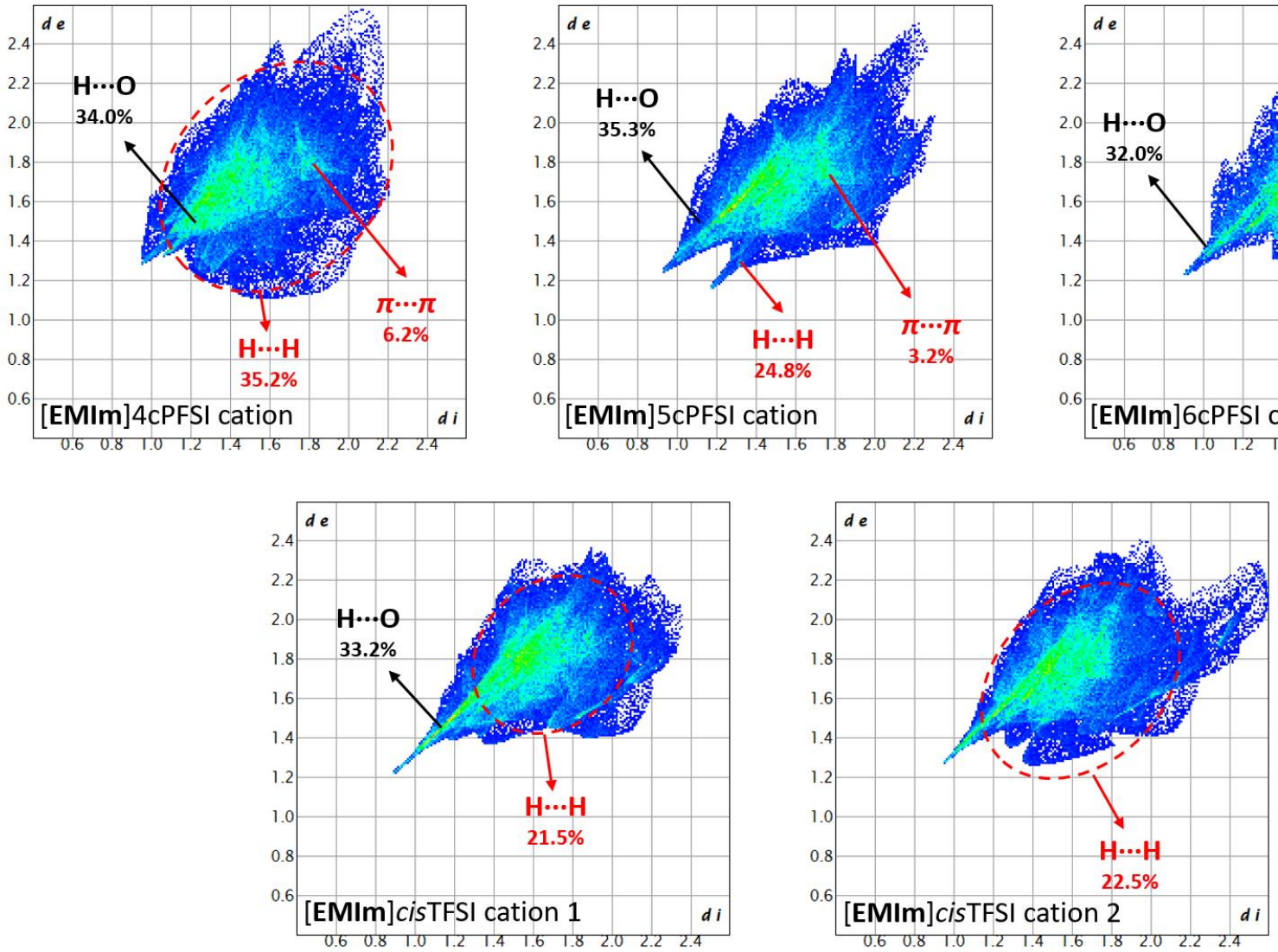

Figure S41: 2D fingerprint plots of the cations in [EMIm]-ILs in this study. The dashed circles mark large, diffuse interaction areas without high interaction occurrence for the respective contact.

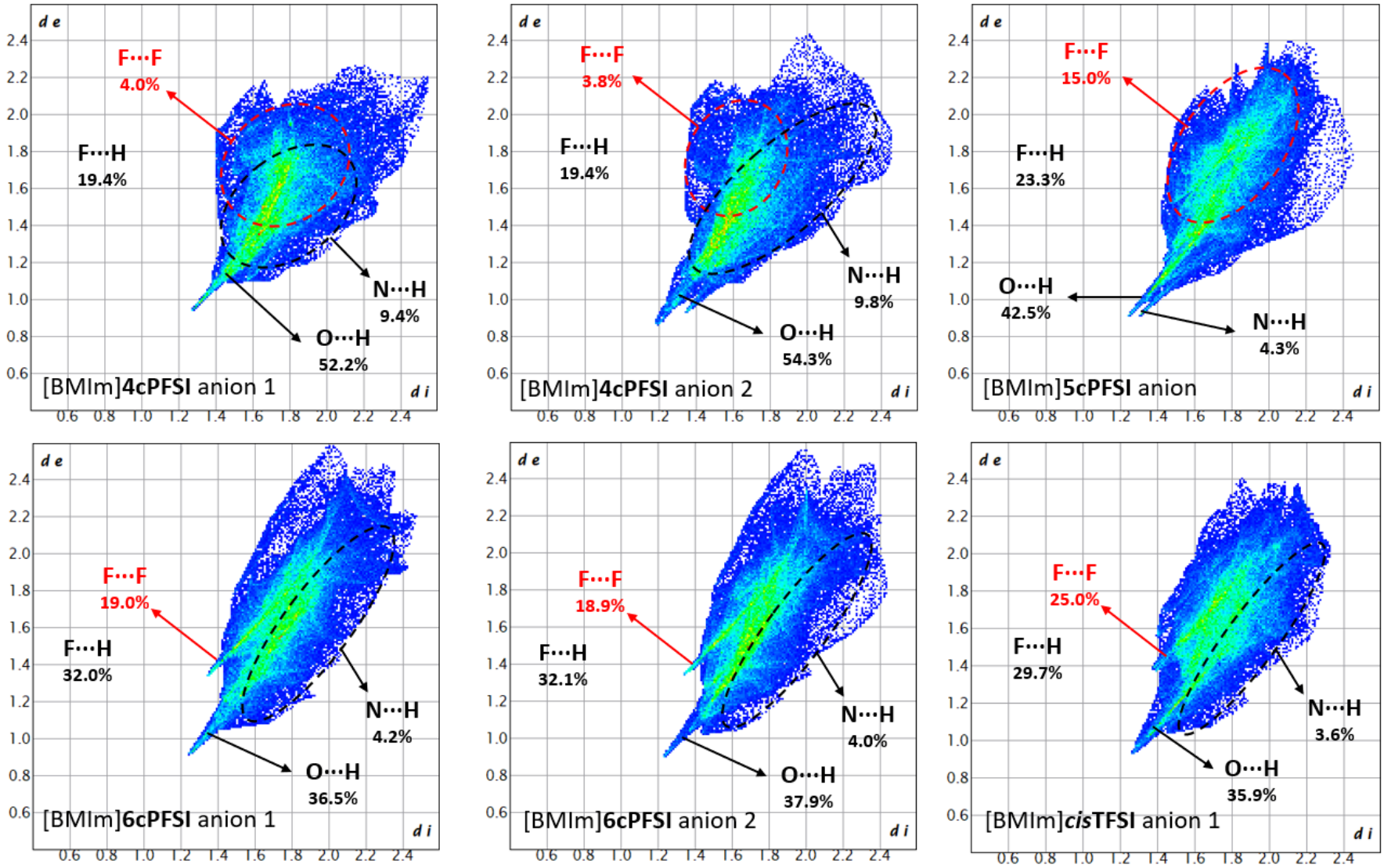

Figure S46: 2D fingerprint plots of the anions in [BMIm]-ILs in this study. The dashed circles mark large, diffuse interaction areas without high interaction occurrence for the respective contact.

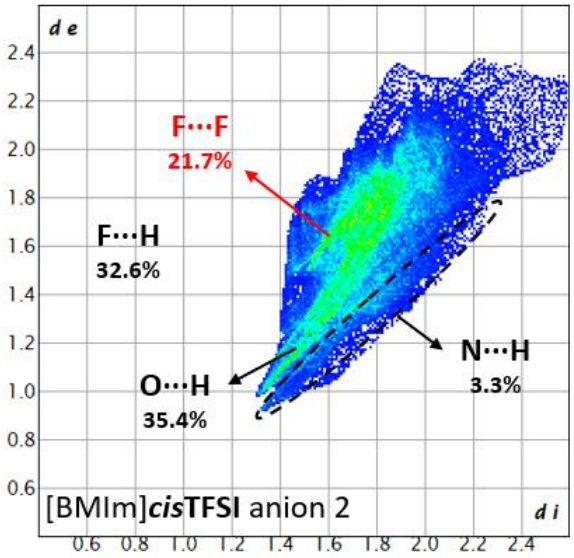

Figure S46 (continued): 2D fingerprint plots of the anions in [BMIm]-ILs in this study. The dashed circles mark large, diffuse interaction areas without high interaction occurrence for the respective contact.

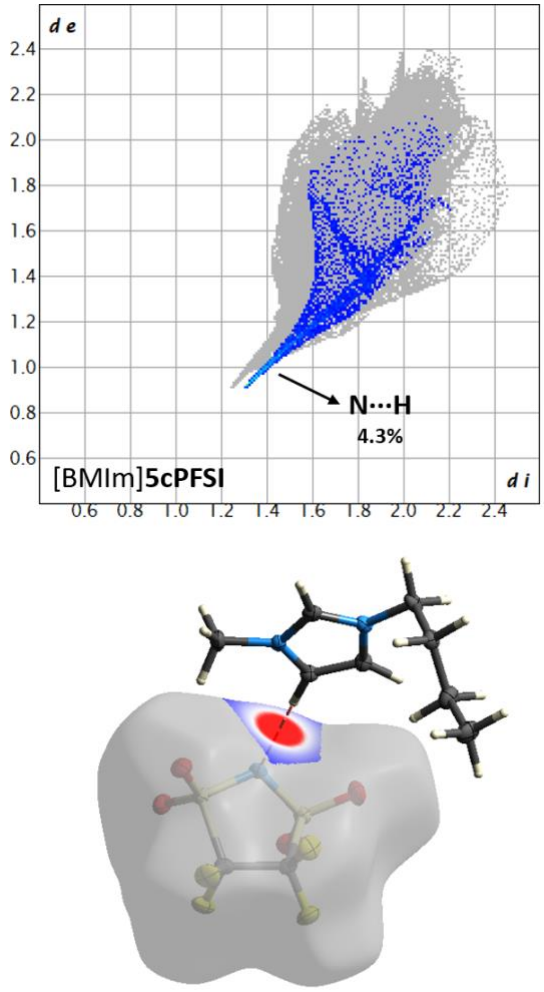

Figure S47: Example for characteristic N···H contacts (blue) in the 2D fingerprint plot of **5cPFSI** in the crystalline phase of [BMIm]**5cPFSI** (top) and corresponding part of the Hirshfeld surface with d_{norm} mapped onto it (bottom).

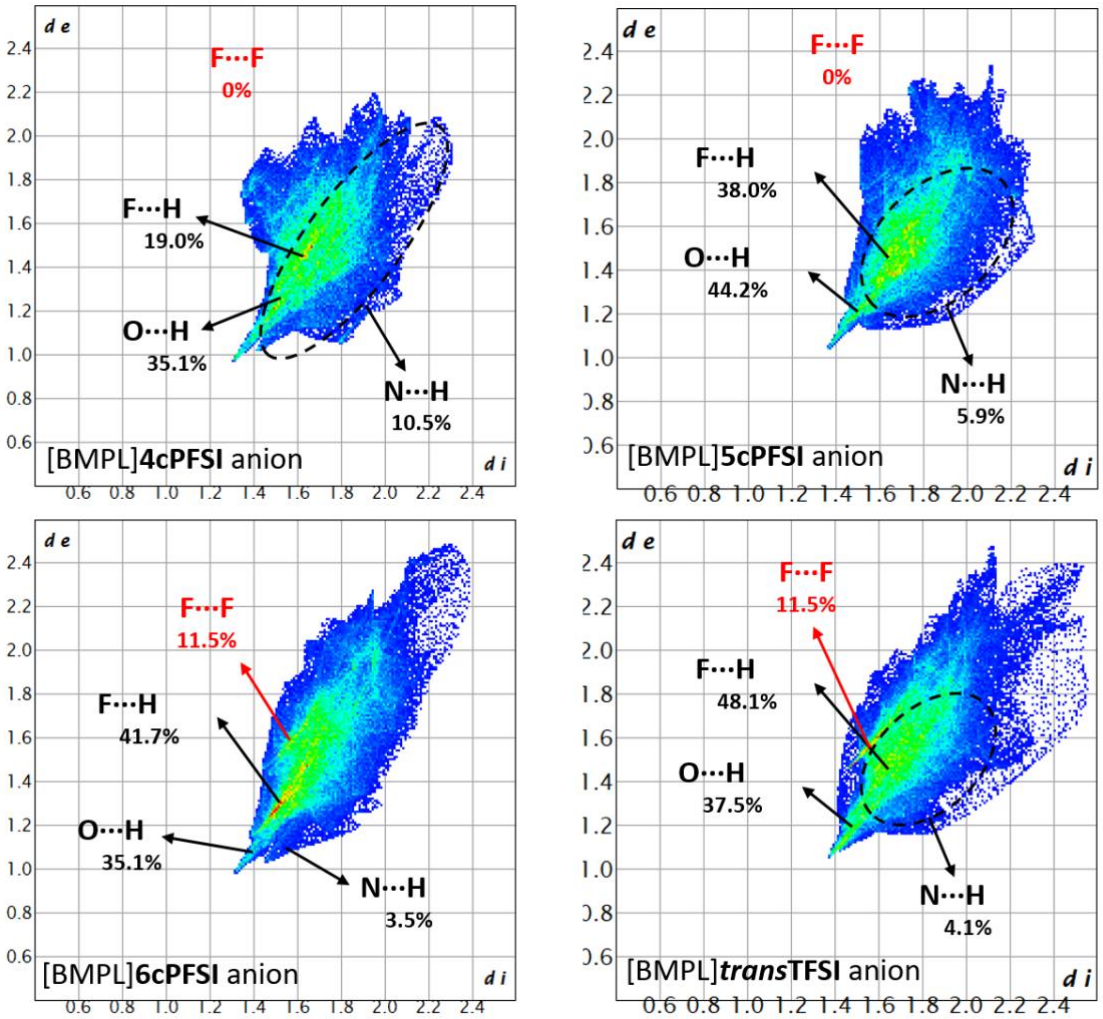

Figure S42: 2D fingerprint plots of the anions in [BMPL]-ILs in this study. The dashed circles mark large, diffuse interaction areas without high interaction occurence for the respective contact.

DSC analysis

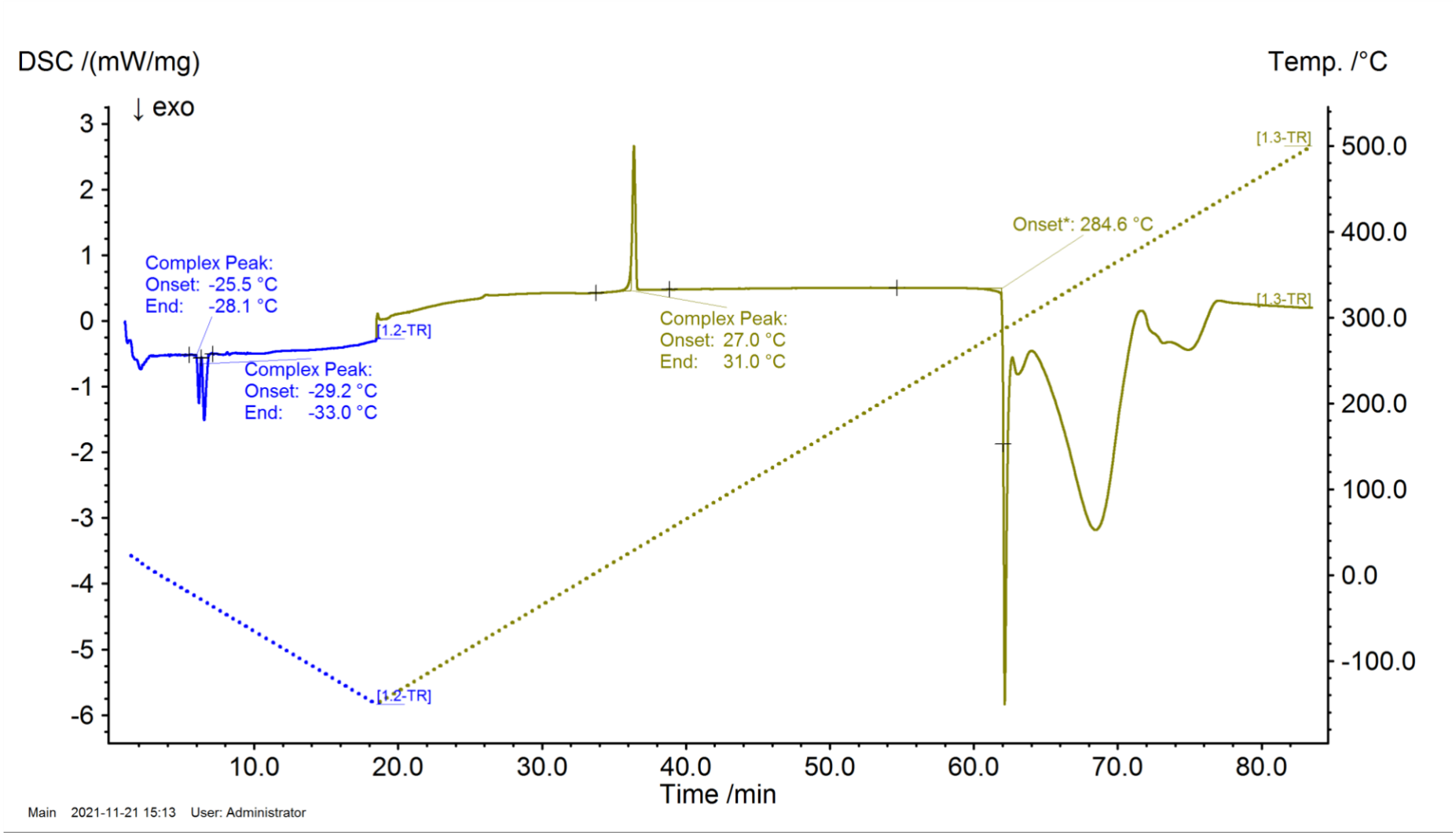

Figure S43: DSC curve of [EMIm]**4cPFSI** (10 K/min).

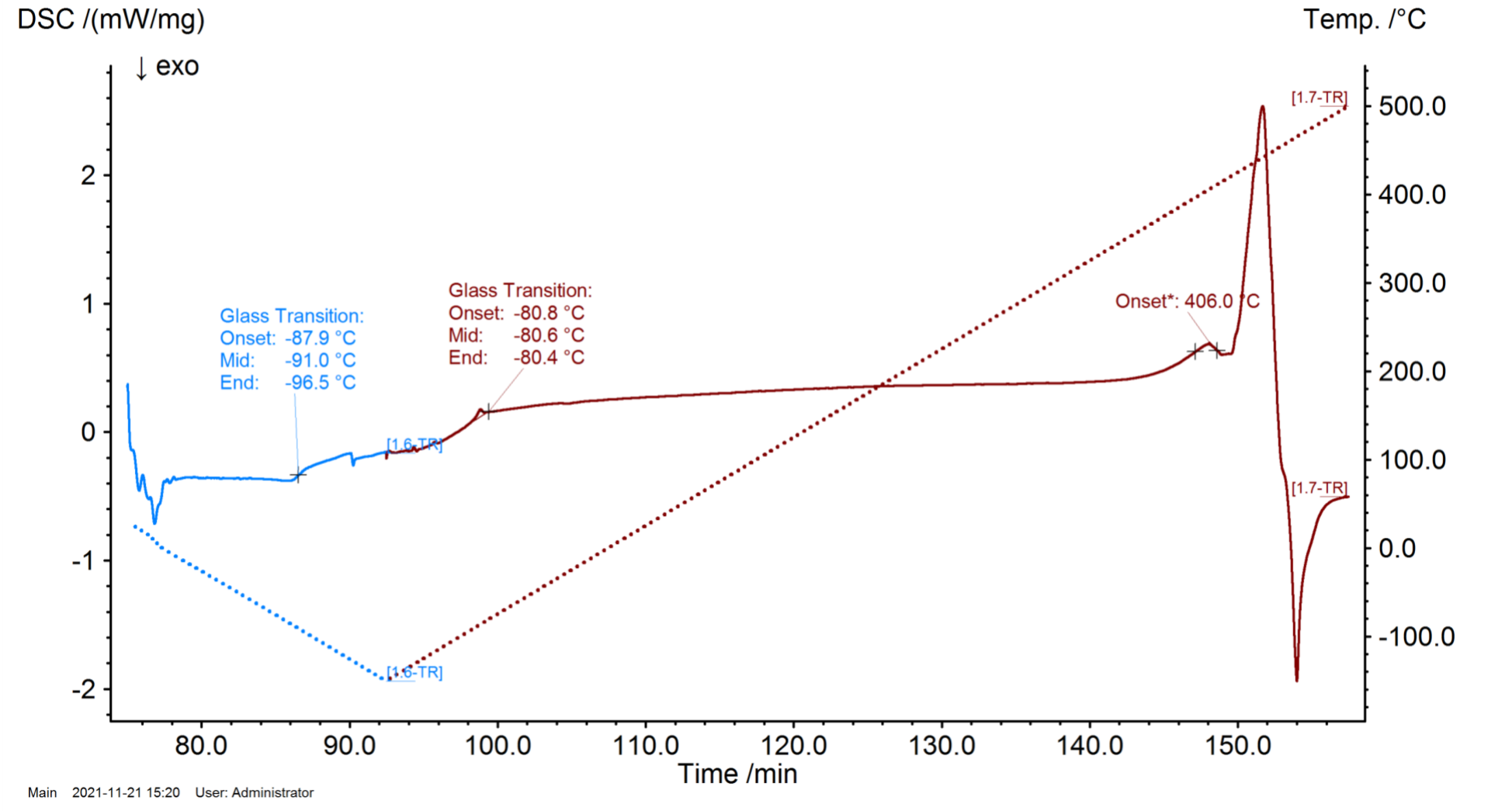

Figure S50: DSC curve of [EMIm]**5cPFSI** (10 K/min).

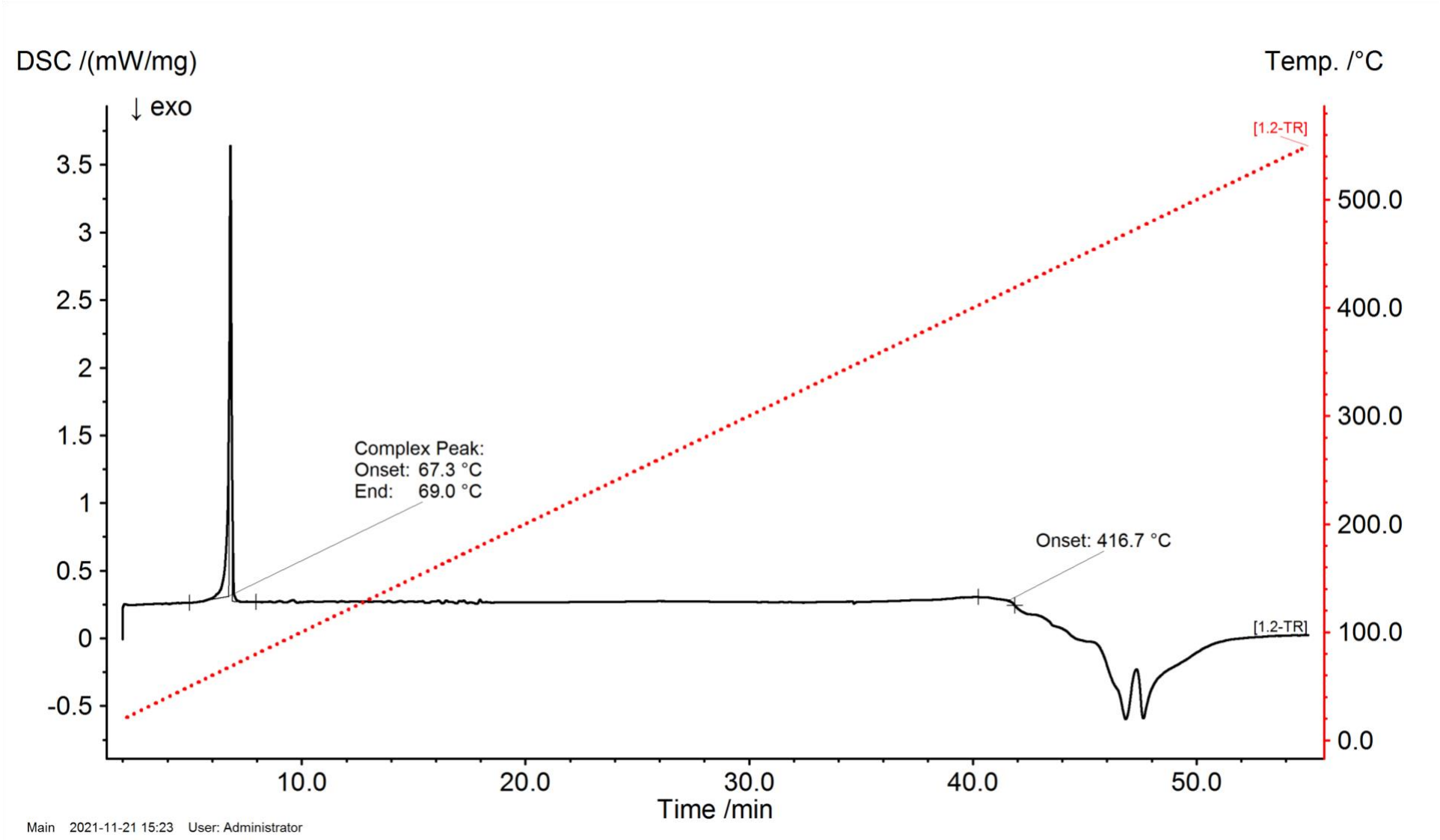

Figure S51: DSC curve of [EMIm]**6cPFSI** (10 K/min).

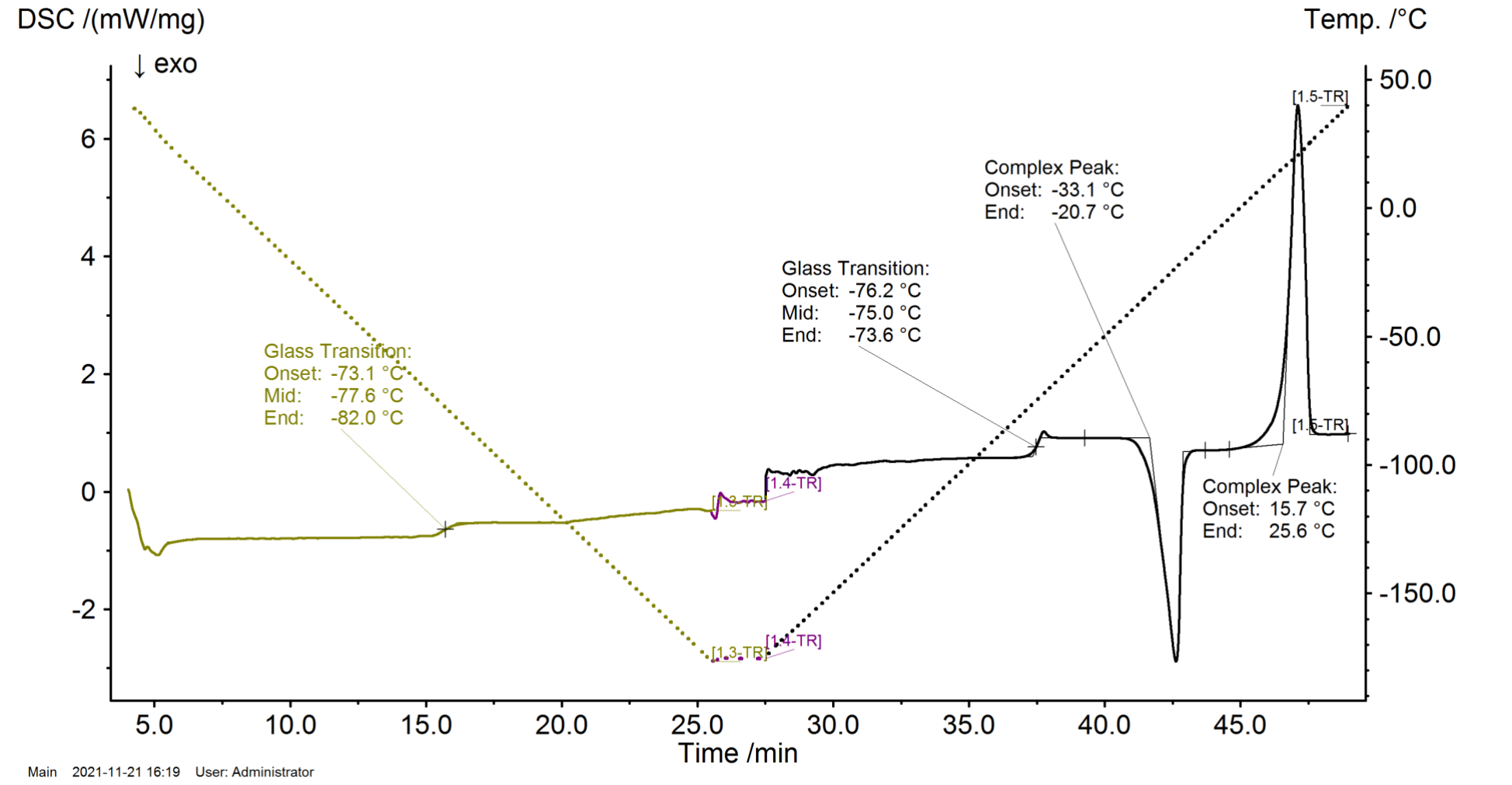

Figure S52: DSC curve of [BMIm]**4cPFSI** (without decomposition; 10 K/min).

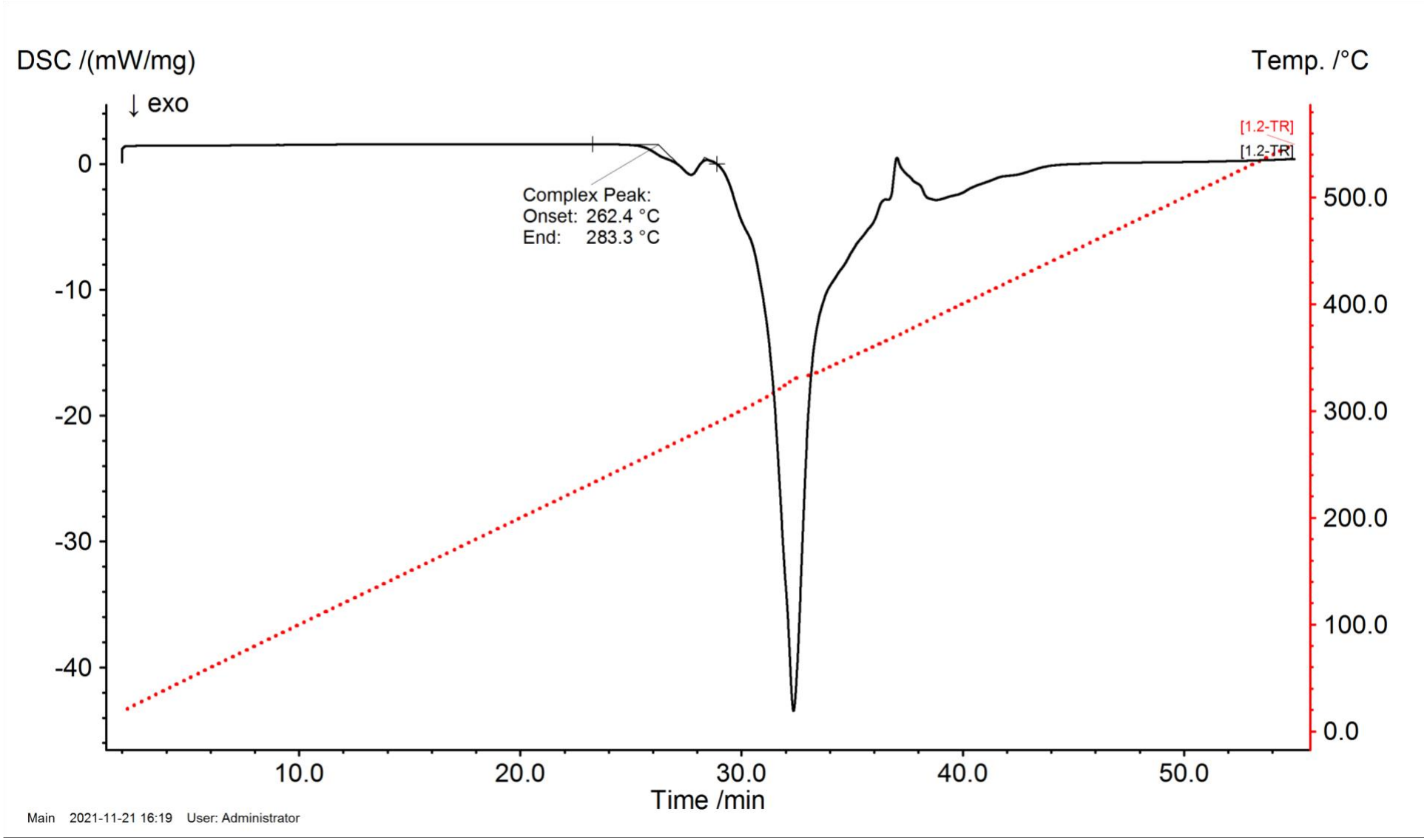

Figure S53: DSC curve of [BMIm]**4cPFSI** (only decomposition; 10 K/min).

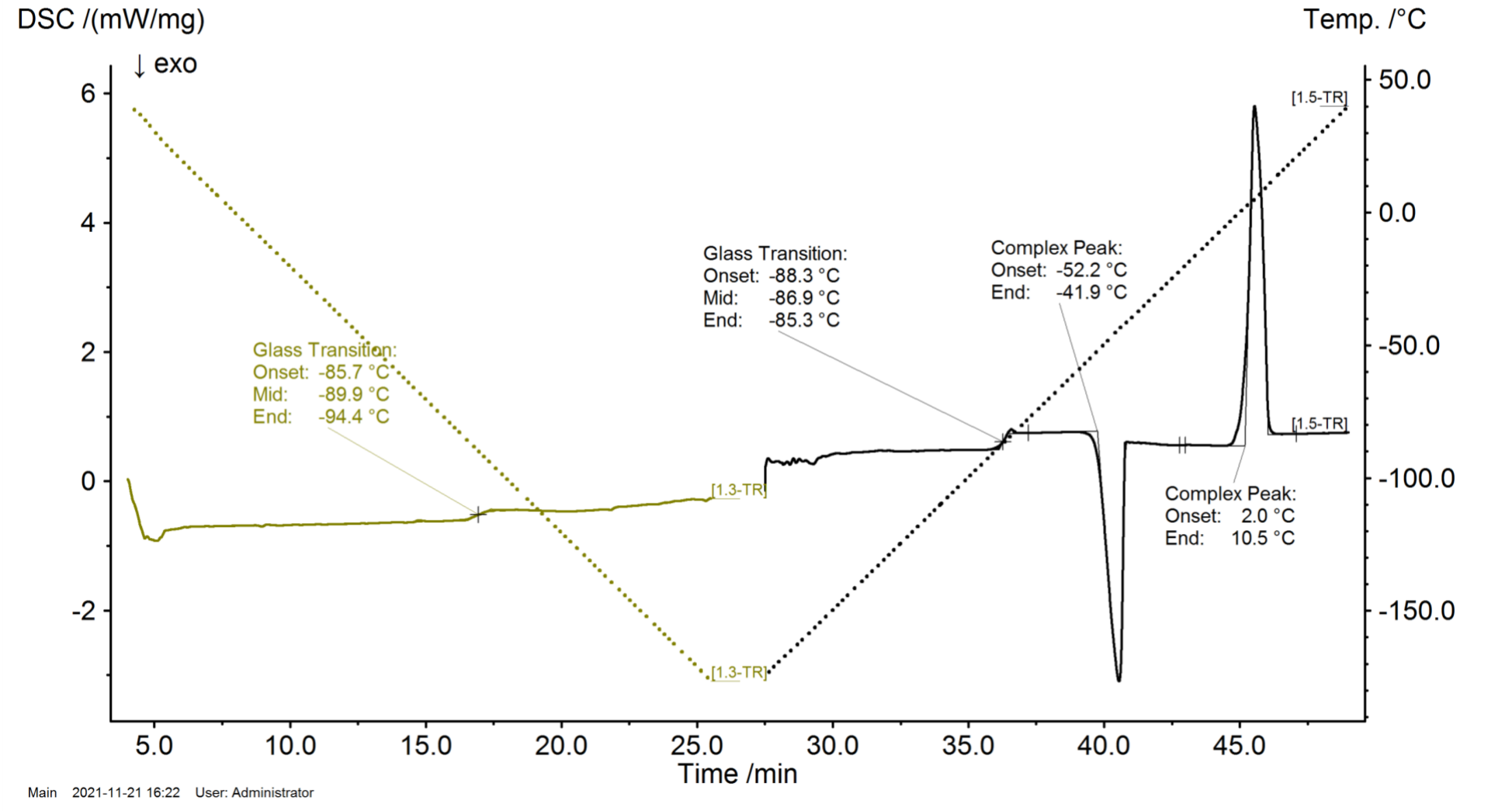

Figure S54: DSC curve of [BMIm]**5cPFSI** (without decomposition; 10 K/min).

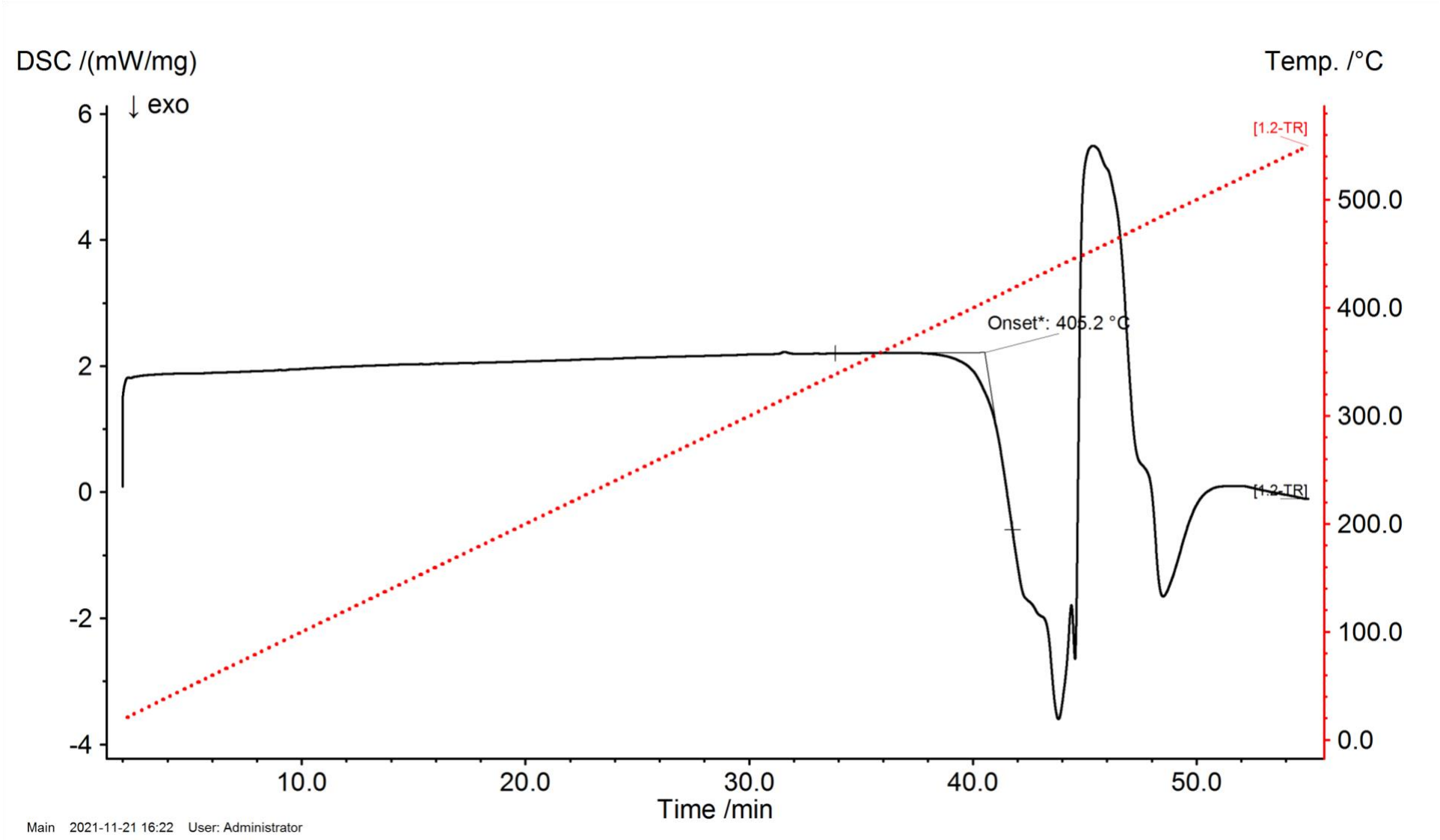

Figure S55*: DSC curve of [BMIm]**5cPFSI** (only decomposition; 10 K/min).*

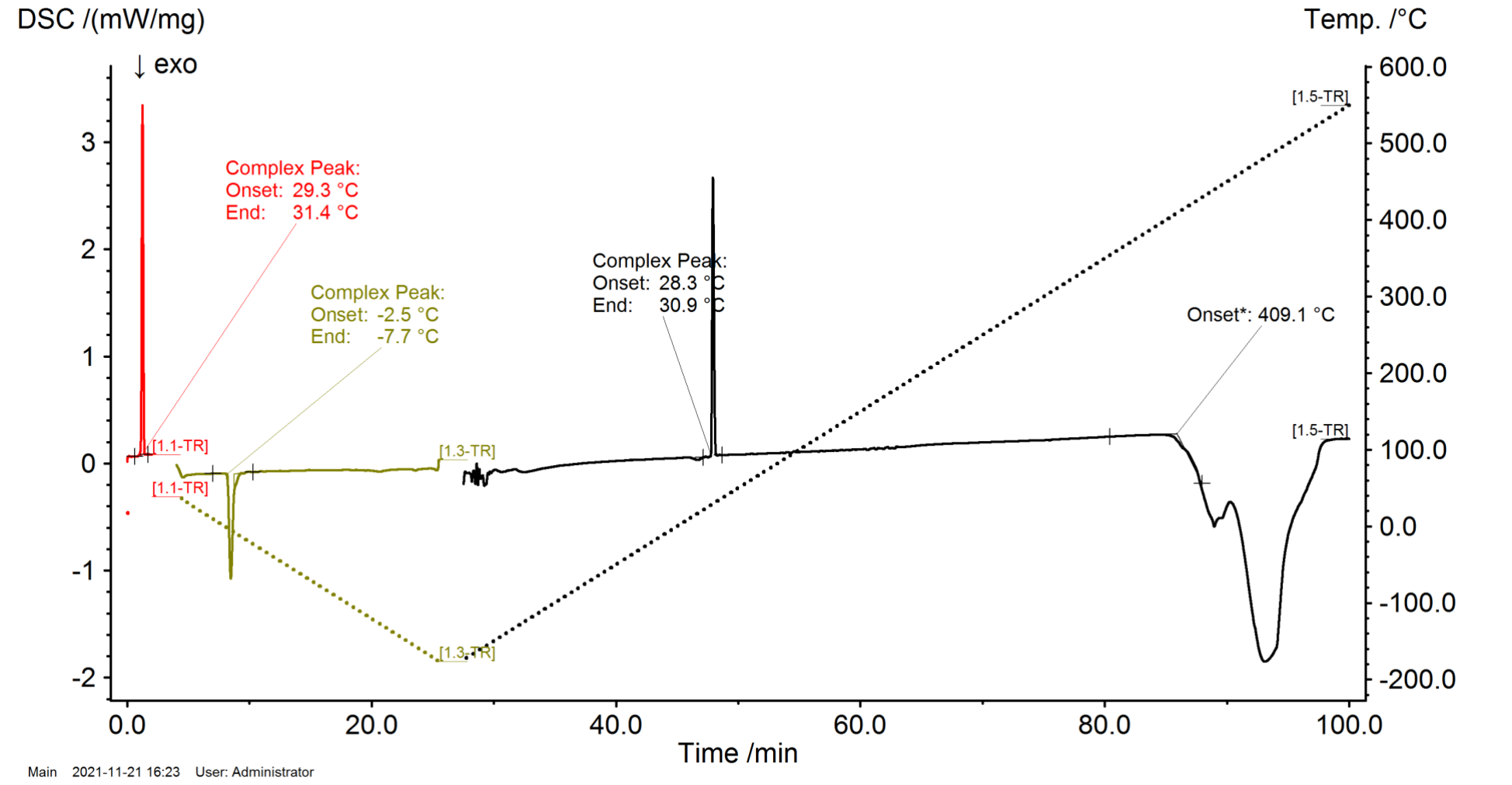

Figure S56: DSC curve of [BMIm]**6cPFSI** (10 K/min).

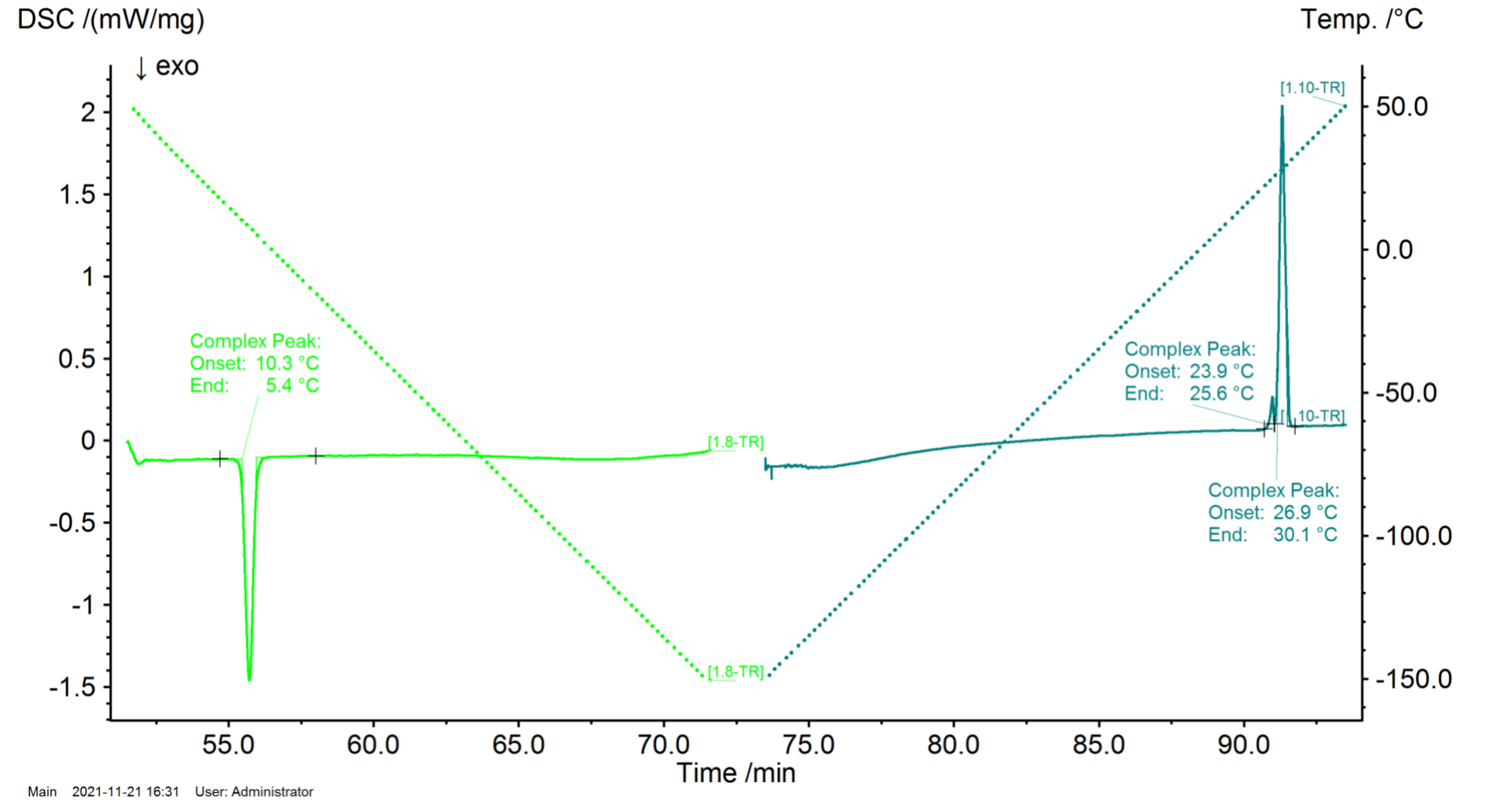

Figure S57: DSC curve of [BMPL]**4cPFSI** (without decomposition; 10 K/min).

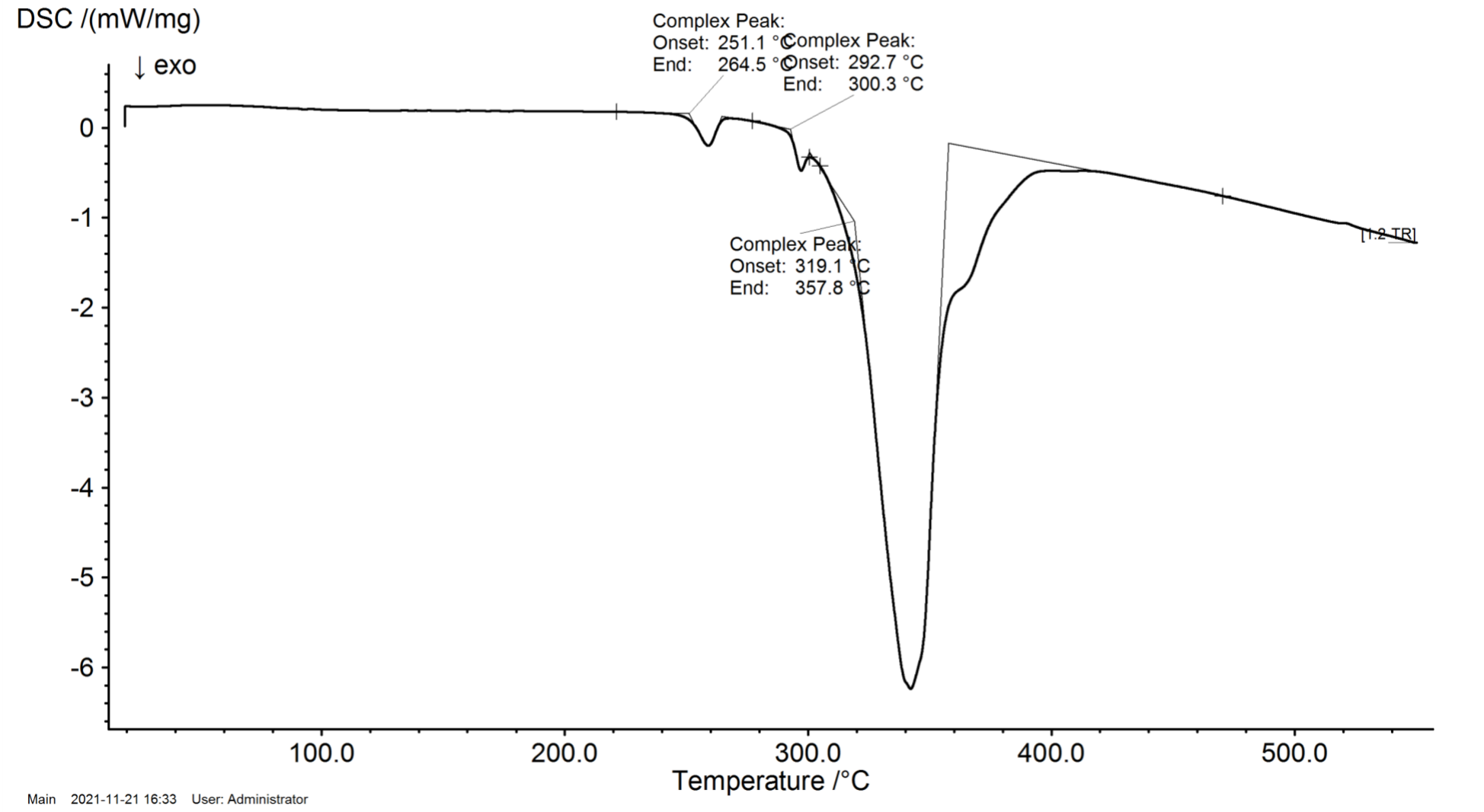

Figure S58: DSC curve of [BMPL]**4cPFSI** (only decomposition; 10 K/min).

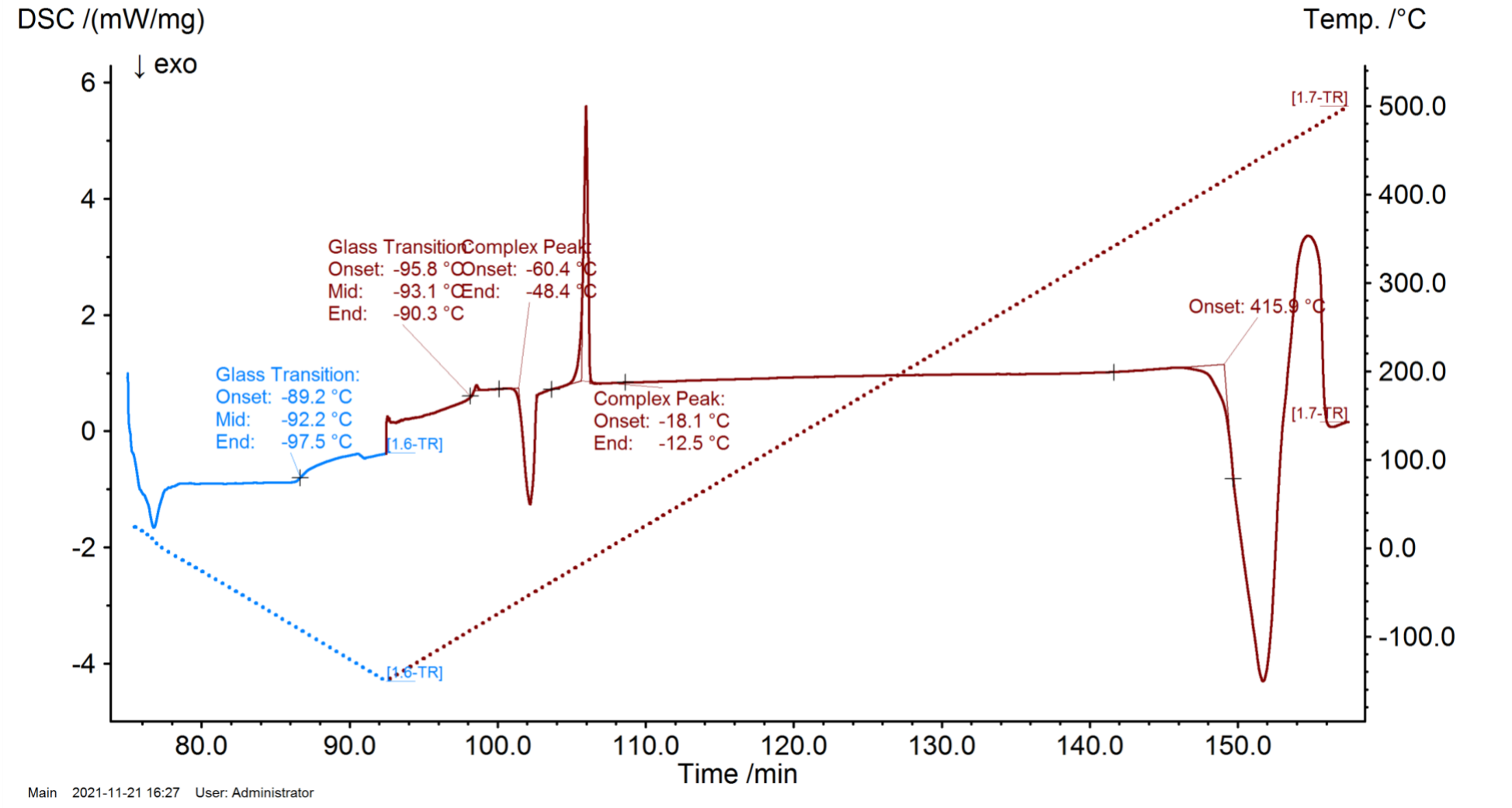

Figure S59: DSC curve of [BMPL]**5cPFSI** (10 K/min).

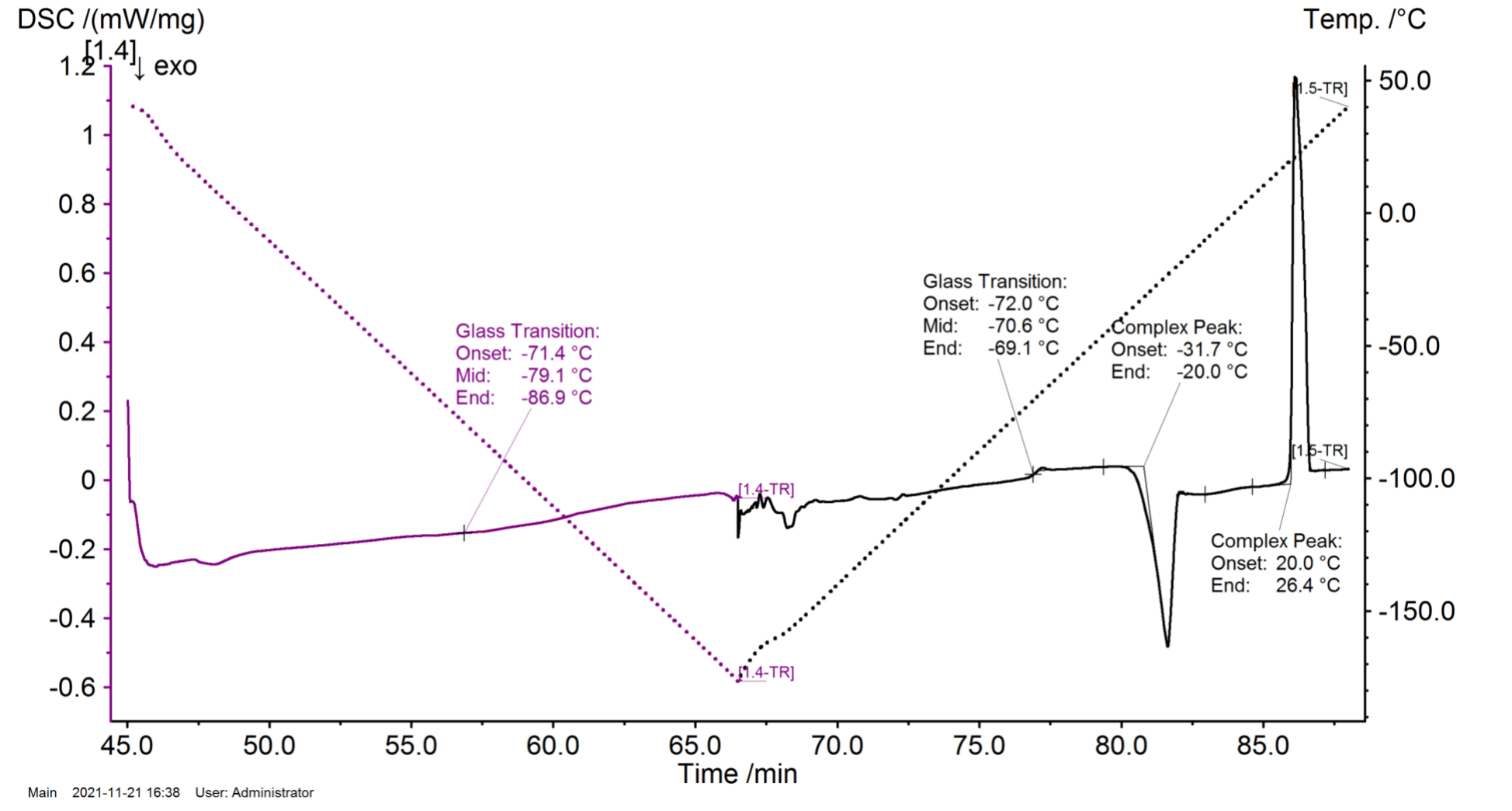

Figure S60: DSC curve of [BMPL]**6cPFSI** (without decomposition; 10 K/min).

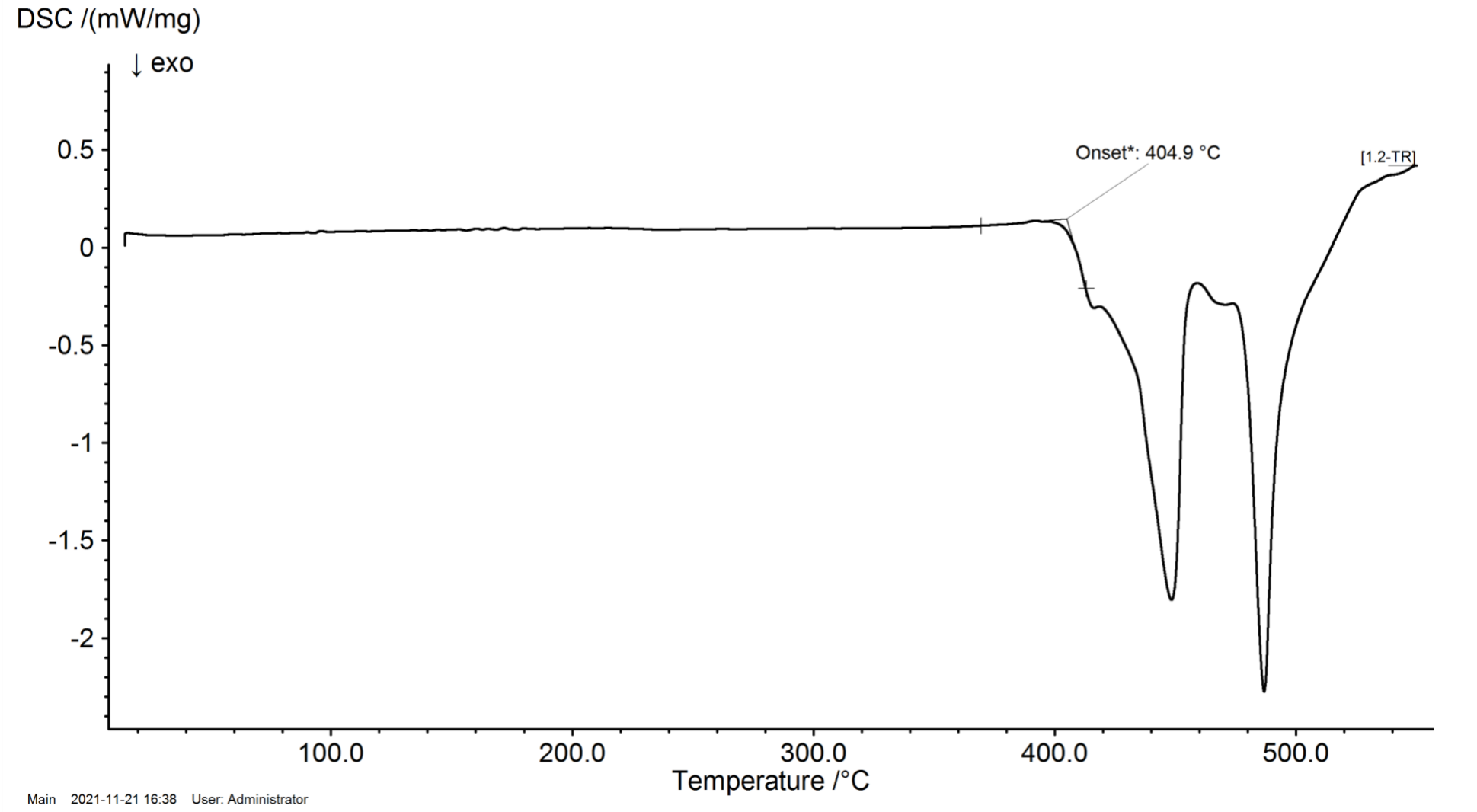

Figure S61: DSC curve of [BMPL]**6cPFSI** (only decomposition; 10 K/min).

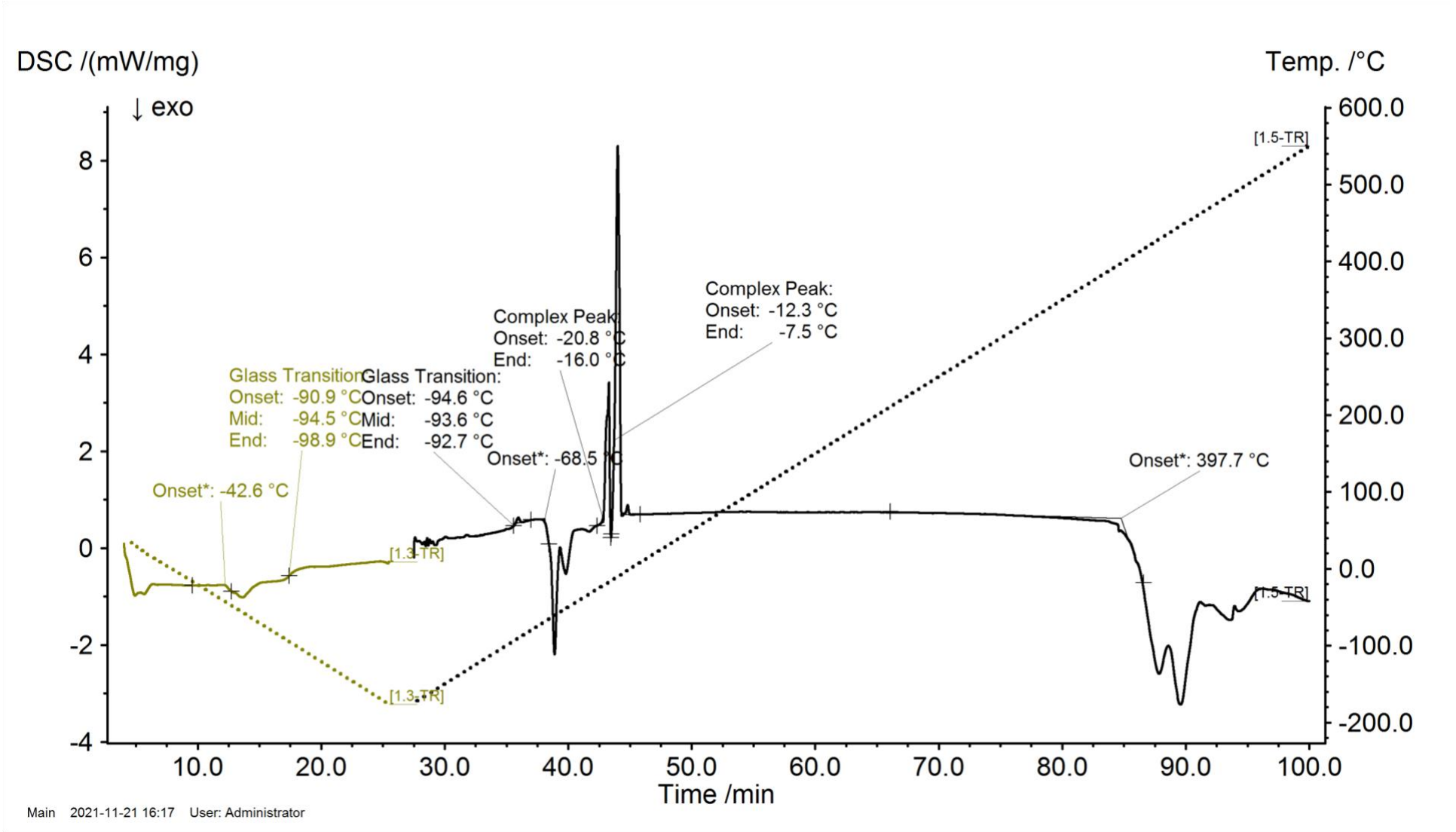

Figure S62: DSC curve of [EMIm]**TFSI** (10 K/min).

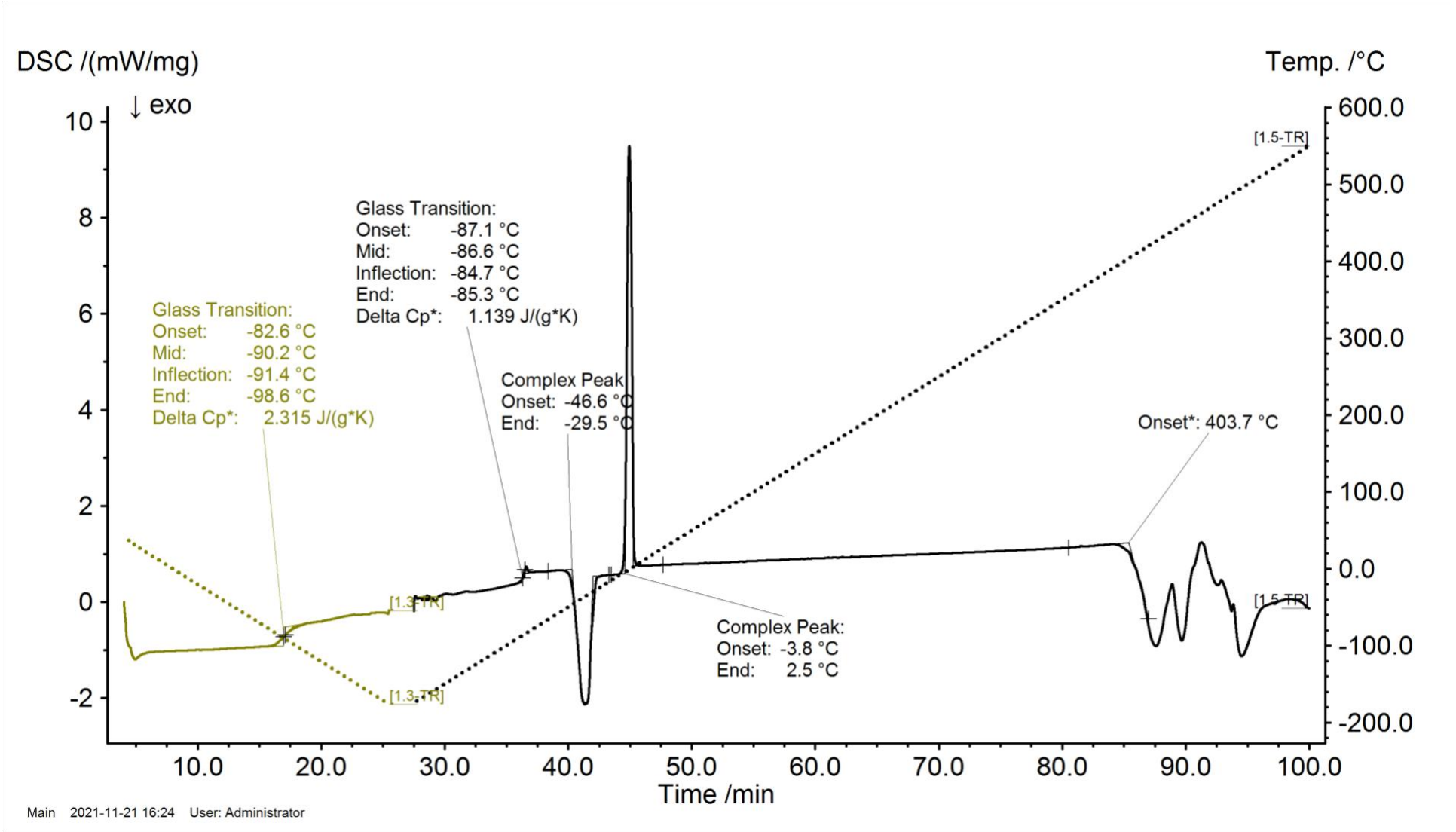

Figure S63: DSC curve of [BMIm]**TFSI** (10 K/min).

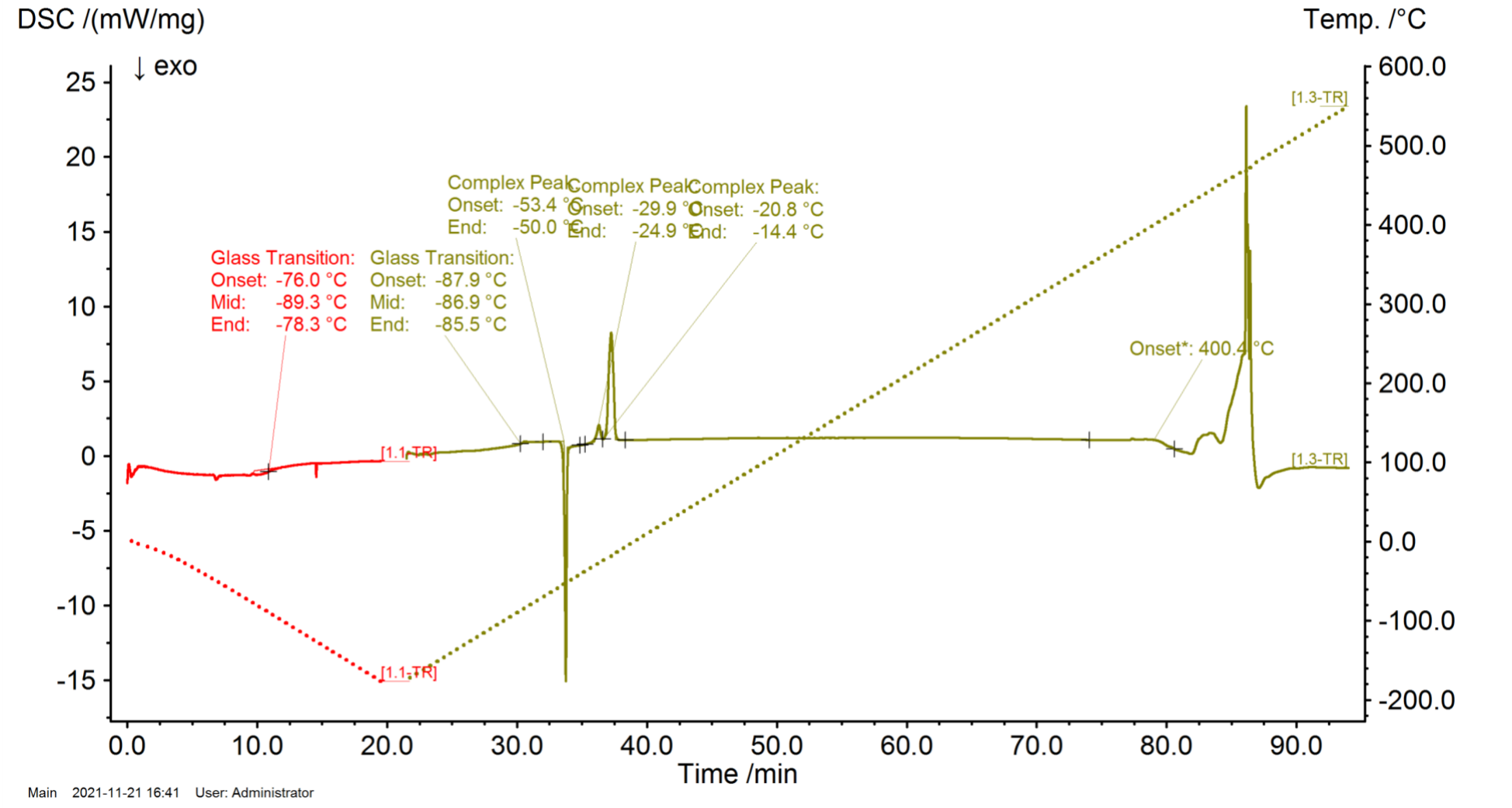

Figure S64: DSC curve of [BMPL]**TFSI** (10 K/min)

NMR Spectra

[EMIm]**4cPFSI**

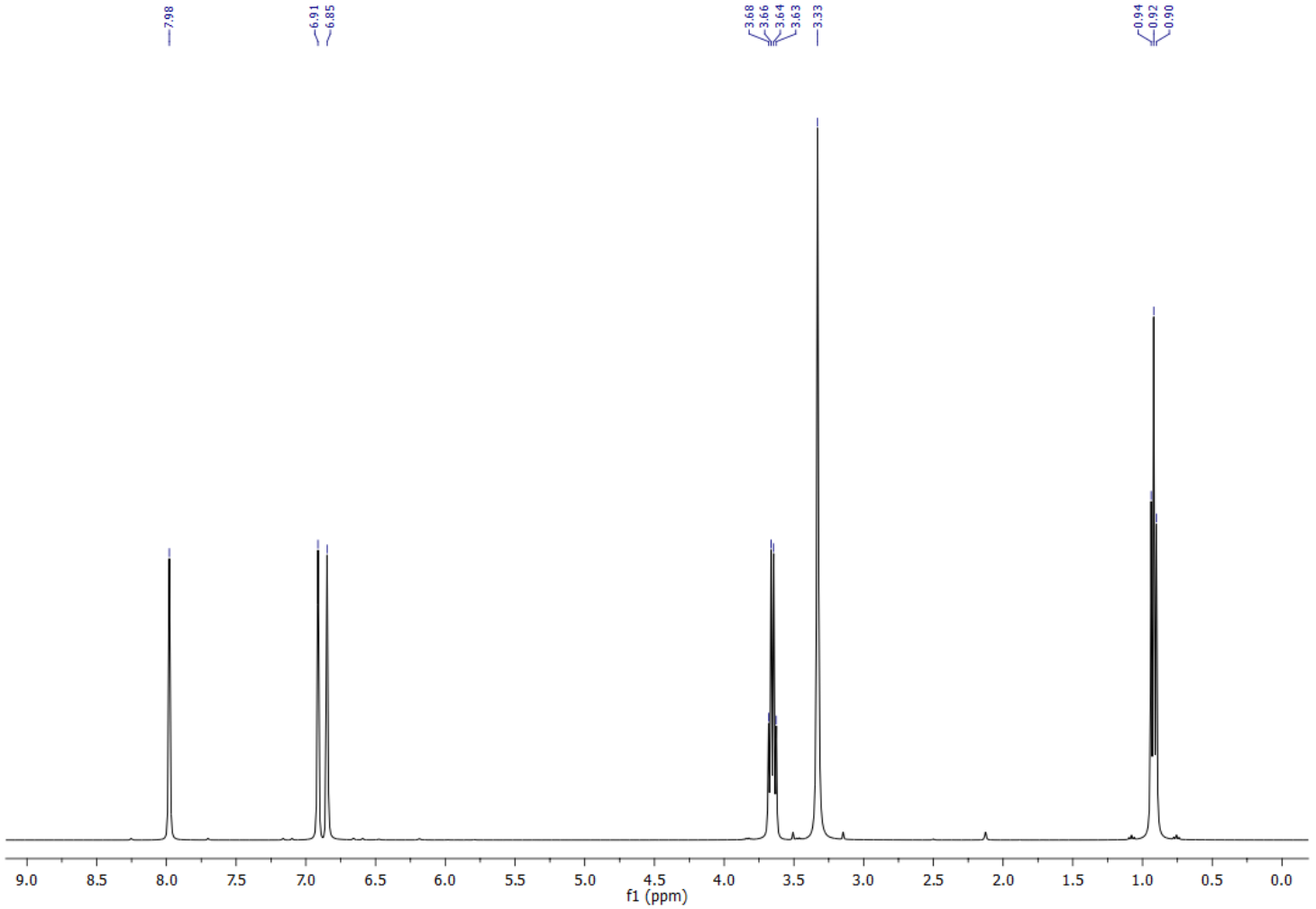

Figure S65: ^{1}H NMR spectrum of neat [EMIm]**4cPFSI** with DMSO-d6 capillary.

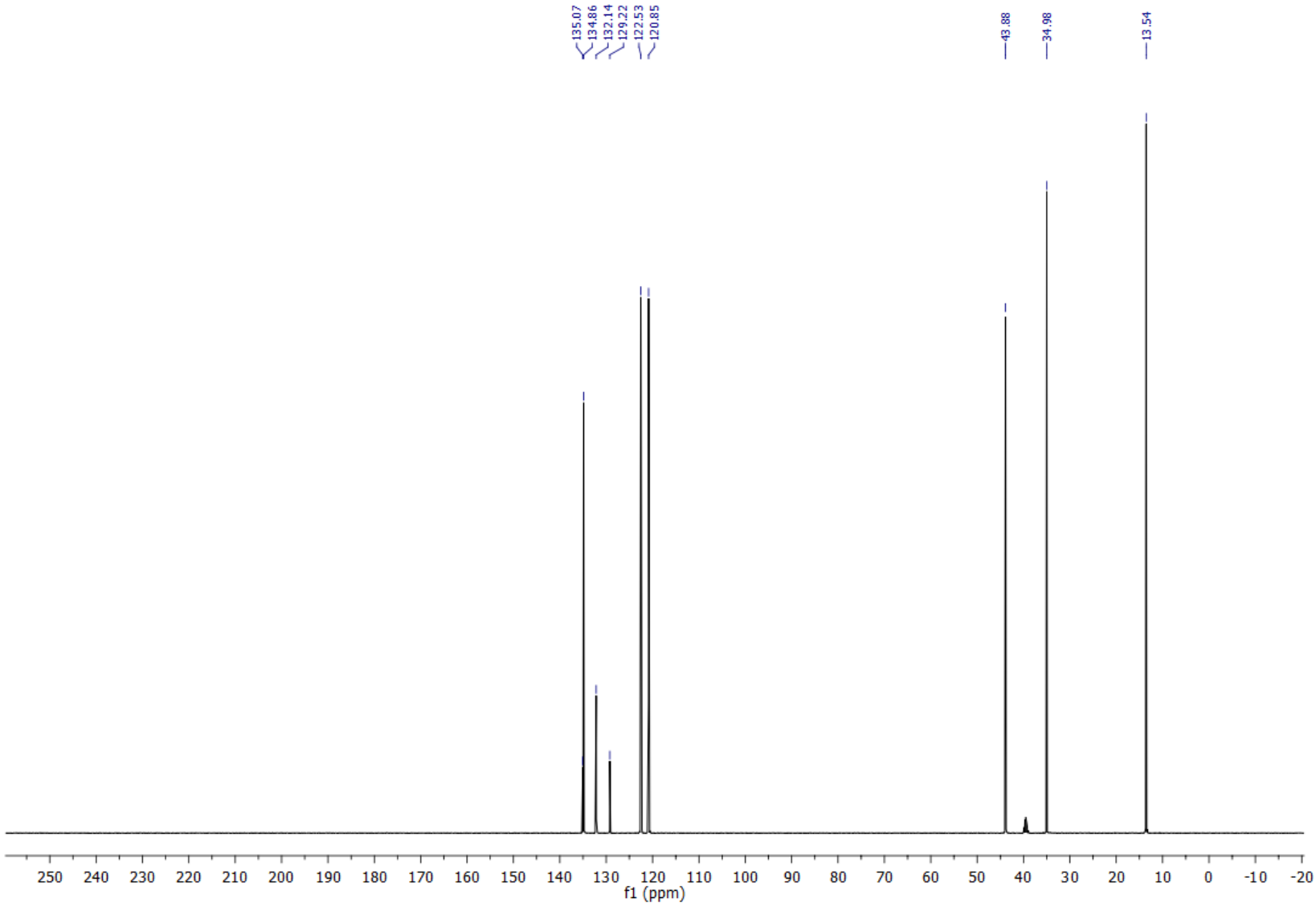

Figure S66: $^{13}C\{^{1}H\}$ NMR spectrum of neat [EMIm]**4cPFSI** with DMSO-d6 capillary.

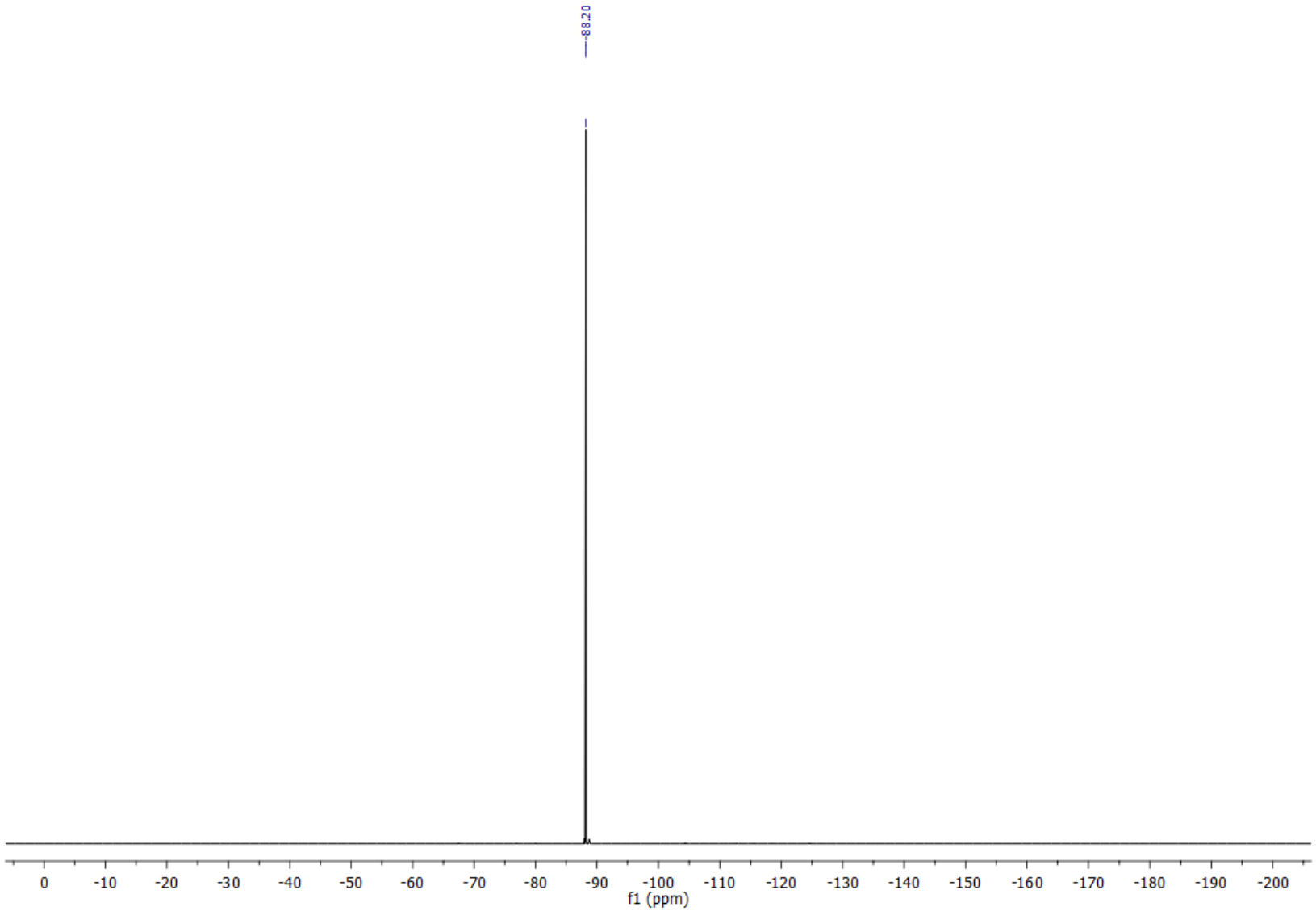

Figure S67: ^{19}F NMR spectrum of neat [EMIm]**4cPFSI** with DMSO-d6 capillary.

[EMIm]**5cPFSI**

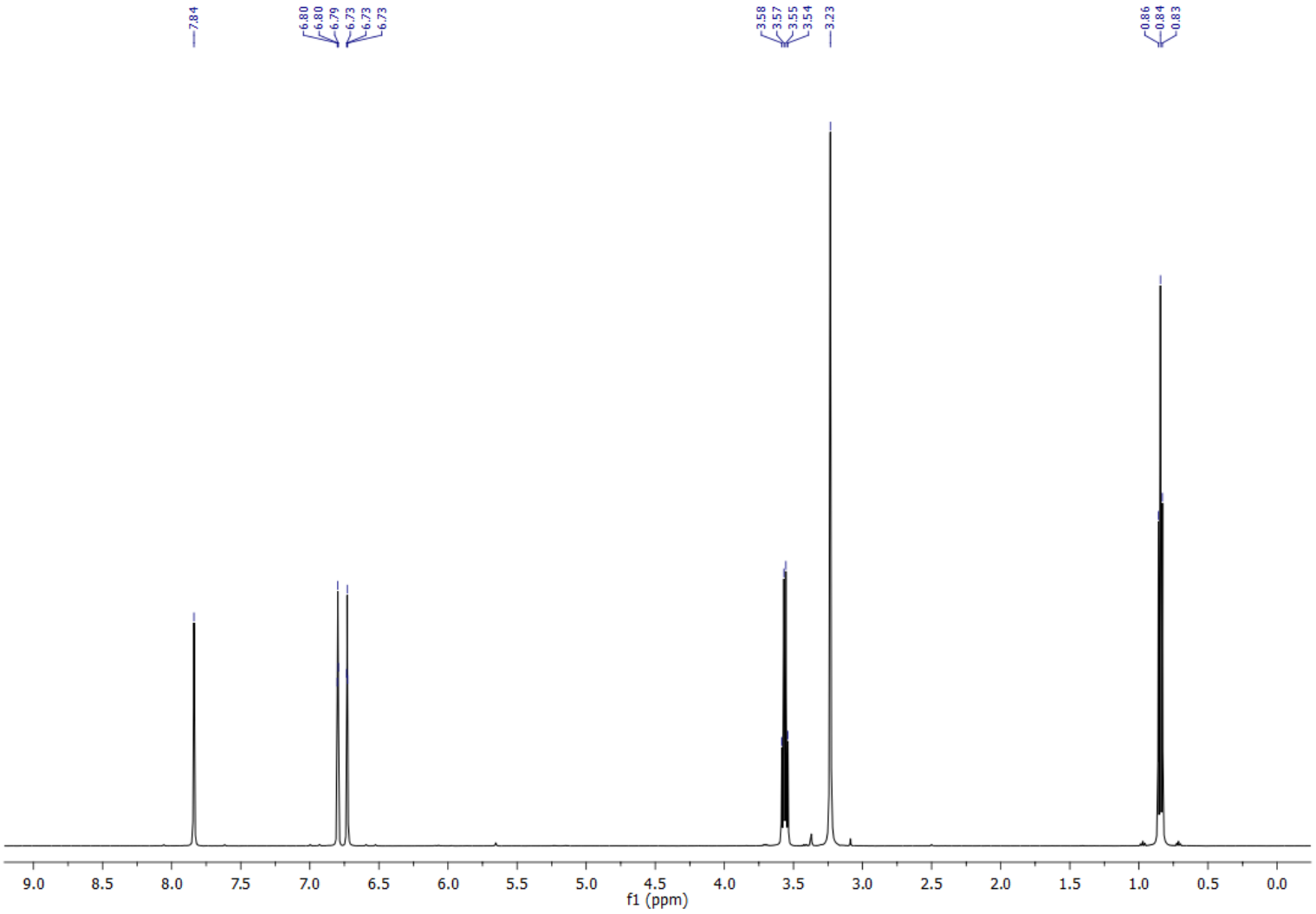

Figure S68: ^{1}H NMR spectrum of neat [EMIm]**5cPFSI** with DMSO-d6 capillary

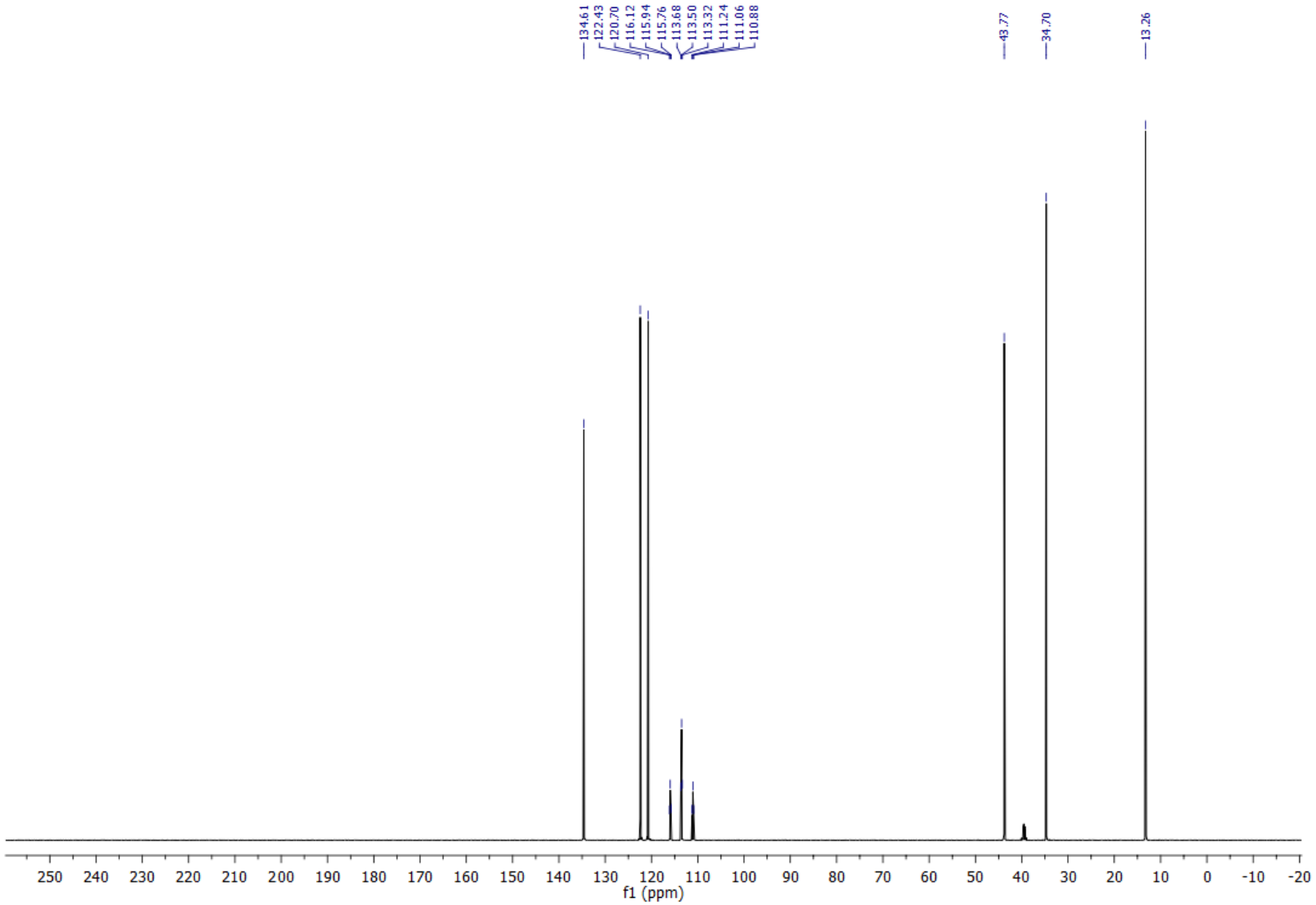

Figure S69: $^{13}C\{^{1}H\}$ NMR spectrum of neat [EMIm]**5cPFSI** with DMSO-d6 capillary.

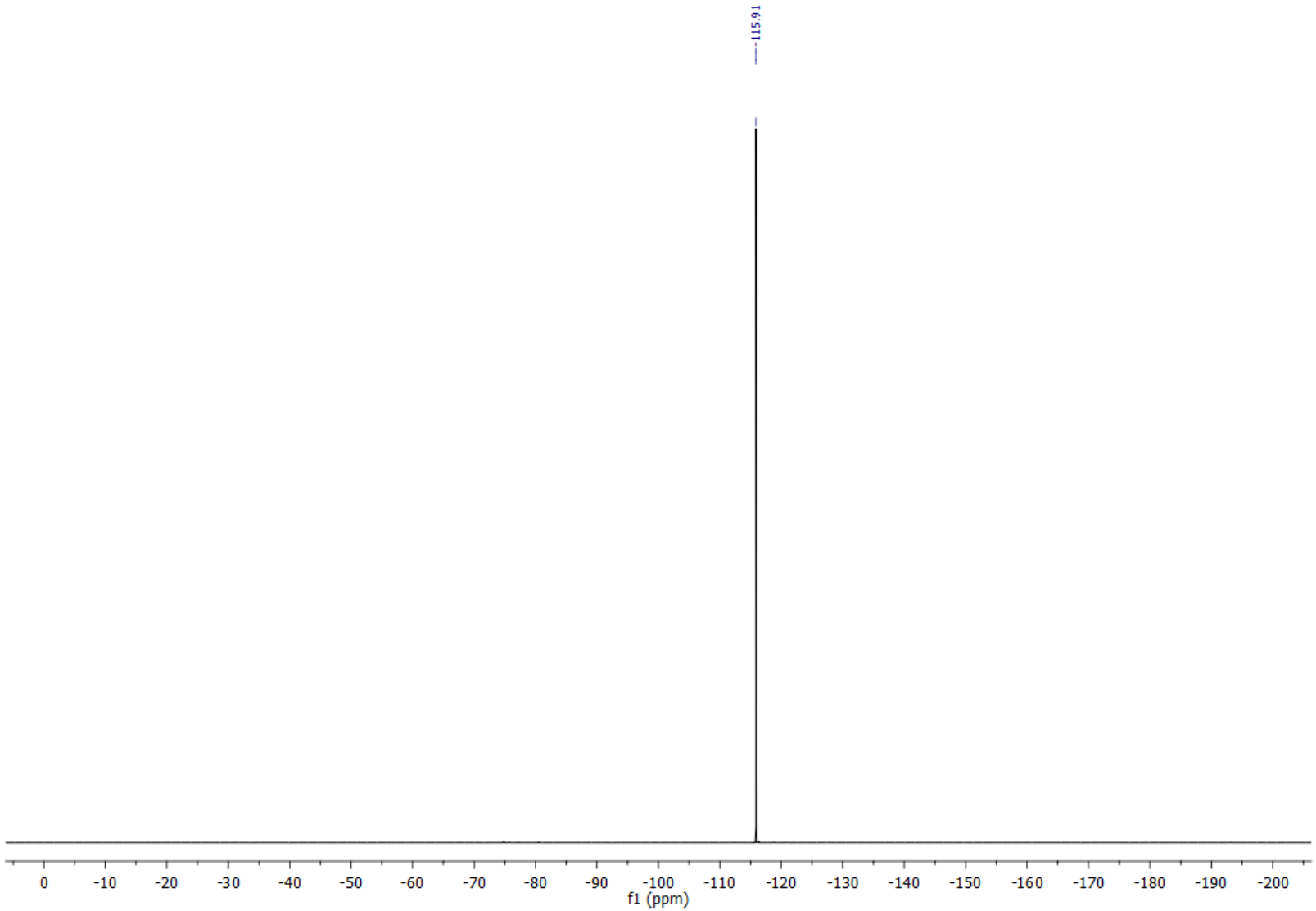

Figure S70: ^{19}F NMR spectrum of neat [EMIm]**5cPFSI** with DMSO-d6 capillary.

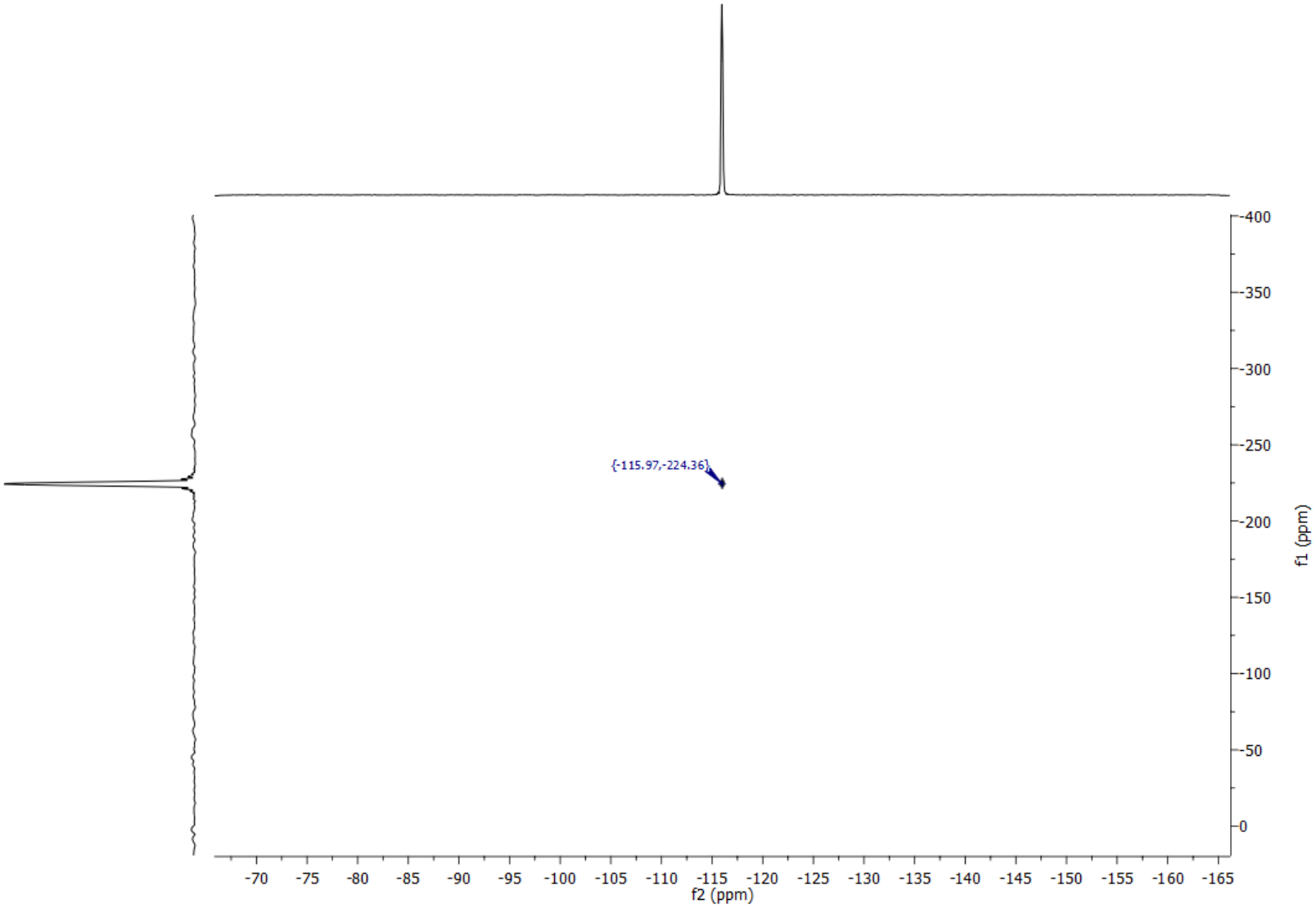

Figure S71: $^{19}F,^{15}N$ HMQC NMR spectrum of neat [EMIm]**5cPFSI** with DMSO-d6 capillary.

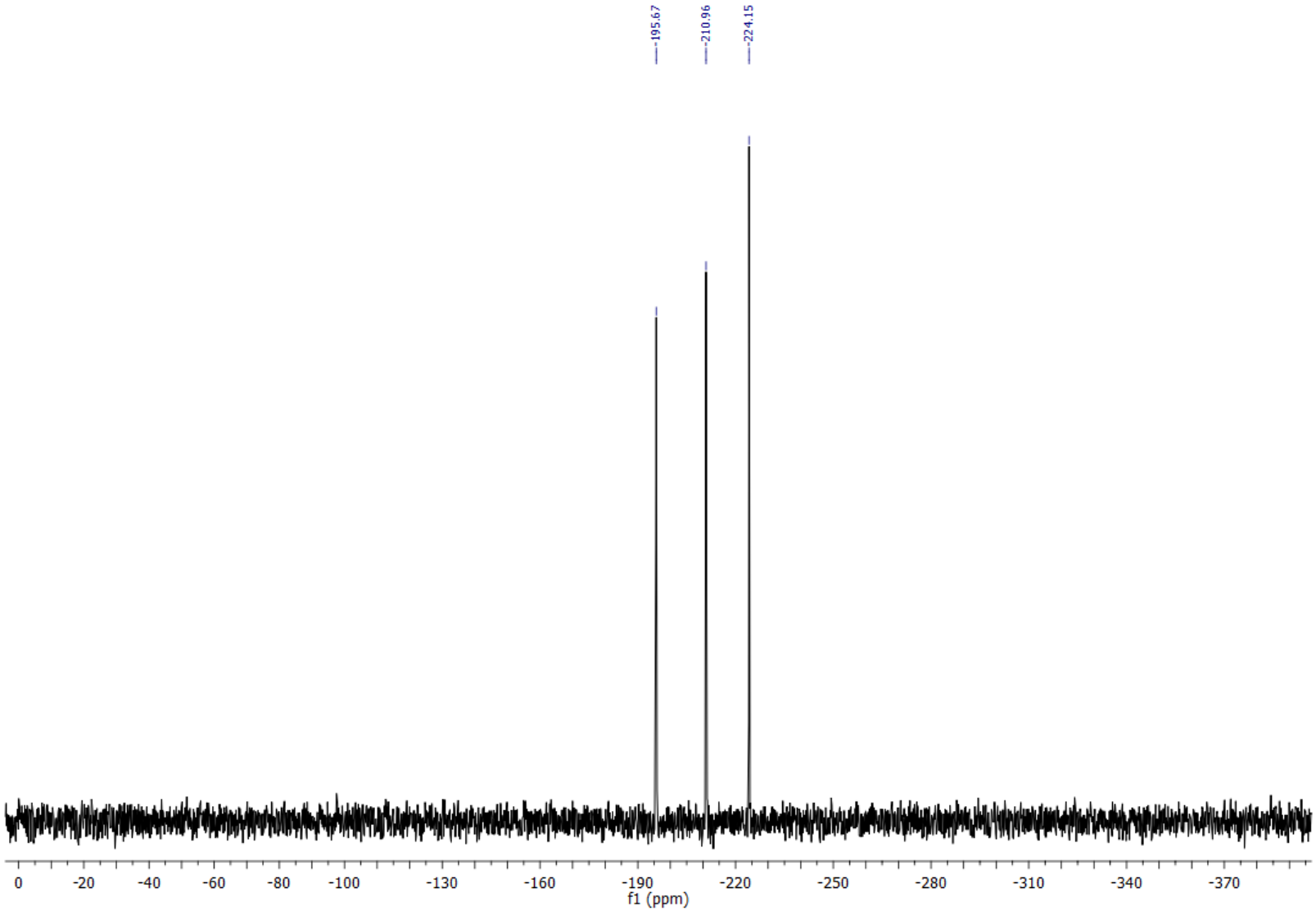

Figure S72: ^{15}N NMR spectrum of neat [EMIm]**5cPFSI** with DMSO-d6 capillary.

[EMIm]**6cPFSI**

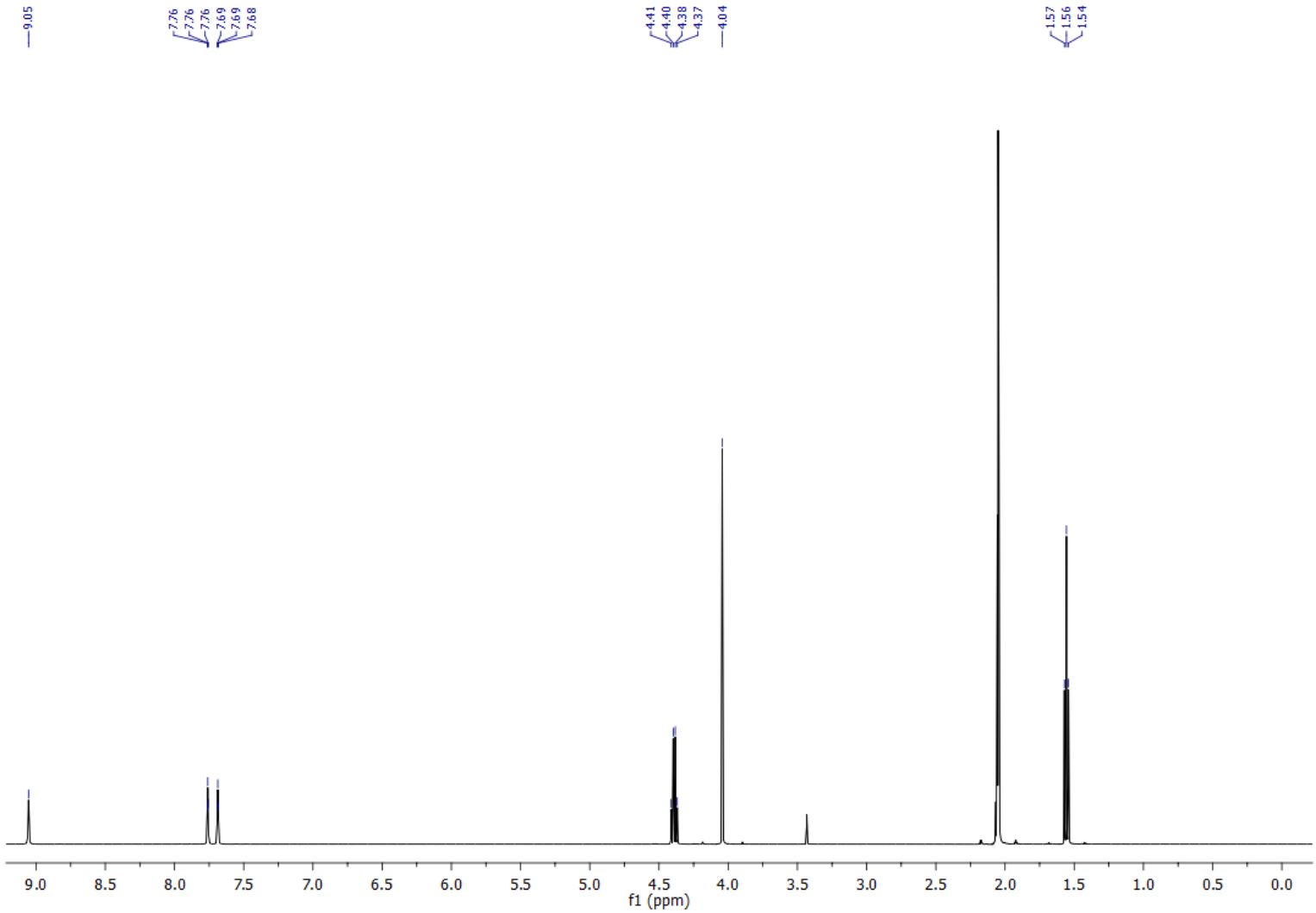

Figure S73: ^{1}H NMR spectrum of [EMIm]**6cPFSI** in acetone-d6.

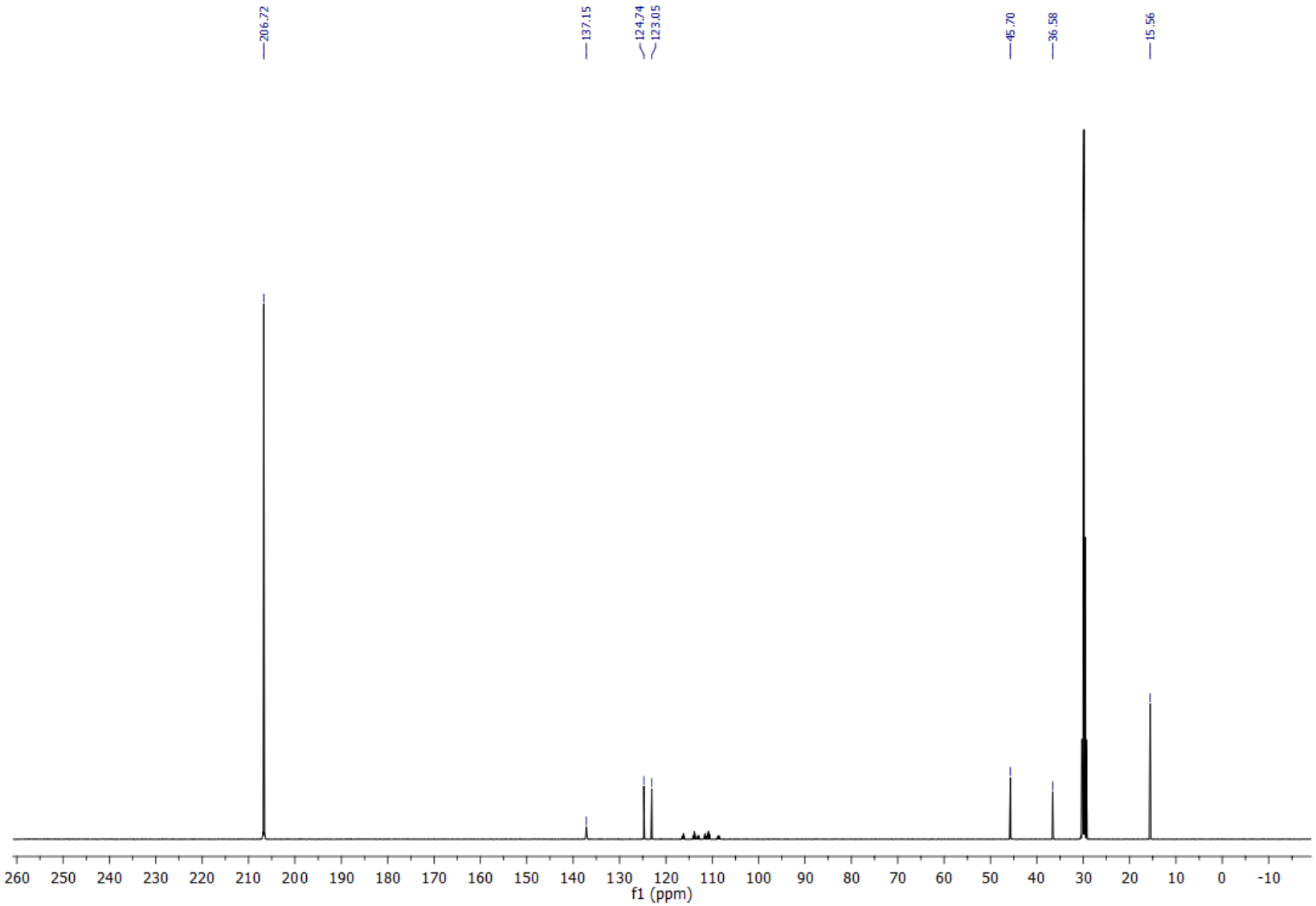

Figure S74: $^{13}C\{^{1}H\}$ NMR spectrum of [EMIm]**6cPFSI** in acetone-d6.

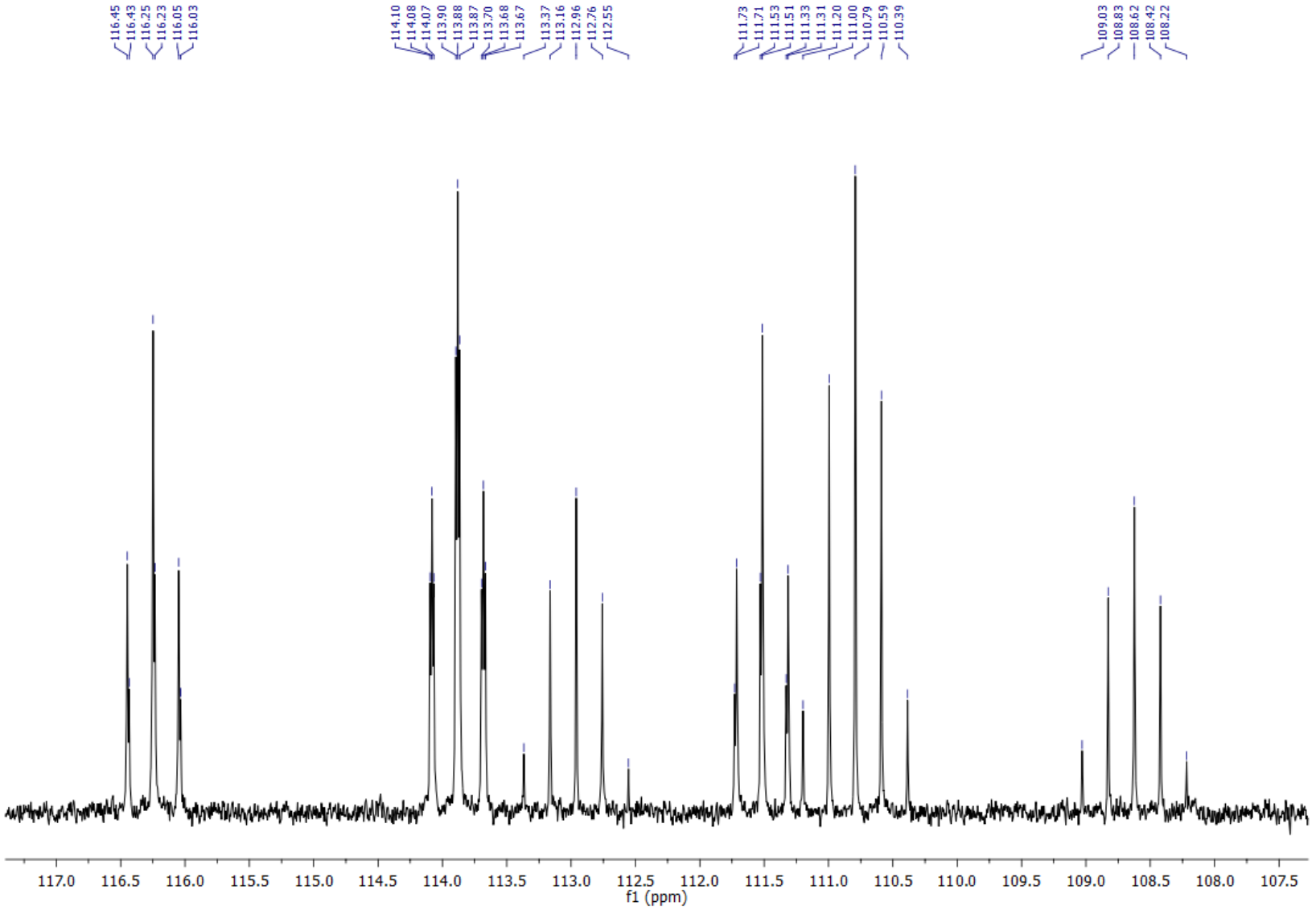

Figure S75: Excerpt of $^{13}C\{^{1}H\}$ NMR spectrum of [EMIm]**6cPFSI** in acetone-d6.

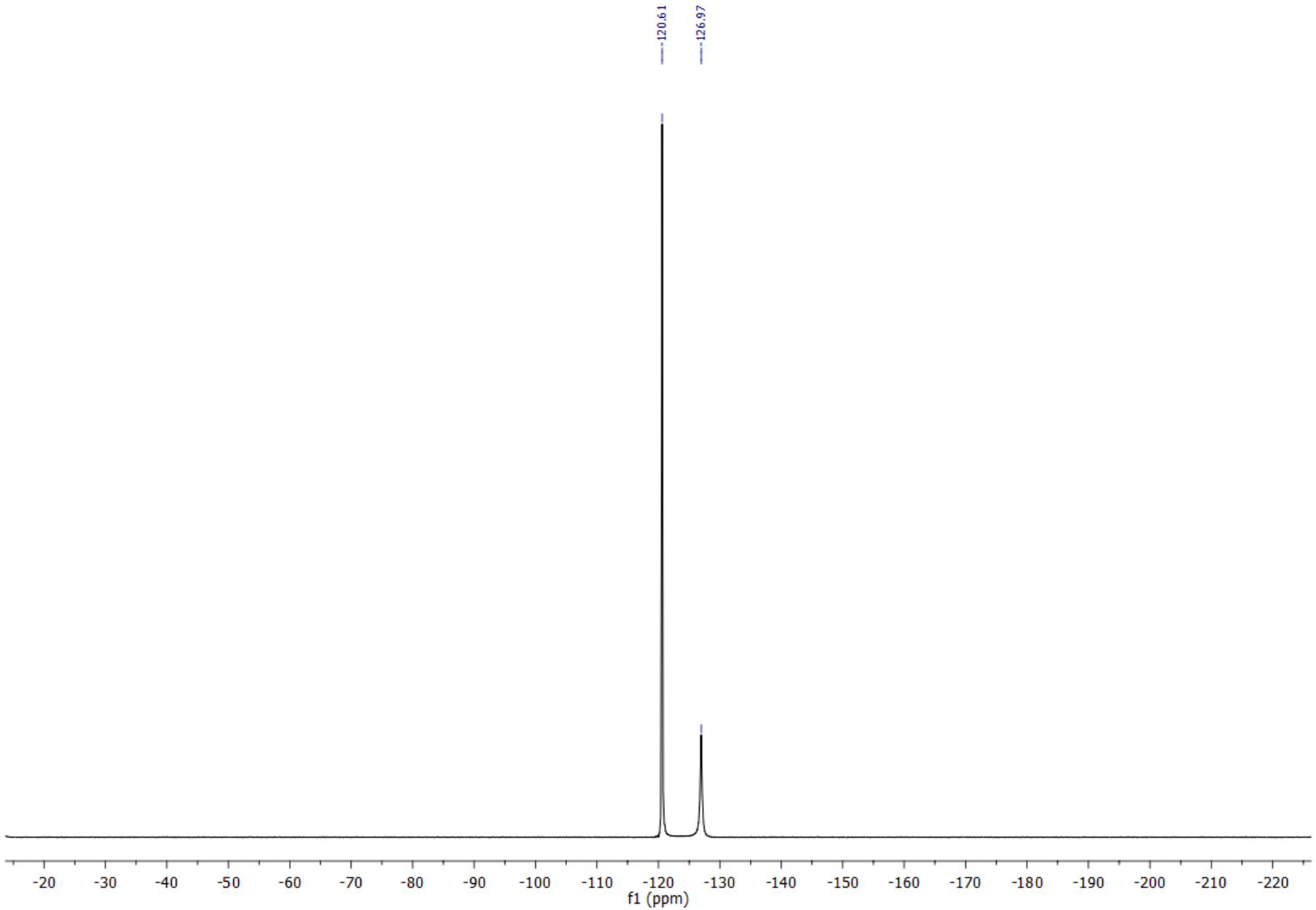

Figure S76: ^{19}F NMR spectrum of [EMIm]**6cPFSI** in acetone-d6.

[BMIm]**4cPFSI**

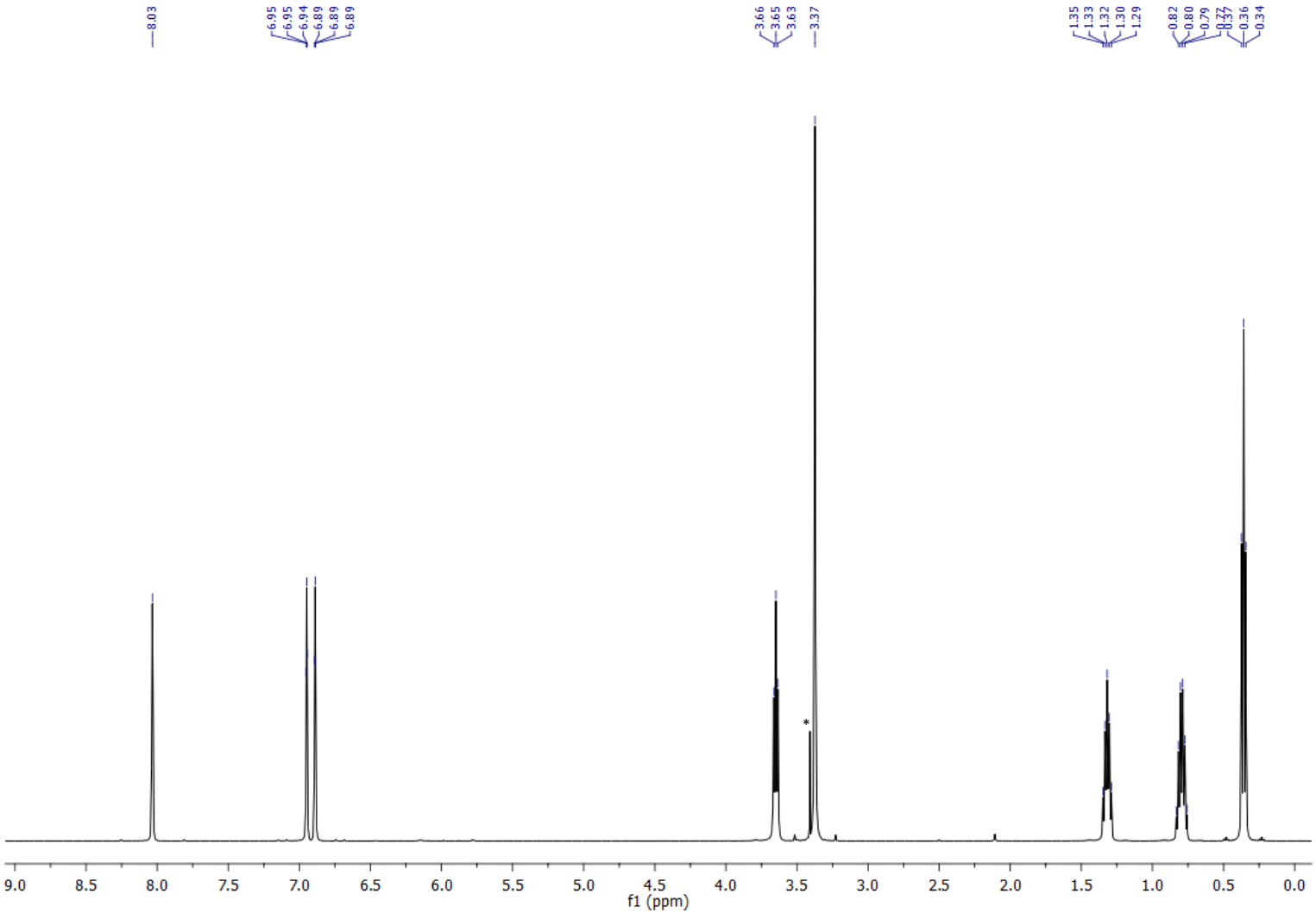

Figure S77: ^{1}H NMR spectrum of neat [BMIm]**4cPFSI** with DMSO-d6 capillary; *: residual water in DMSO-d6 capillary.

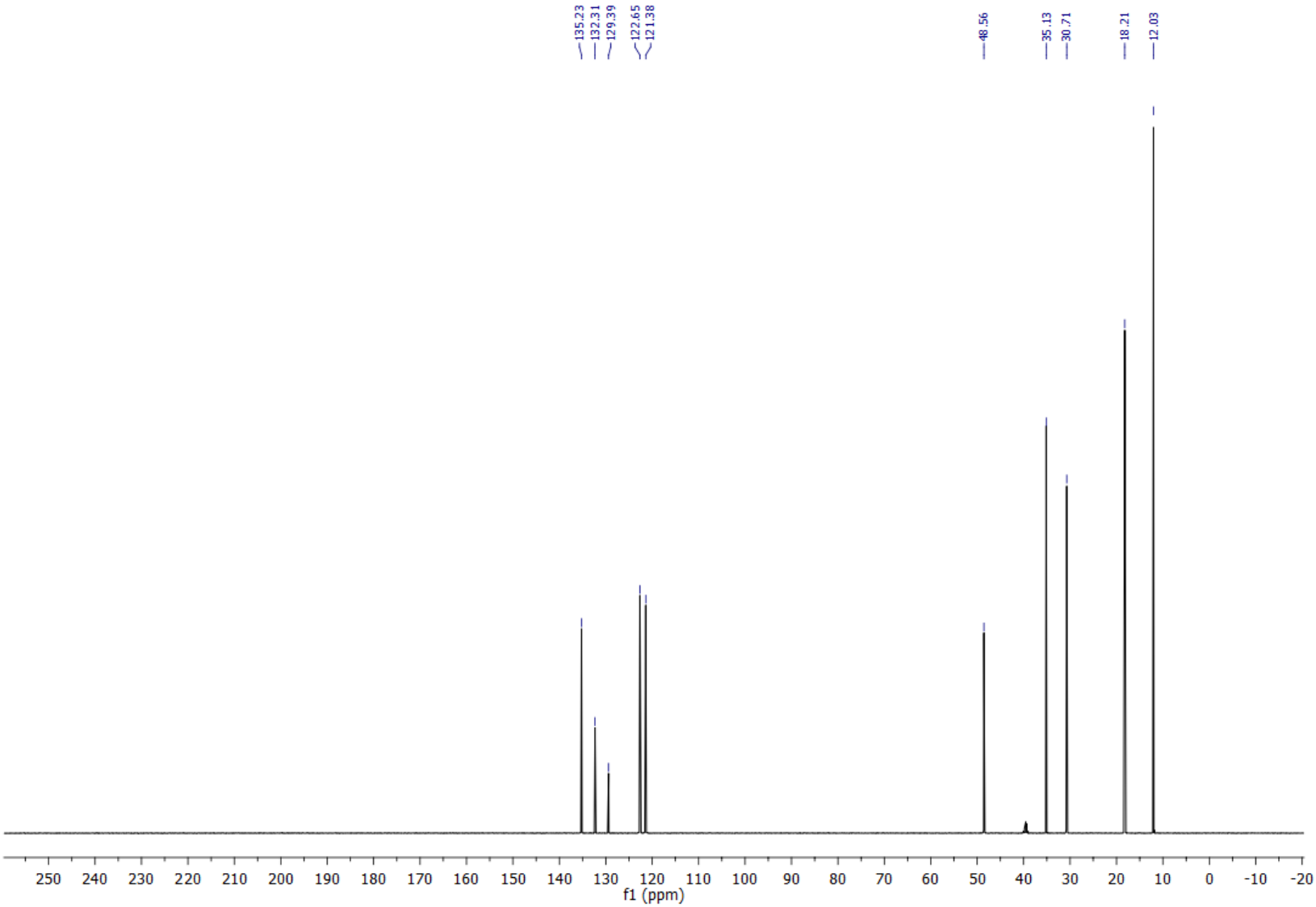

Figure S78: $^{13}C\{^{1}H\}$ NMR spectrum of neat [BMIm]**4cPFSI** with DMSO-d6 capillary.

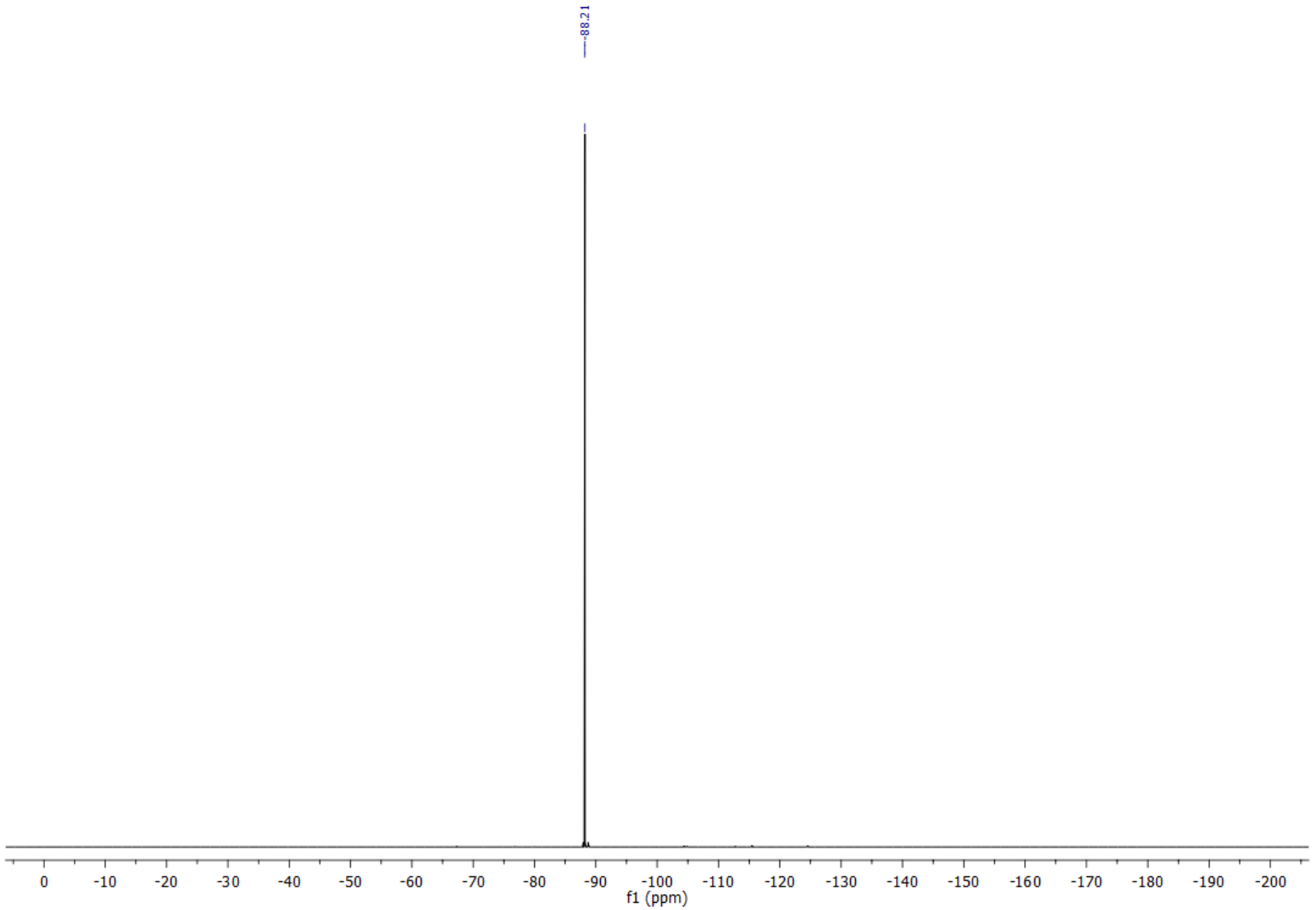

Figure S79: ^{19}F NMR spectrum of neat [BMIm]**4cPFSI** with DMSO-d6 capillary.

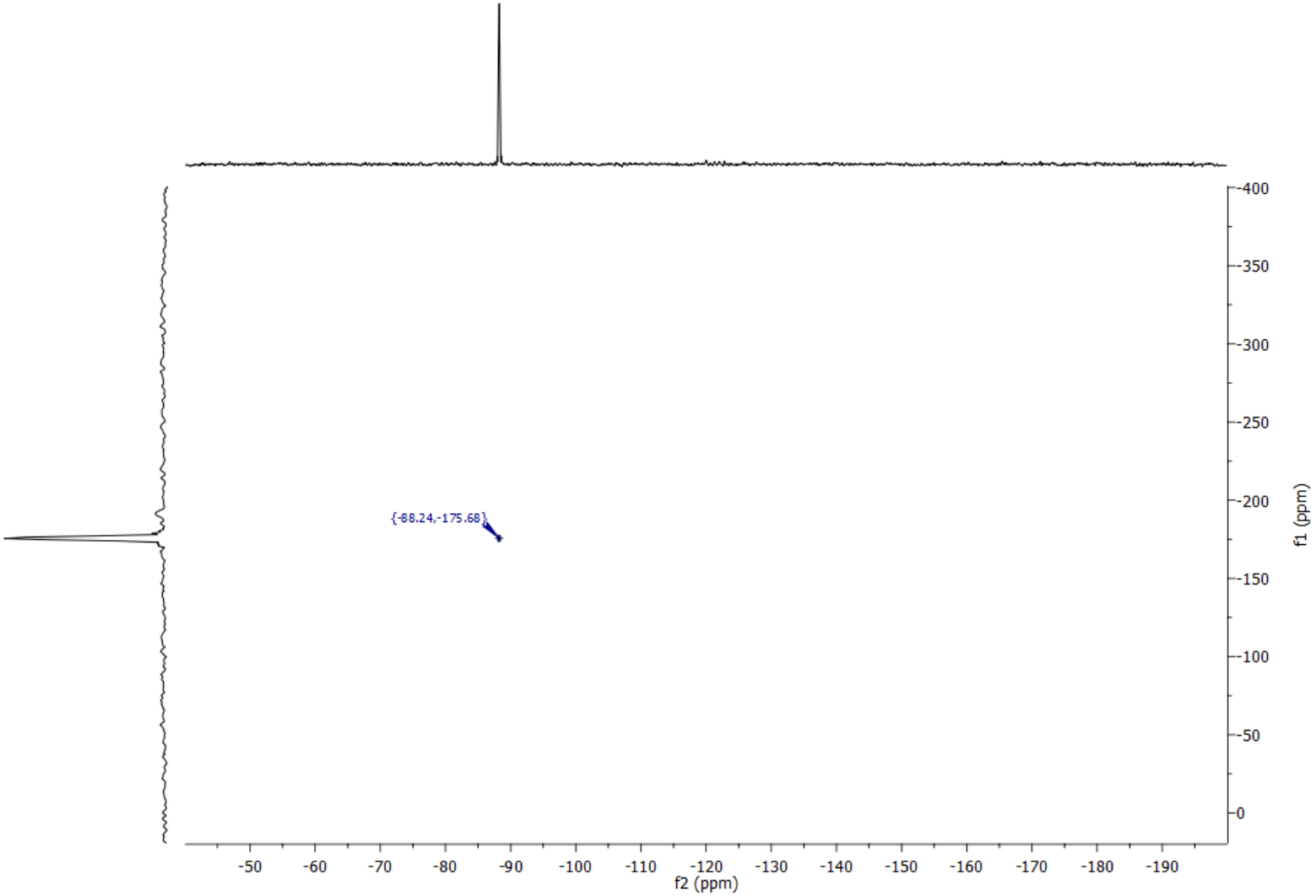

Figure S80: $^{19}F,^{15}N$ HMQC NMR spectrum of neat [BMIm]**4cPFSI** with DMSO-d6 capillary.

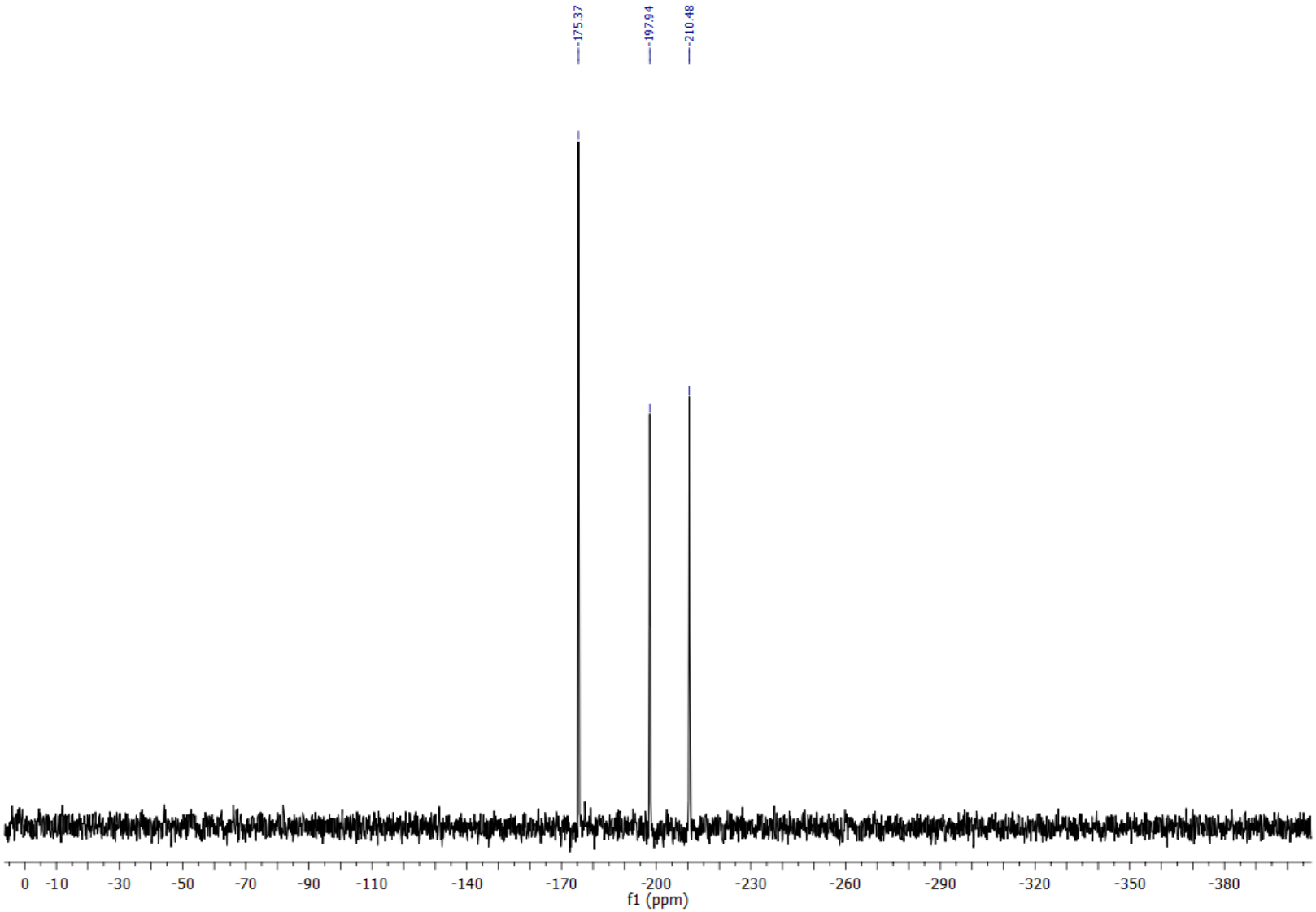

Figure S81: ^{15}N NMR spectrum of neat [BMIm]**4cPFSI** with DMSO-d6 capillary.

[BMIm]**5cPFSI**

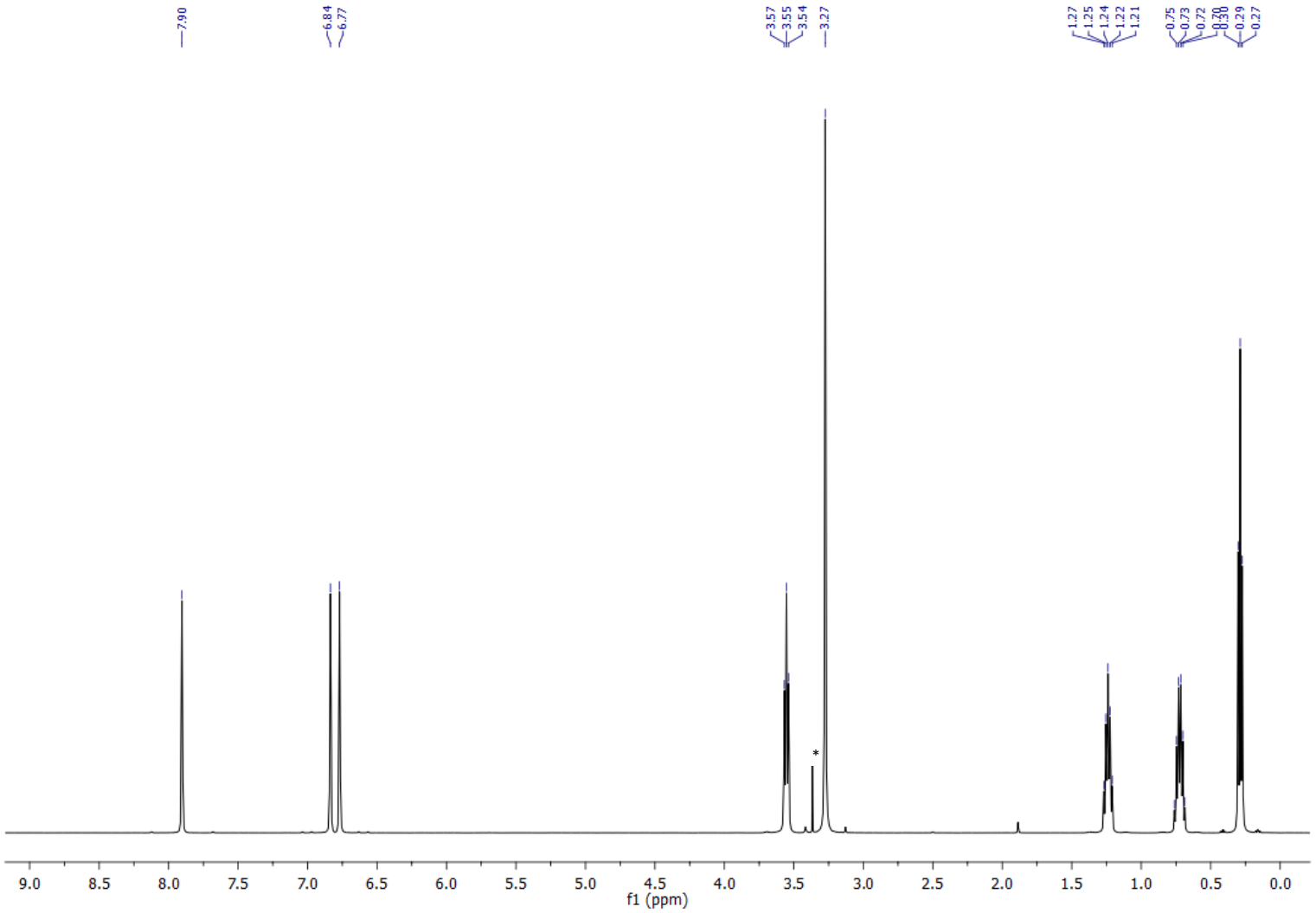

Figure S82: ^{1}H NMR spectrum of neat [BMIm]**5cPFSI** with DMSO-d6 capillary; *: residual water in DMSO-d6 capillary.

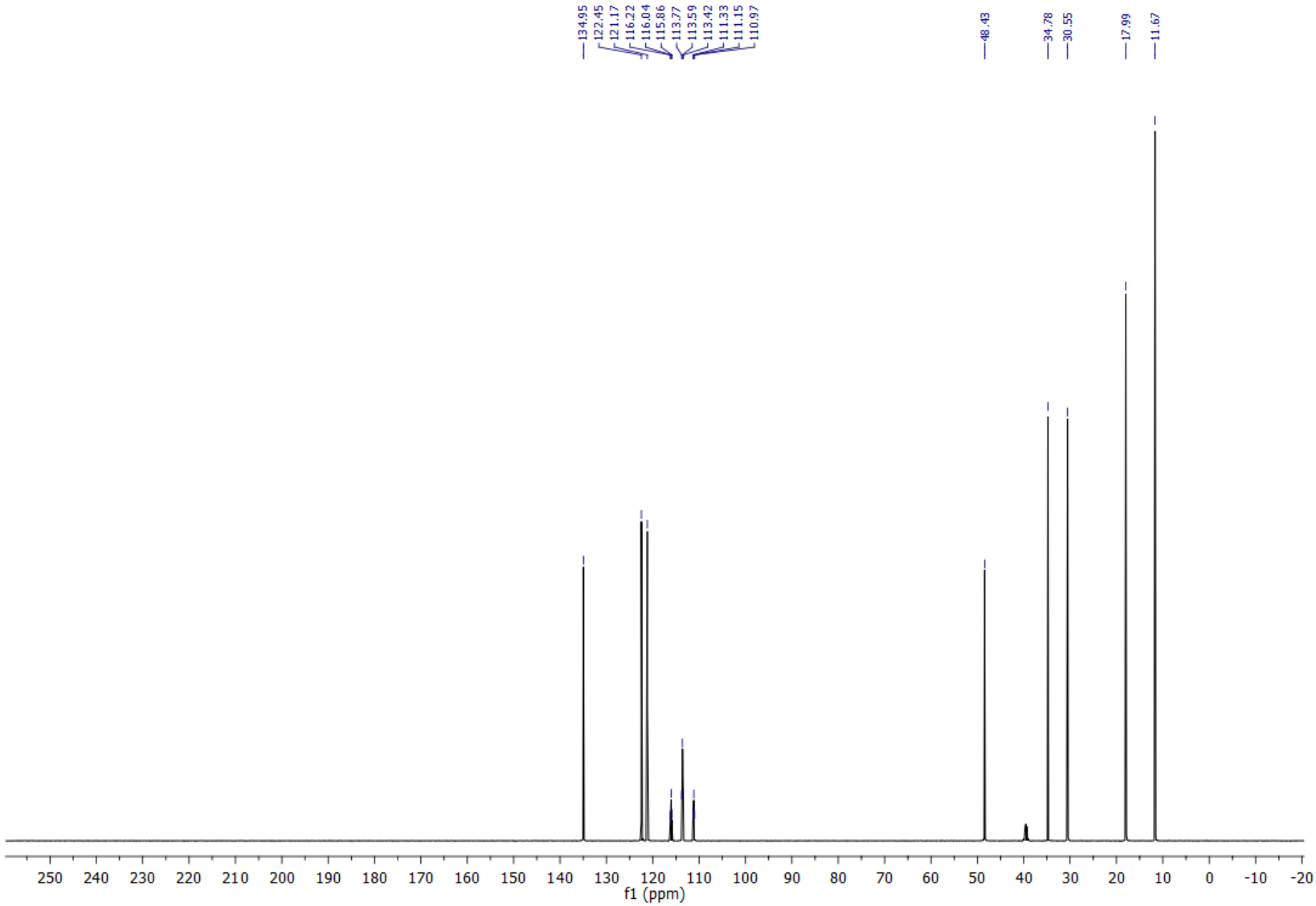

Figure S83: $^{13}C\{^{1}H\}$ NMR spectrum of neat [BMIm]**5cPFSI** with DMSO-d6 capillary.

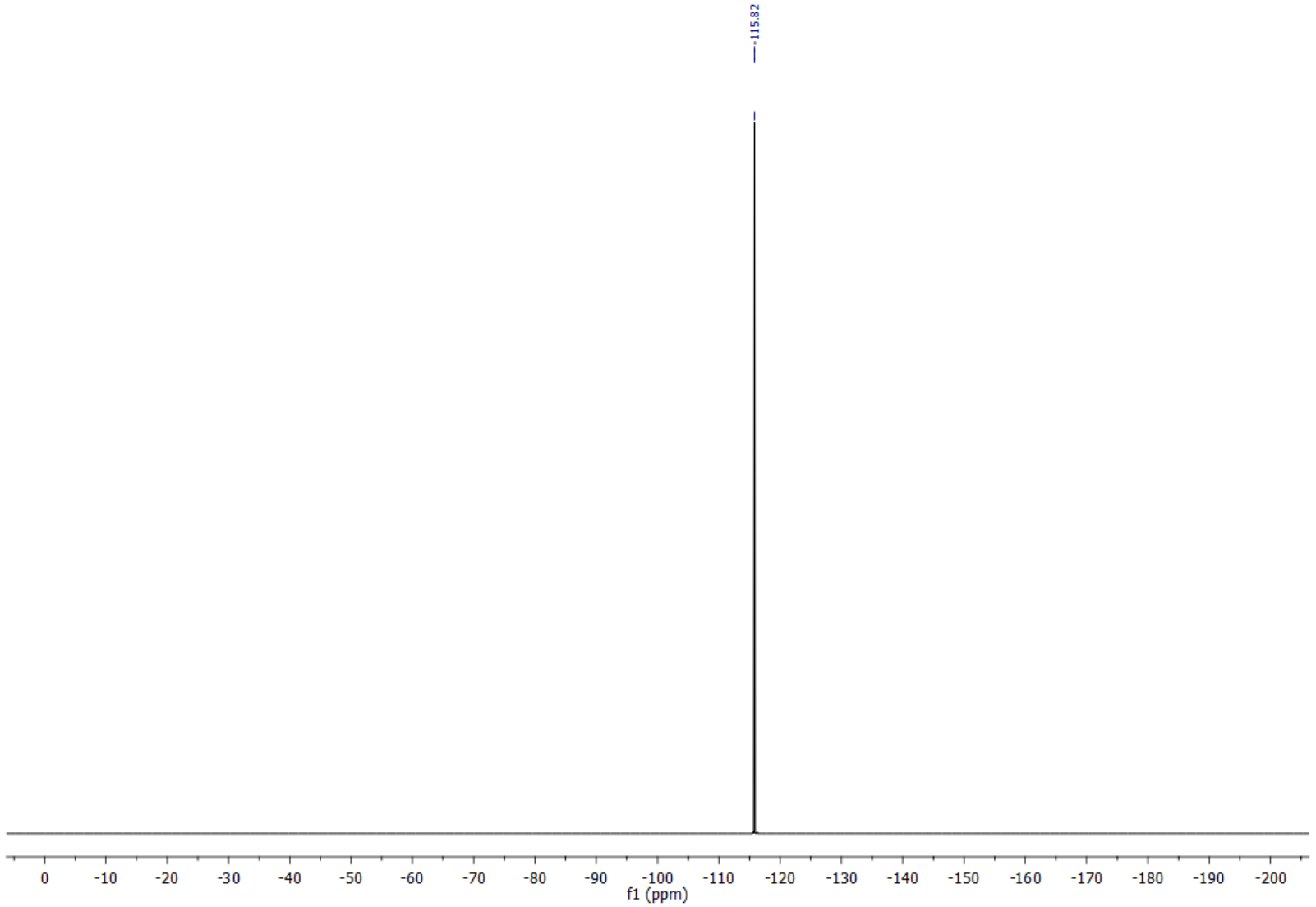

Figure S84: ^{19}F NMR spectrum of neat [BMIm]**5cPFSI** with DMSO-d6 capillary.

[BMIm]**6cPFSI**

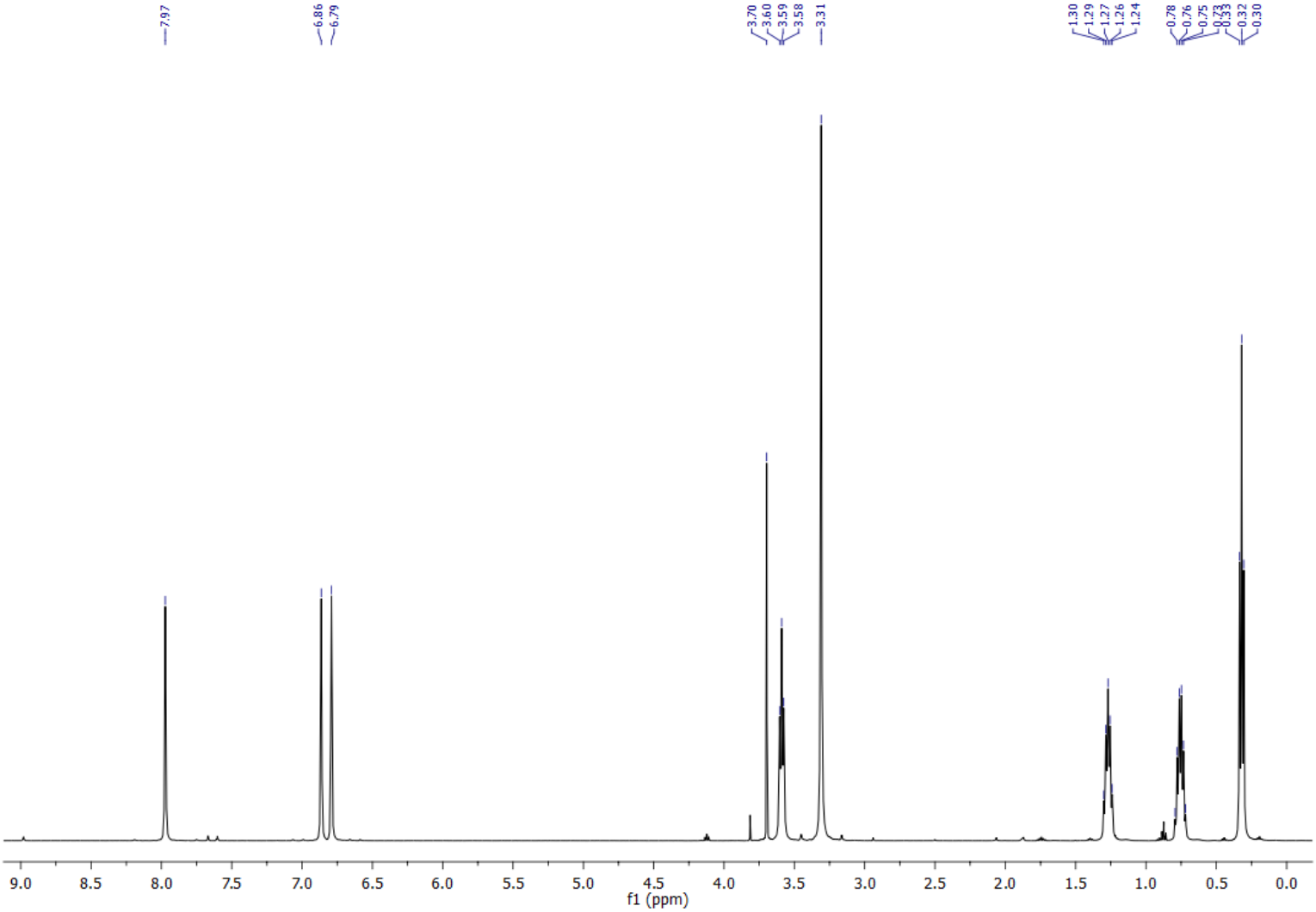

Figure S85: ^{1}H NMR spectrum of neat [BMIm]**6cPFSI** with DMSO-d6 capillary.

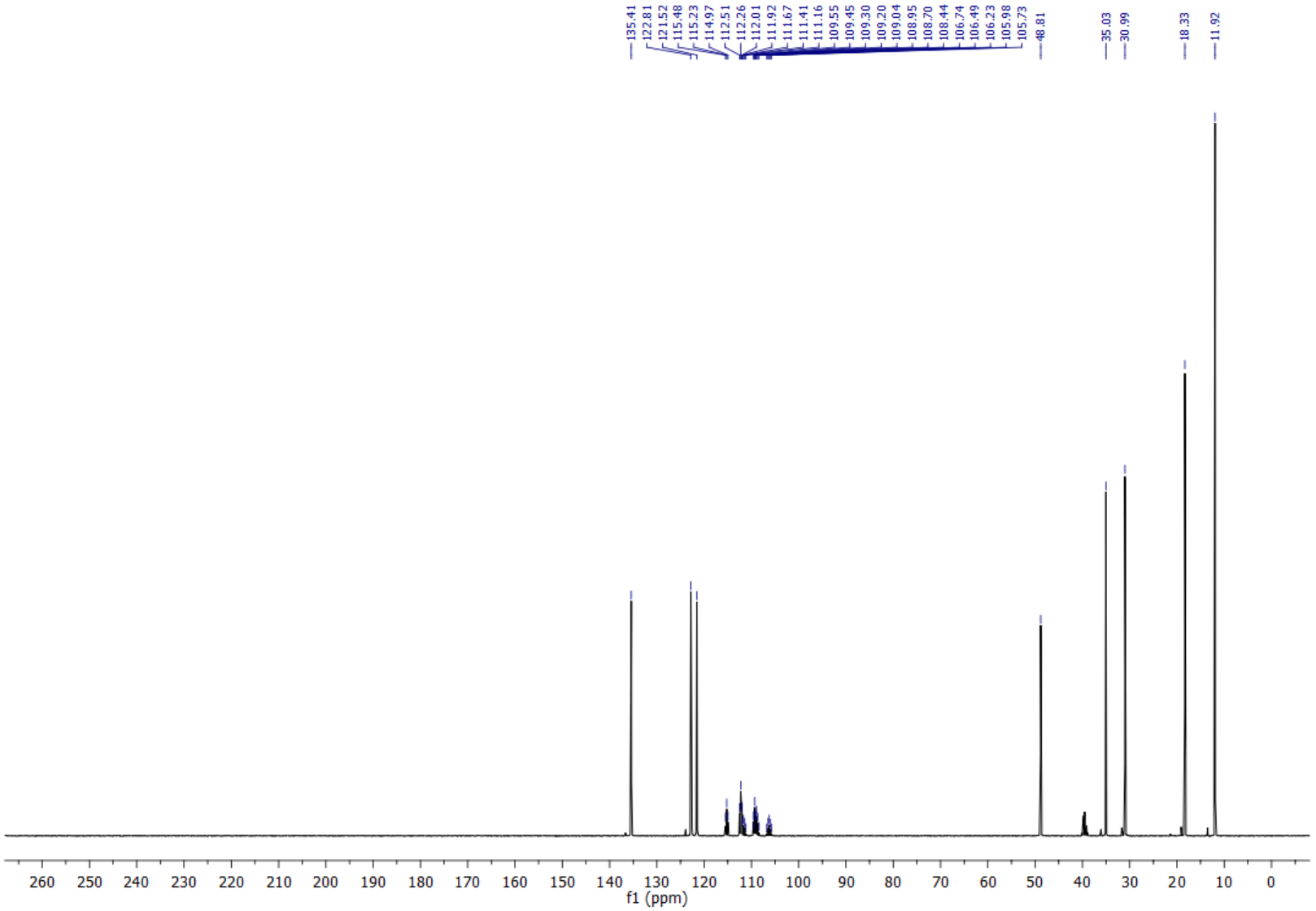

Figure S86: $^{13}C\{^{1}H\}$ NMR spectrum of neat [BMIm]**6cPFSI** with DMSO-d6 capillary.

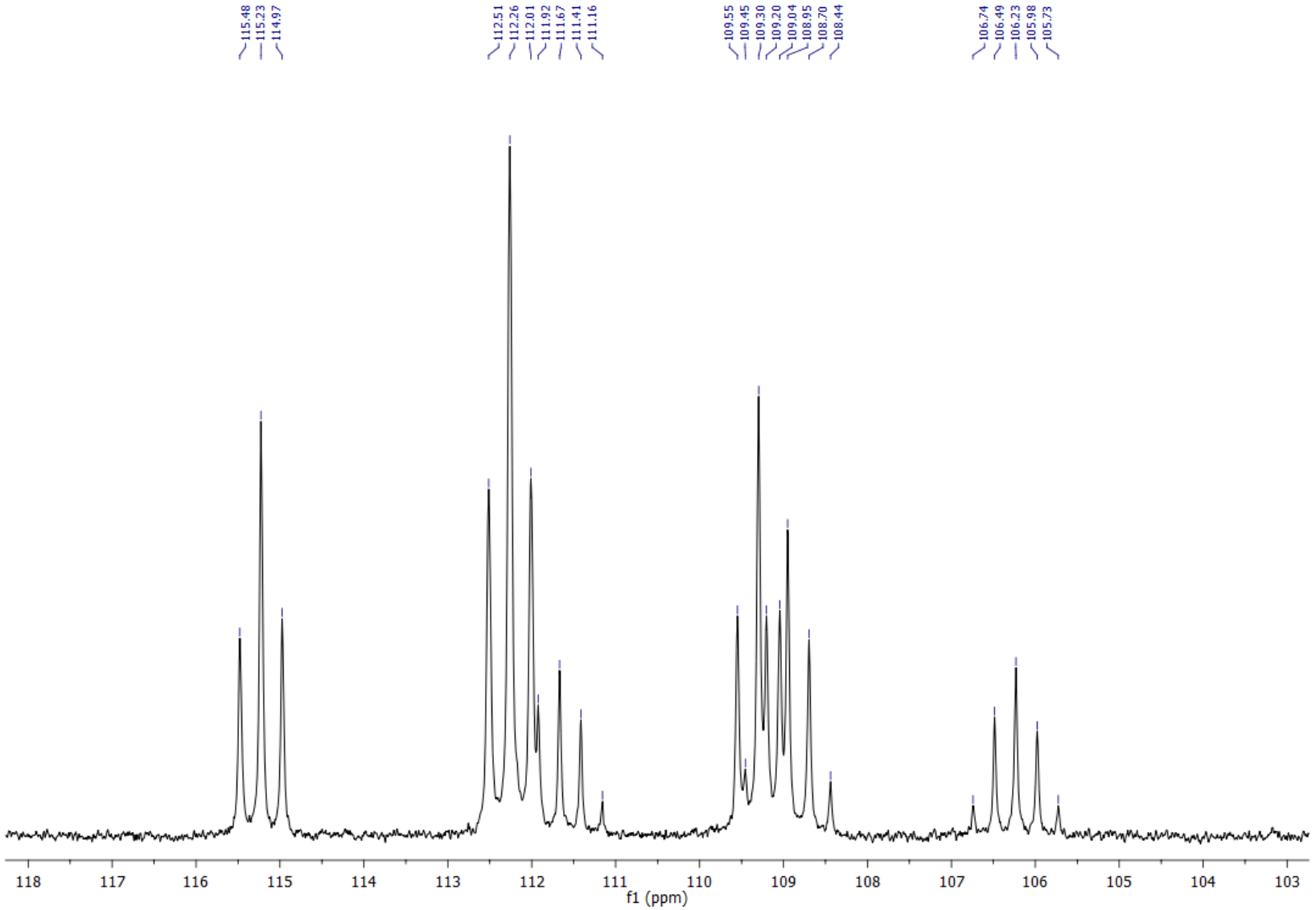

Figure S87: Excerpt of $^{13}C\{^{1}H\}$ NMR spectrum of neat [BMIm]**6cPFSI** with DMSO-d6 capillary.

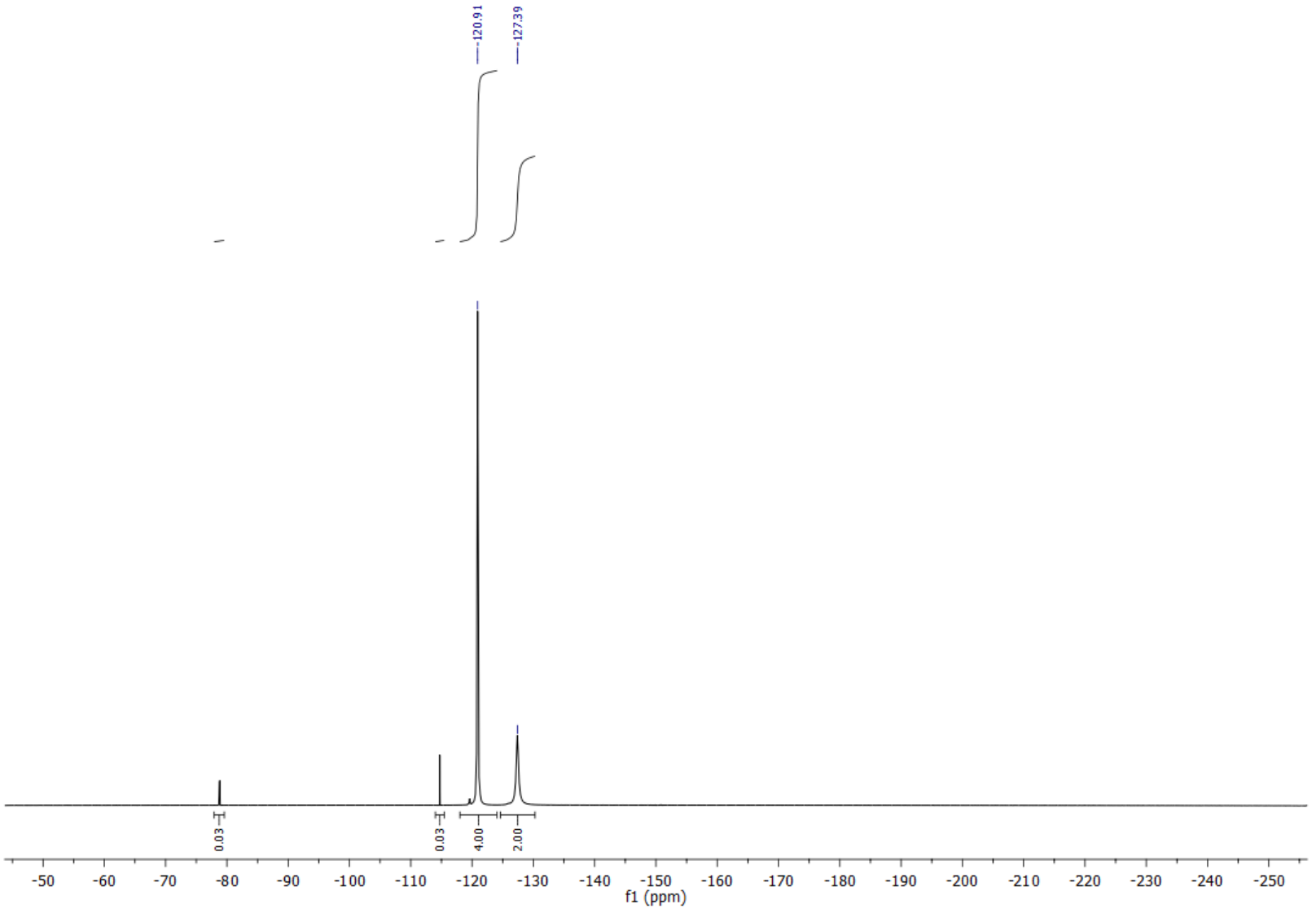

Figure S88: ^{19}F NMR spectrum of neat [BMIm]**6cPFSI** with DMSO-d6 capillary.

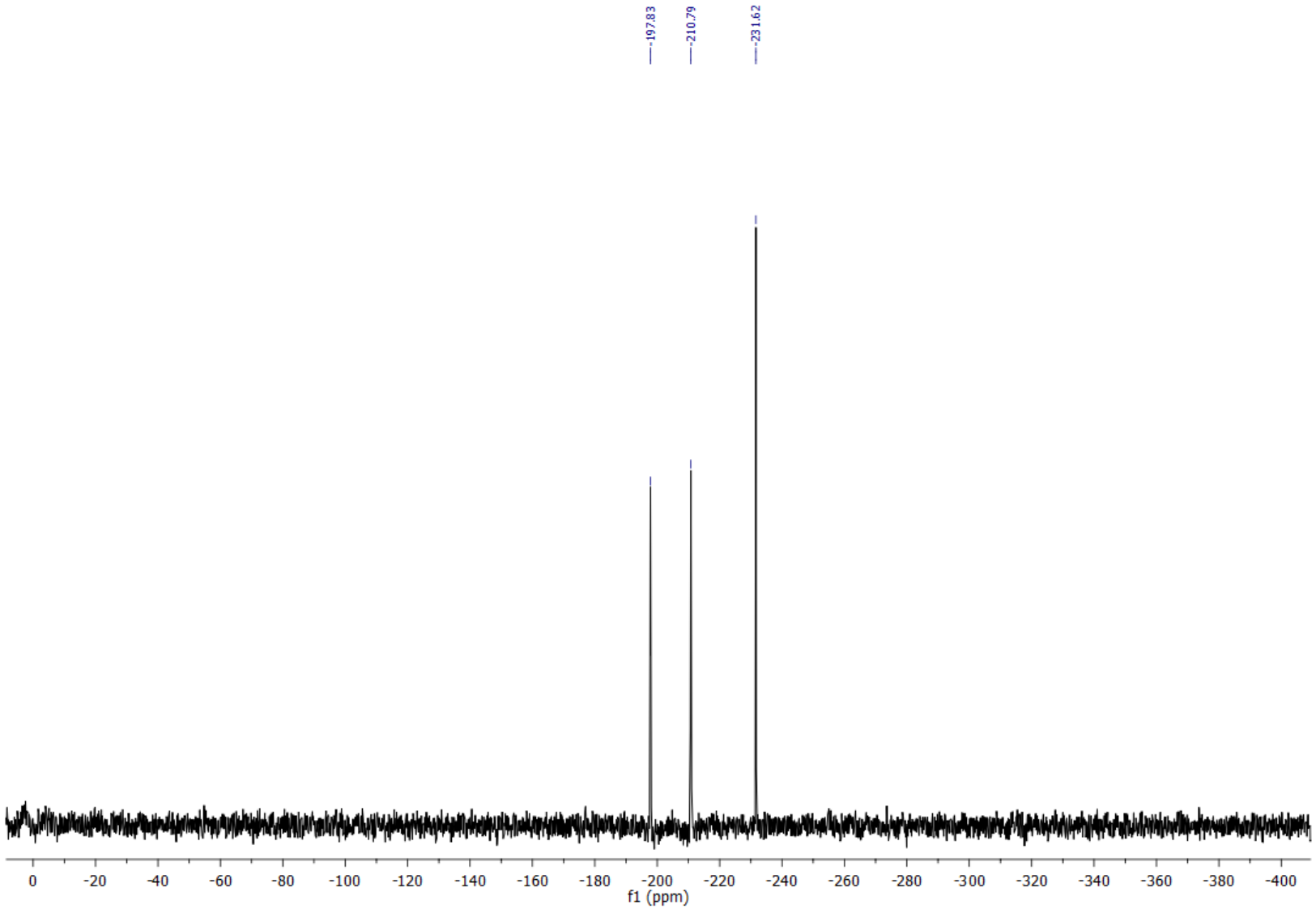

Figure S89: ^{15}N NMR spectrum of neat [BMIm]**6cPFSI** with DMSO-d6 capillary.

[BMPL]**4cPFSI**

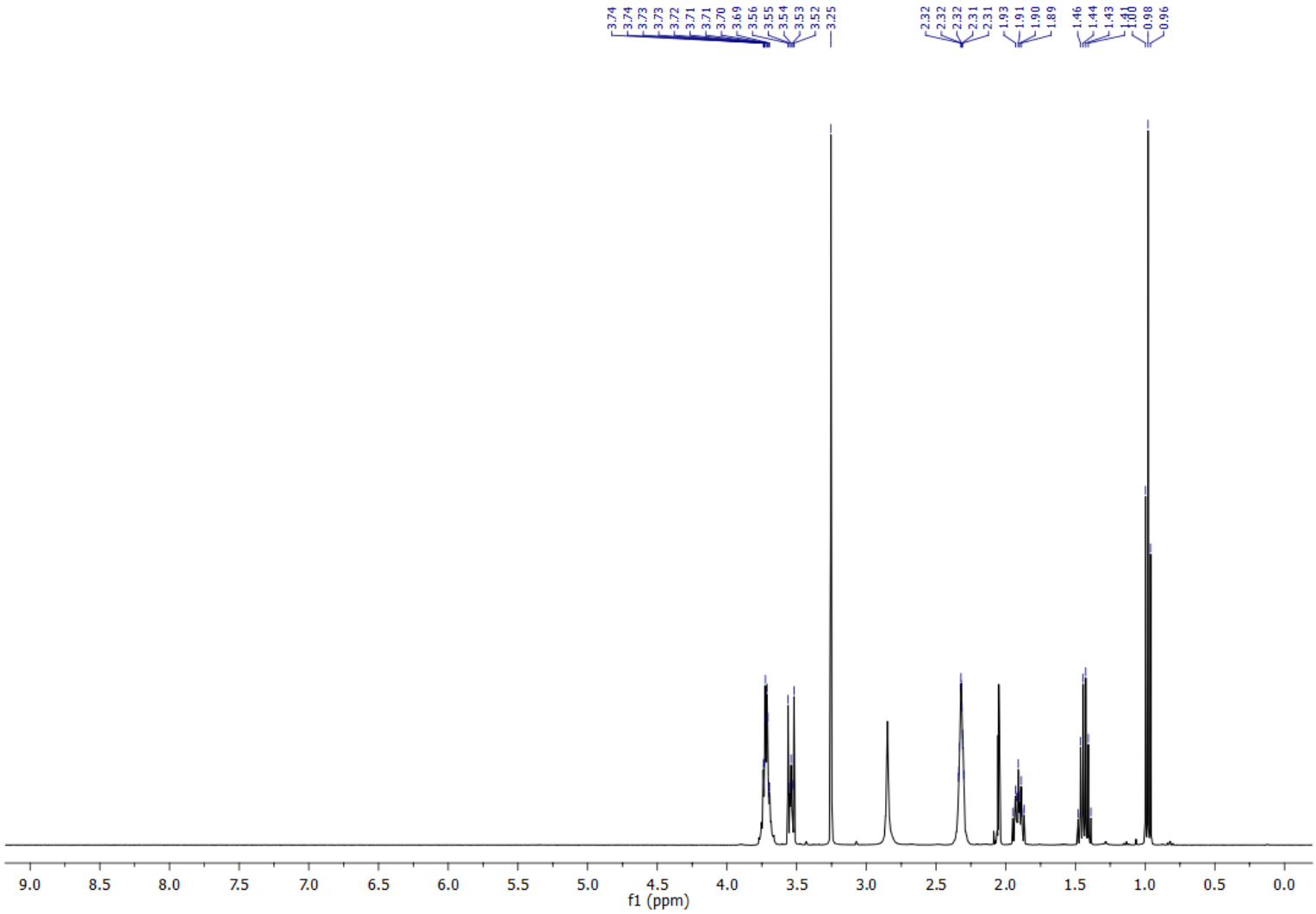

Figure S90: ^{1}H NMR spectrum of [BMPL]**4cPFSI** in acetone-d6.

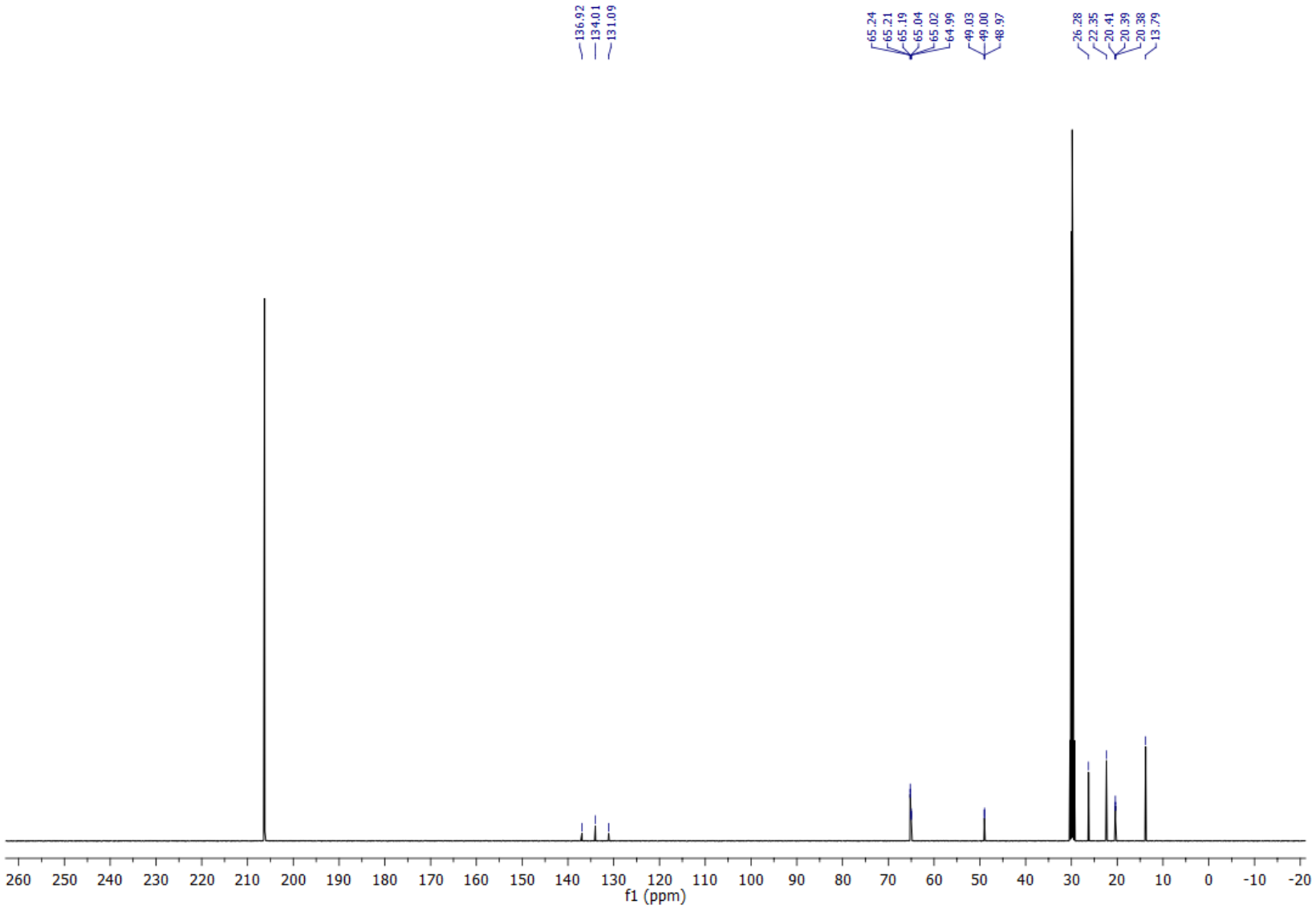

Figure S91: $^{13}C\{^{1}H\}$ NMR spectrum of [BMPL]**4cPFSI** in acetone-d6.

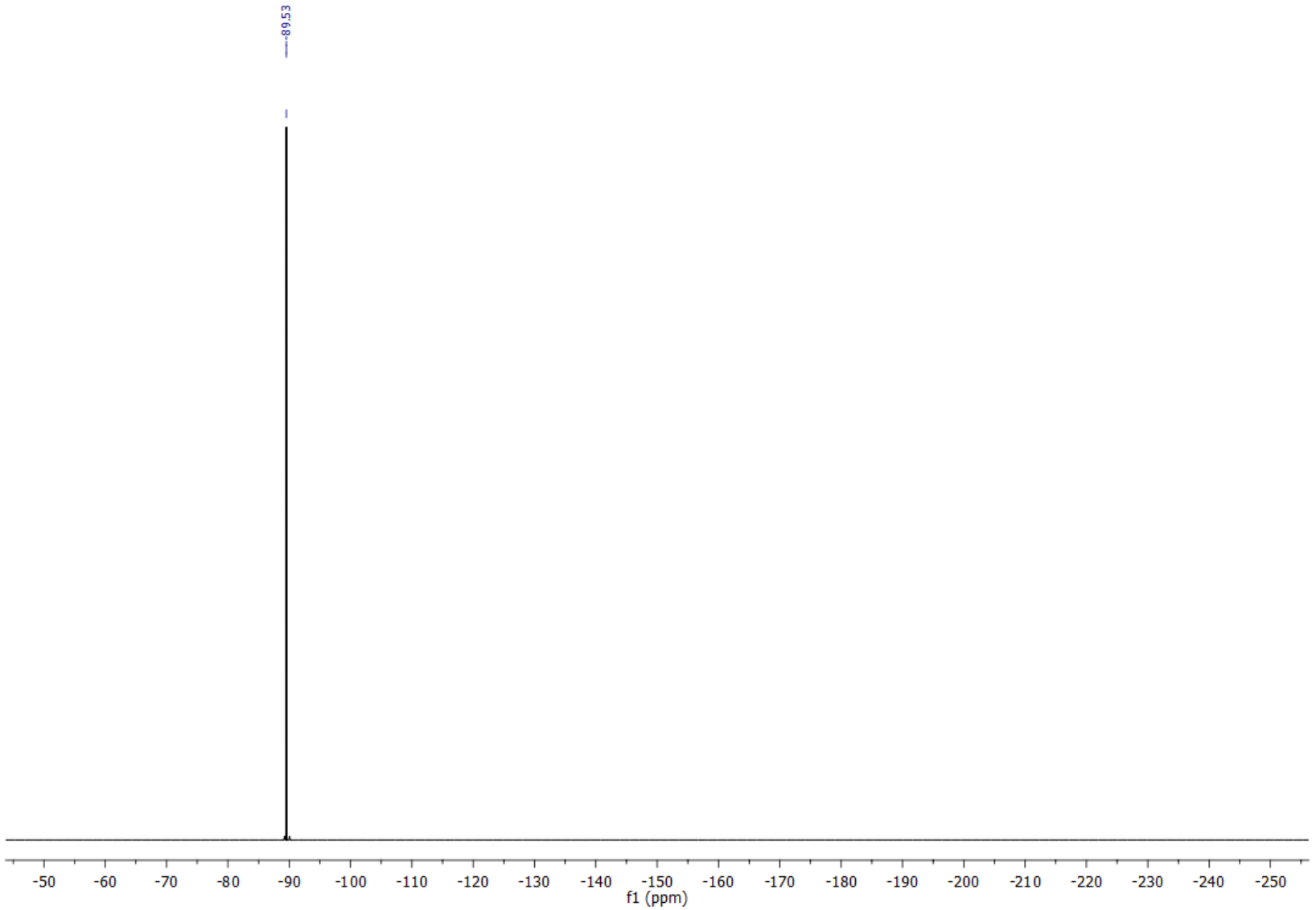

Figure S92: ^{19}F NMR spectrum of [BMPL]**4cPFSI** in acetone-d6.

[BMPL]**5cPFSI**

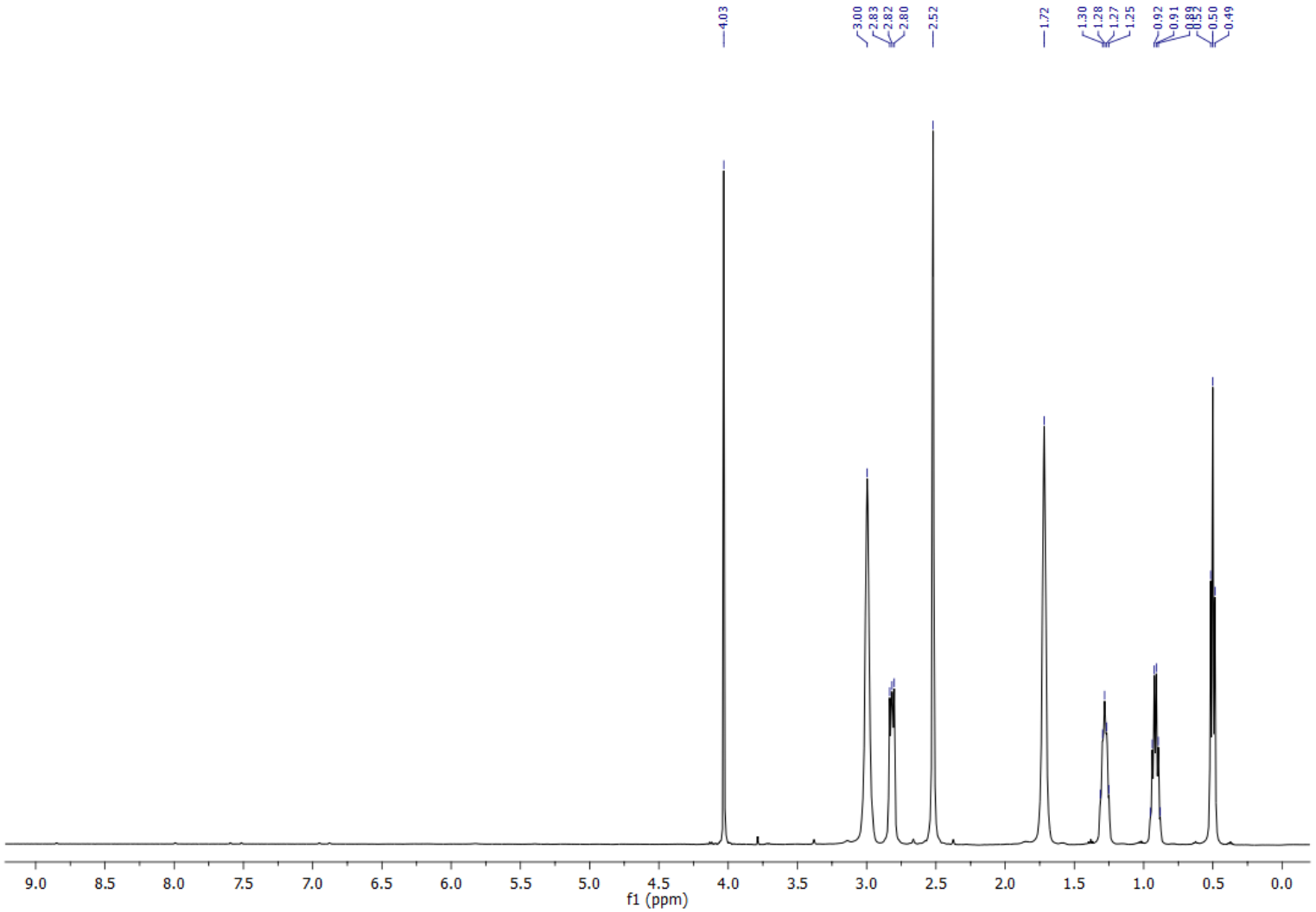

Figure S93: ^{1}H NMR spectrum of neat [BMPL]**5cPFSI** with DMSO-d6 capillary.

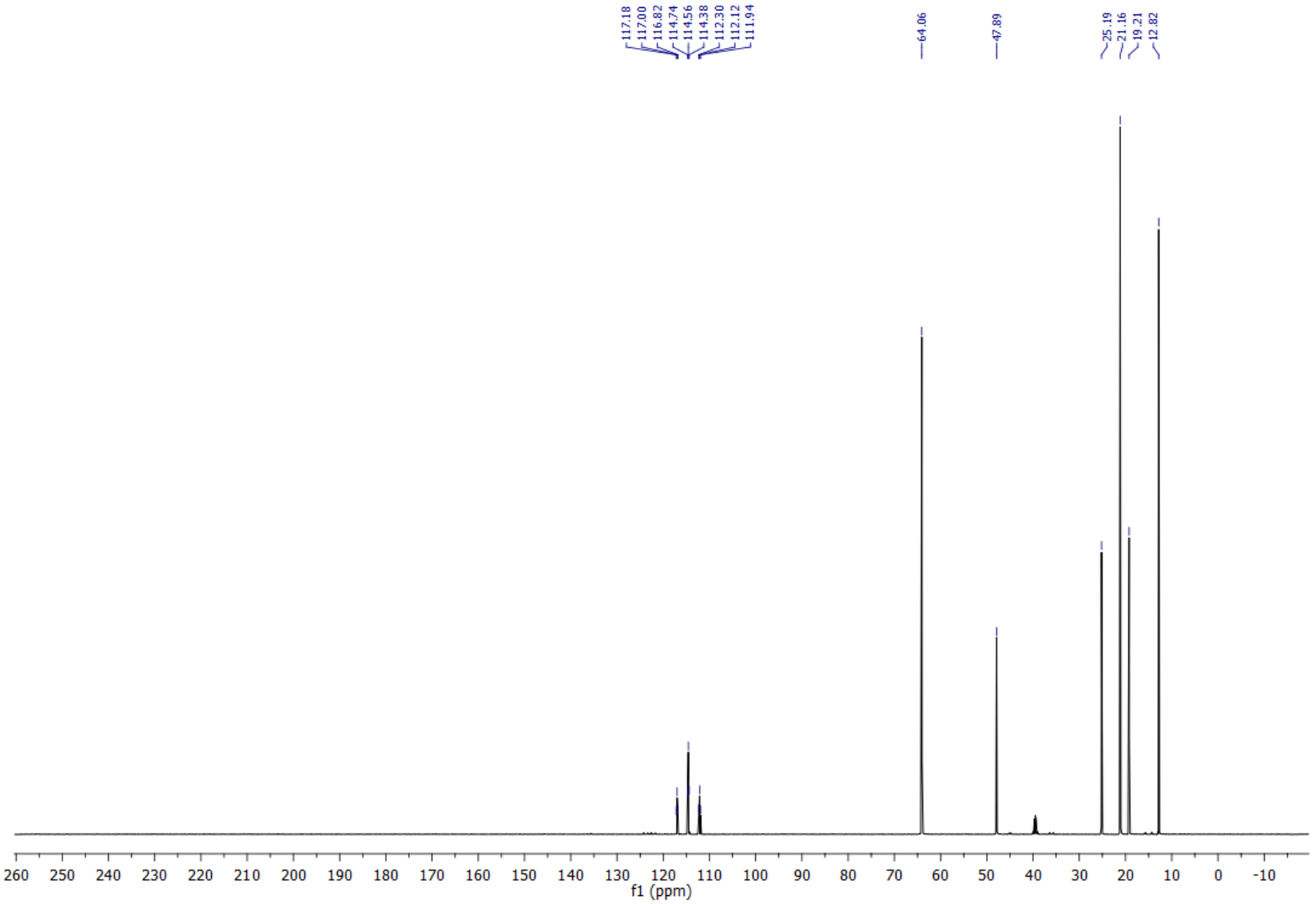

Figure S94: $^{13}C\{^{1}H\}$ NMR spectrum of neat [BMPL]**5cPFSI** with DMSO-d6 capillary.

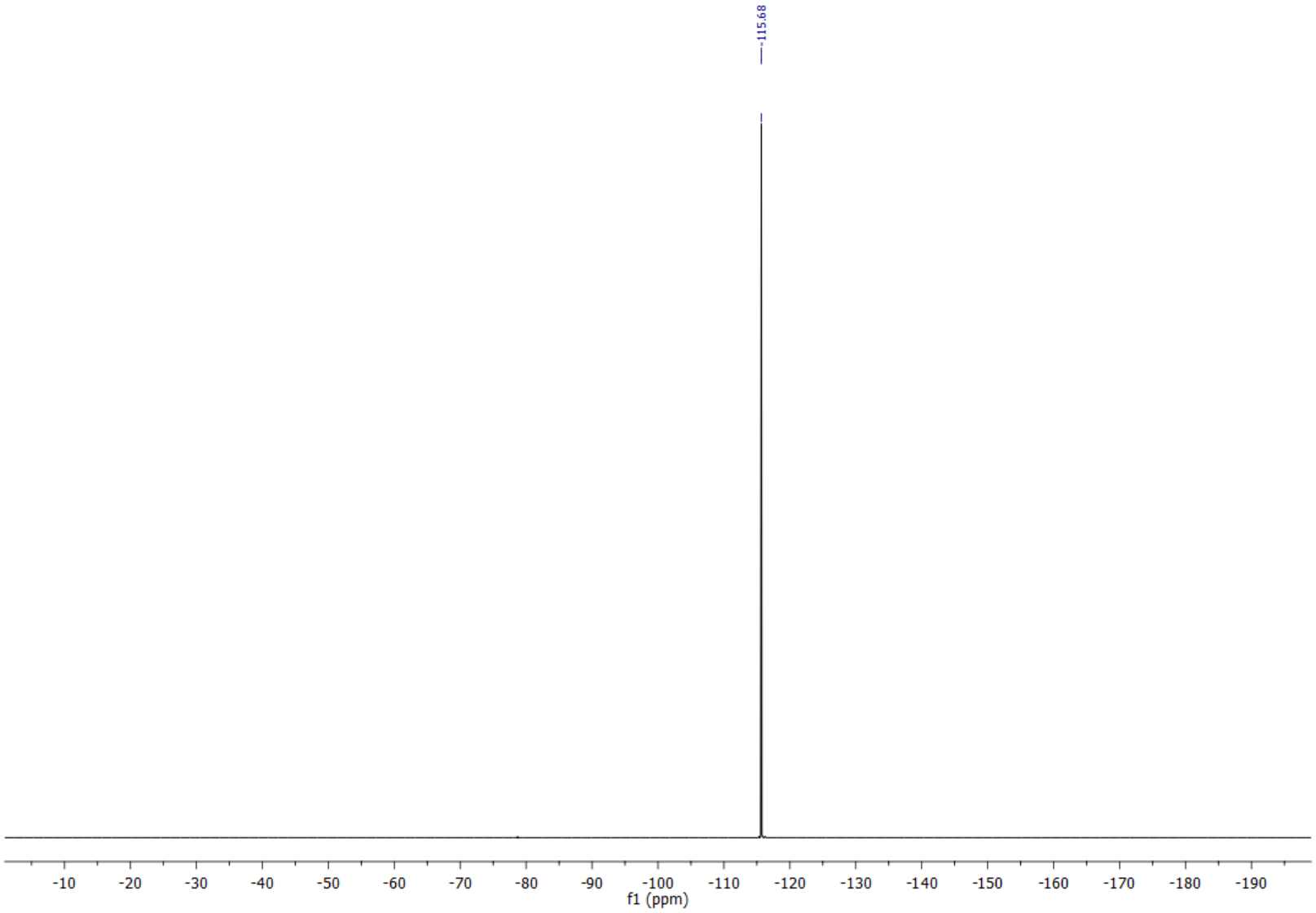

Figure S95: ^{19}F NMR spectrum of neat [BMPL]**5cPFSI** with DMSO-d6 capillary.

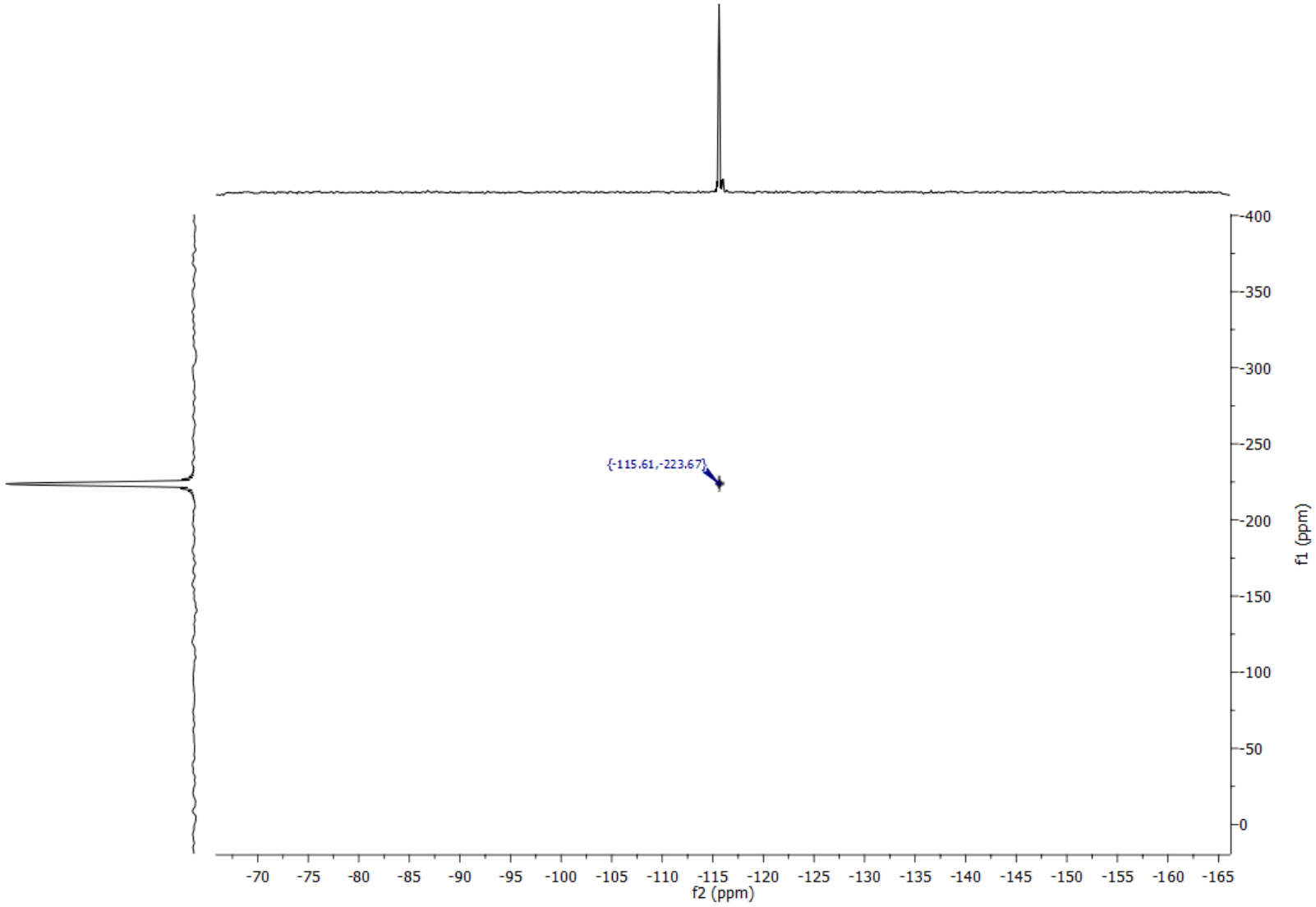

Figure S96: $^{19}F,^{15}N$ HMQC NMR spectrum of neat [BMPL]**5cPFSI** with DMSO-d6 capillary.

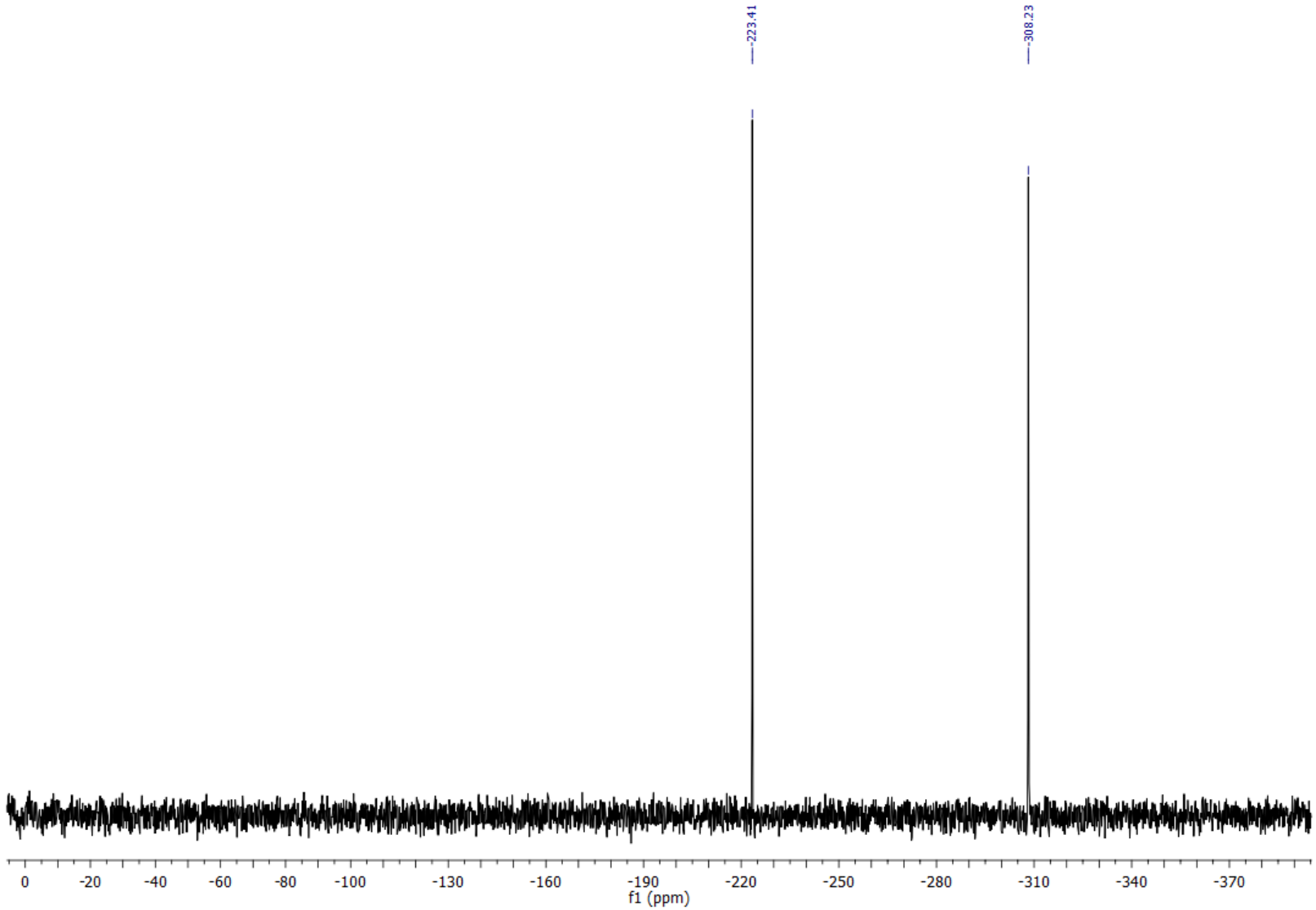

Figure S97: ^{15}N NMR spectrum of neat [BMPL]**5cPFSI** with DMSO-d6 capillary.

[BMPL]**6cPFSI**

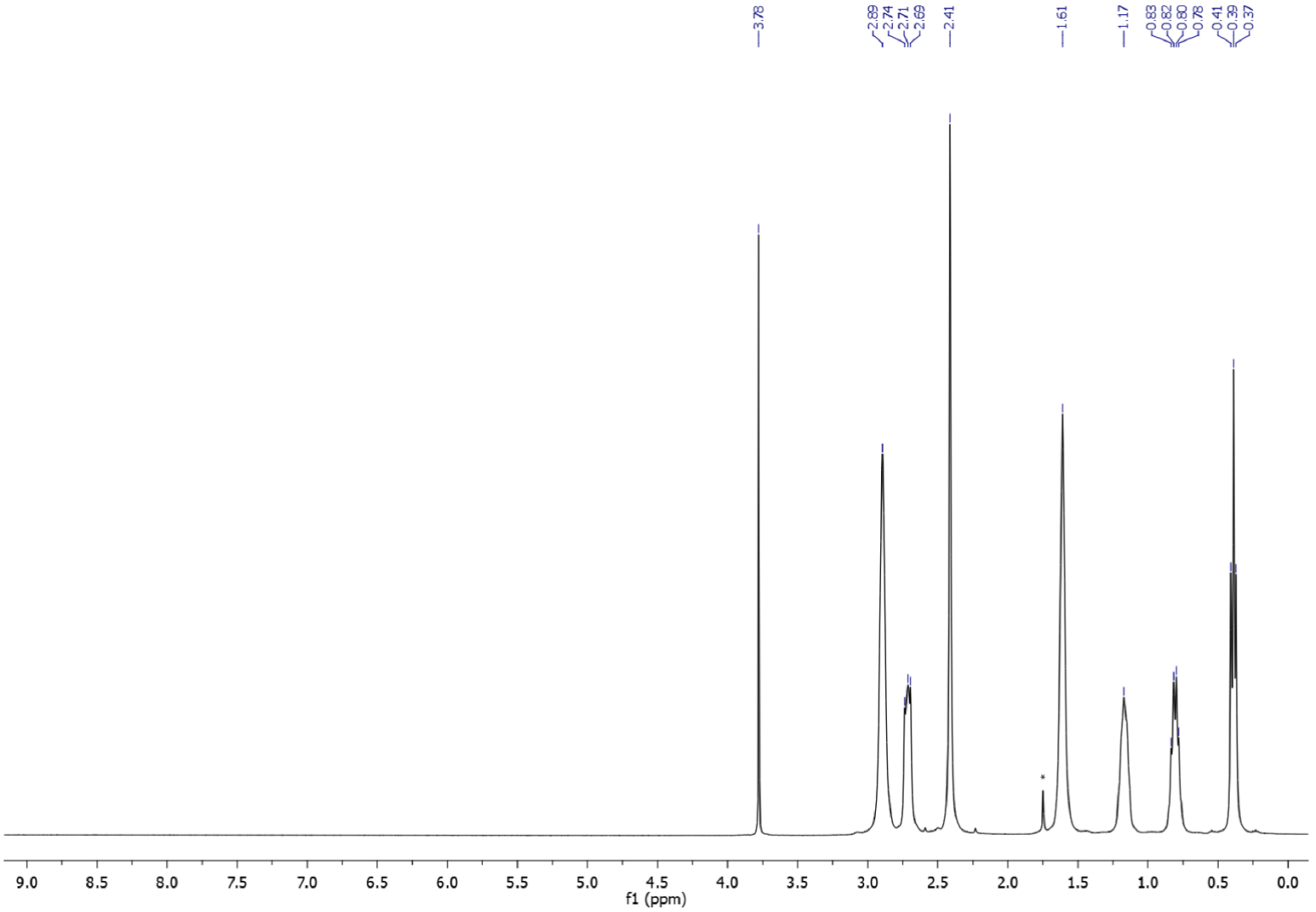

Figure S98: ^{1}H NMR spectrum of neat [BMPL]**6cPFSI** with DMSO-d6 capillary; *: residual water in DMSO-d6 capillary.

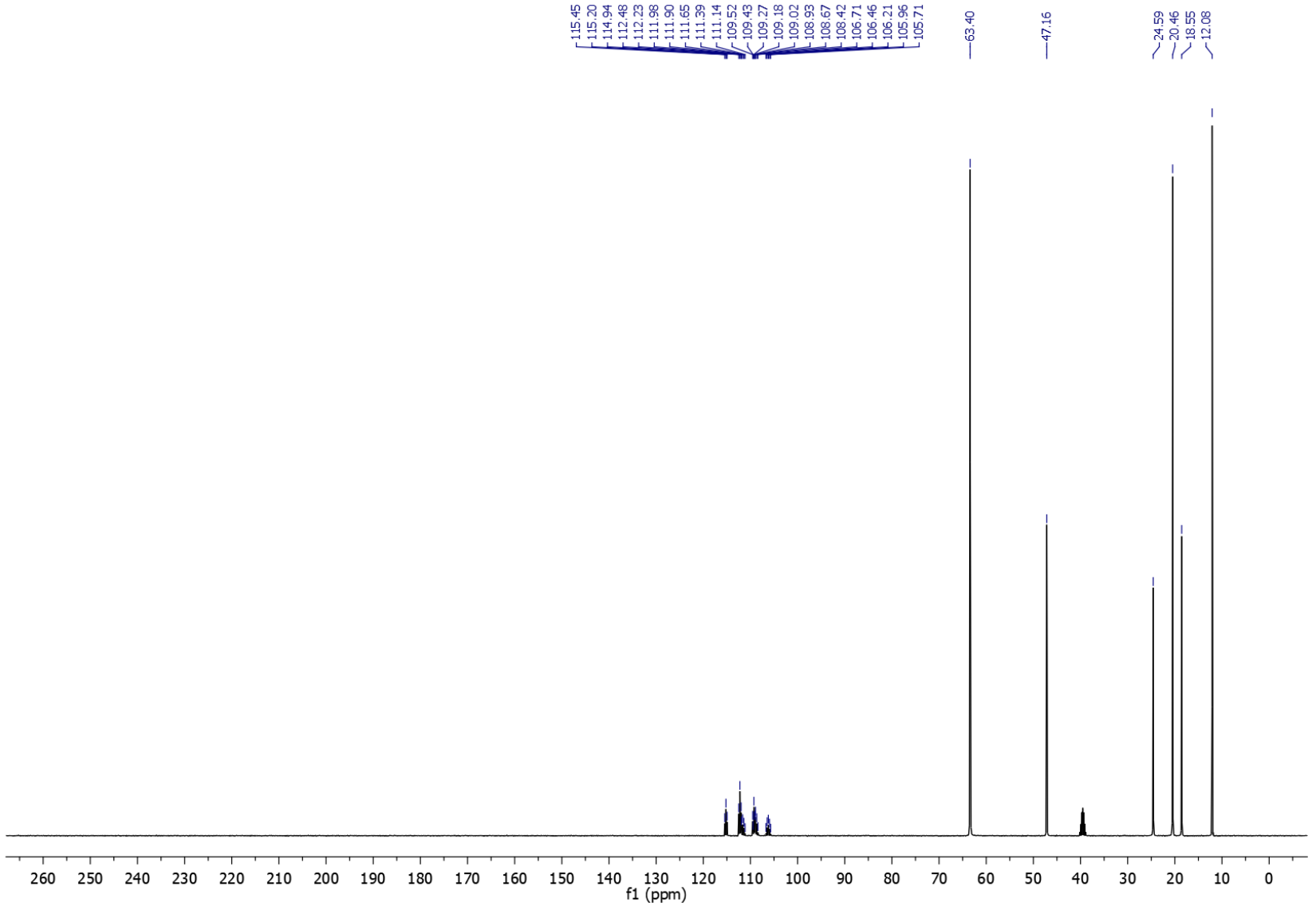

Figure S99: $^{13}C\{^{1}H\}$ NMR spectrum of neat [BMPL]**6cPFSI** with DMSO-d6 capillary.

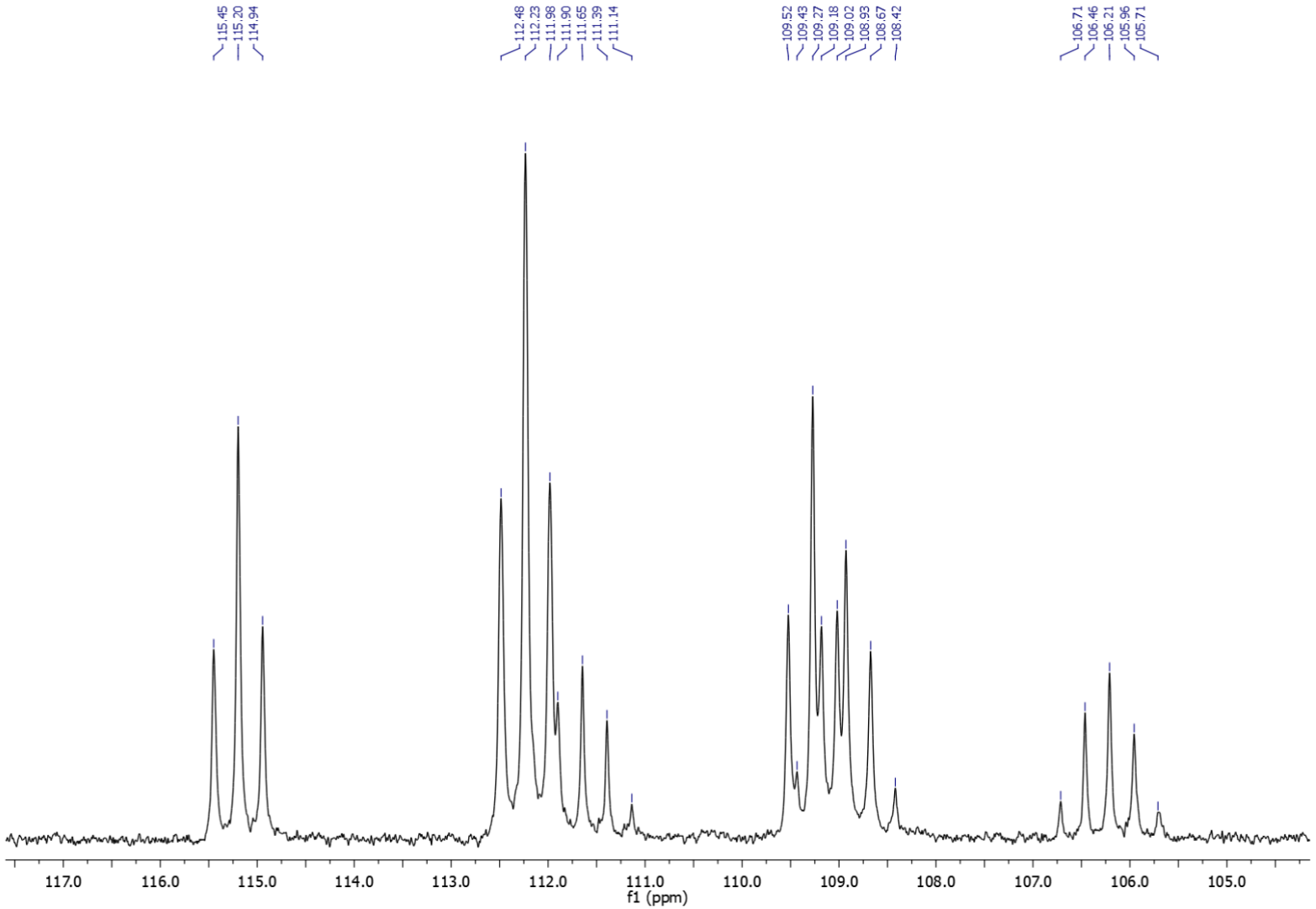

Figure S100: Excerpt of $^{13}C\{^{1}H\}$ NMR spectrum of neat [BMPL]**6cPFSI** with DMSO-d6 capillary.

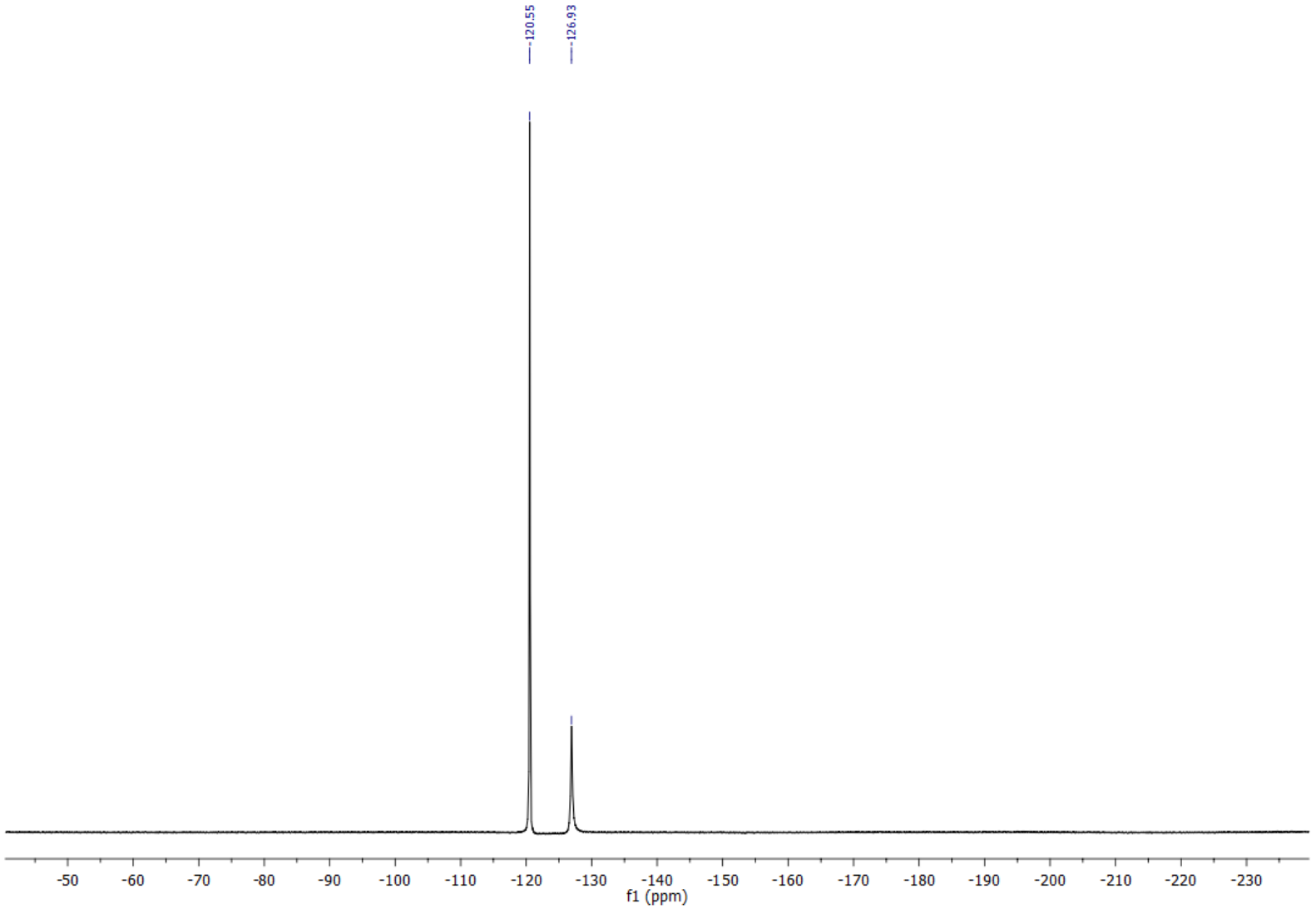

Figure S101: ^{19}F NMR spectrum of [BMPL]**6cPFSI** in acetone-d6.

Experimental

Chemical synthesis

Chemicals

[NH_4]**4cPFSI**, [NH_4]**5cPFSI** and K**4cPFSI** were synthesized according to literature procedures.[30] K**5cPFSI** was synthesized in a similar manner as described below. H**6cPFSI** was obtained from TCI in 98% purity, [EMIm]Cl and [BMPL]Cl were obtained from Merck in 98% purity and [BMIm]Cl was obtained from Sigma Aldrich in 98% purity. [EMIm]**TFSI** was obtained from abcr in 95-98% purity, [BMIm]**TFSI** in ≥99% purity and [BMPL]**TFSI** in 95-98% purity. The **TFSI**-ionic liquids were dried under vacuum for at least 24 h prior to analysis. The water content of the **TFSI**-ILs was determined by Karl-Fischer titration and found to be below 50 ppm.

Synthesis of K5cPFSI

Potassium hydroxide (7.97 g, 142.1 mmol) was added to a solution of [NH_4]**5cPFSI** (26.90 g, 103.39 mmol) in tetrahydrofuran (130 mL). The resulting suspension was stirred and refluxed for 18 h, until gas evolution had ceased. The reaction mixture was filtered, and the filter cake was extracted three times with tetrahydrofuran (3 x 7 mL). The solvent of the combined organic phases was removed under reduced pressure to yield an off-white solid. This solid was dissolved in water (115 mL) and activated carbon (granulated, 3.00 g) was added. The resulting suspension was heated under reflux for 190 min and filtered. The solvent of the filtrate was removed under reduced pressure. The residue was dried under vacuum for 16 h to yield 26.95 g of the title compound (95.83 mmol, 93%) as a colourless solid.

$^{13}C\{^1H\}$ NMR (acetone-d6, 126 MHz, δ in ppm): 115.7 (tt, $^1J(^{19}F,^{13}C)$ = 305.4 Hz, $^3J(^{19}F,^{13}C)$ = 22.6 Hz 2C).

^{19}F NMR (acetone-d6, 471 MHz, δ in ppm): −115.9 (s, 4F).

^{15}N NMR (acetone-d6, 51 MHz, δ in ppm): −222.8 (s, 1N).

HRMS ((−)-ESI): *m/z* (isotropic abundance) for $C_2F_4NO_4S_2$ calcd.: 241.92 (100.0), 242.92 (4.29) 243.92 (9.9); found: 241.92 (100.0), 242.92 (1.6), 243.9 (9.0).

Syntheses of the ionic liquids

General procedure

To an aqueous solution of the cation precursor, an aqueous solution of the anion precursor was added. The resulting mixture was stirred for two hours, and the organic phase was separated. The ionic liquids with the anions **5cPFSI** and **6cPFSI** were washed several times with double distilled water (5 mL per washing) until the halide test was found to be negative. Testing was performed by addition of a concentrated aqueous silver nitrate solution to the aqueous phase obtained from the washing procedure. The **4cPFSI**-ILs were washed three times with double distilled water (5 mL per washing). Since all three **4cPFSI**-ILs, *i.e.* [EMIm]**4cPFSI**, [BMIm]**4cPFSI** and [BMPL]**4cPFSI**, are slightly soluble in water and because they form [EMIm][Ag(**4cPFSI**)$_2$], [BMIm][Ag(**4cPFSI**)$_2$] and [BMPL][Ag(**4cPFSI**)$_2$] respectively,

which are insoluble in water, a negative Ag^+ test was not possible. The three complex salts [EMIm][Ag(**4cPFSI**)$_2$], [BMIm][Ag(**4cPFSI**)$_2$] and [BMPL][Ag(**4cPFSI**)$_2$] were obtained from the respective wash phase and characterized by SC-XRD (see Crystallographic Data).

The ionic liquids were dried in a fine vacuum at room temperature for at least 24 hours. The water content was determined by Karl Fischer titration and found to be below 50 ppm.

[EMIm]4cPFSI

[EMIm]Cl (6.95 g, 47.4 mmol) and [NH_4]**4cPFSI** (9.97 g, 47.4 mmol) yielded 12.2 g of the title compound (40.3 mmol, 85% yield) as a pale beige liquid.

^{1}H NMR (DMSO-d6 capillary, 500 MHz, δ in ppm): 7.98 (s, 1H, NC*H*N), 6.91 (m, 1H, C*H*CH), 6.85 (m, 1H, CHC*H*), 3.66 (q, ^{3}J(^{1}H,^{1}H) = 7.43 Hz, 2H, CH_2), 3.33 (s, 1H, NCH_3), 0.92 (t, ^{3}J(^{1}H,^{1}H) = 7.44 Hz, 3H, CH_3CH$_2$).

^{1}H NMR (acetone-d6, 400 MHz, δ in ppm): 8.85 (s, 1H, NC*H*N), 7.67 (m, 1H, C*H*CH), 7.60 (m, 1H, CHC*H*) 4.34 (q, ^3J(^{1}H,^{1}H) = 7.34 Hz, 2H, NCH_2CH$_3$) 4.00 (s, 1H, NCH_3), 1.54 (t, ^3J(^{1}H,^{1}H) = 7.36 Hz, 3H, CH$_2$CH_3).

^{13}C{^{1}H} NMR (DMSO-d6 capillary, 126 MHz, δ in ppm): 134.9 (s, 1C, N*C*HN), 132.1 (t, ^1J(^{19}F,^{13}C) = 366.5 Hz 1C, *C*F$_2$), 122.5 (m, 1C, CH*C*H), 120.9 (m, 1C, *C*HCH), 43.9 (s, 1C, *C*H$_2$), 35.0 (s, 1C, NC^{13}C{^{1}H} NMR (acetone-d6, 101 MHz, δ in ppm): 136.8 (s, 1C, N*C*HN), 133.8 (t, ^1J(^{19}F,^{13}C) = 367.4 Hz 1C, *C*F$_2$), 124.5 (s, 1C, *C*HCH), 122.8 (s, 1C, CH*C*H), 45.5 (s, 1C, *C*H$_2$CH$_3$), 36.5 (s, 1C, NC^{19}F NMR (DMSO-d6 capillary, 471 MHz, δ in ppm): −88.2 (s, 2F).

^{19}F NMR (acetone-d6, 377 MHz, δ in ppm): −88.0 (t, ^3J(^{19}F,^{14}N) = 2.5 Hz, 2F).

^{15}N NMR (DMSO-d6 capillary, 51 MHz, δ in ppm): −175.6 (s, 1N, *N*(SO$_2$)$_2$).

HRMS ((+)-ESI): *m/z* (isotropic abundance) for $C_6H_{11}N_2$ calcd.:111.09 (100.0), 112.10 (6.6); found: 111.09 (100.0), 112.10 (6.8).

HRMS ((−)-ESI): *m/z* (isotropic abundance) for $CF_2NO_4S_2$ calcd.: 191.92 (100.0), 193.92 (9.1), 192.92 (2.0); found: 191.92 (100.0), 193.92 (9.1), 192.92 (1.5).

Elemental analysis calcd. (%) for $C_7H_{11}F_2N_3O_4S_2$: C 27.72, H 3.66, N 13.85, S 21.14; found: C 27.85, H 3.59, N 14.09, S 21.49.

[EMIm]5cPFSI

[EMIm]Cl (5.71 g, 38.9 mmol) and [NH_4]**5cPFSI** (8.18 g, 38.9 mmol) yielded 8.06 g of the title compound (22.8 mmol, 59% yield) as a pale beige liquid.

^{1}H NMR (DMSO-d6 capillary, 500 MHz, δ in ppm): 7.98 (s, 1H, NC*H*N), 6.91 (m, 1H, C*H*CH), 6.85 (m, 1H, CHC*H*), 3.66 (q, ^3J(^{1}H,^{1}H) = 7.43 Hz, 2H, CH_2), 3.33 (s, 1H, NCH_3), 0.92 (t, ^3J(^{1}H,^{1}H) = 7.44 Hz, 3H, CH_3CH$_2$).

^{1}H NMR (acetone-d6, 400 MHz, δ in ppm): 8.97 (s, 1H, NC*H*N), 7.75 (t, ^3J(^{1}H,^{1}H) = 1.8 Hz, 1H, C*H*CH), 7.67 (t, ^3J(^{1}H,^{1}H) = 1.8 Hz, 1H, CHC*H*), 4.39 (q, ^3J(^{1}H,^{1}H) = 7.33 Hz, 2H, NCH_2CH$_3$), 4.04 (s, 1H, NCH_3), 1.56 (t, ^3J(^{1}H,^{1}H) = 7.33 Hz, 3H, CH$_2$CH_3).

$^{13}C\{^{1}H\}$ NMR (DMSO-d6 capillary, 126 MHz, δ in ppm): 135.0 (s, 1C, N*C*HN), 113.9 (tt, $^{1}J(^{19}F,^{13}C)$ = 305.6 Hz, $^{3}J(^{19}F,^{13}C)$ = 22.9 Hz, 2C, C_2F_4), 122.9 (m, 1C, CH*C*H), 121.1 (m, 1C, *C*HCH), 44.2 (s, 1C, CH_2), 35.2 (s, 1C, N*C*$^{13}C\{^{1}H\}$ NMR (acetone-d6, 101 MHz, δ in ppm): 137.0 (s, 1C, N*C*HN), 124.7 (s, 1C, *C*HCH), 123.0 (s, 1C, CH*C*H), 115.6 (tt, $^{1}J(^{19}F,^{13}C)$ = 305.8 Hz, $^{3}J(^{19}F,^{13}C)$ = 22.4 Hz, 2C, C_2F_4), 45.6 (s, 1C, CH_2CH_3), 36.5 (s, 1C, N*C*^{19}F NMR (DMSO-d6 capillary, 471 MHz, δ in ppm): −115.9 (s, 4F).

^{19}F NMR (acetone-d6, 377 MHz, δ in ppm): −115.9 (s, 4F).

^{15}N NMR (DMSO-d6 capillary, 51 MHz, δ in ppm): −224.2 (s, 1N, $N(SO_2)_2$)), −211.0, −195.7.

HRMS ((+)-ESI): *m/z* (isotropic abundance) for $C_6H_{11}N_2$ calcd.: 111.09 (100.0), 112.09 (7.39), 113.09 (0.24); found: 111.09 (100.0), 112.09 (6.34).

HRMS ((−)-ESI): *m/z* (isotropic abundance) for $C_2F_4NO_4S_2$ calcd.: 241.92 (100.0), 242.92 (4.29) 243.92 (9.9); found: 241.92 (100.0), 242.92 (2.3), 243.9 (9.1).

Elemental analysis calcd. (%) for $C_8H_{11}F_4N_3O_4S_2$: C 27.20, H 3.14, N 11.87, S 18.15; found: C 27.19, H 2.98, N 12.36, S 18.04.

[EMIm]6cPFSI

A solution of [EMIm]Cl (2.61 g, 17.8 mmol) in water (3 mL) and a solution of H**6cPFSI** (4.02 g, 13.7 mmol) in water (9 mL) were combined and stirred for 5 min. Instantaneous precipitation of a colourless solid was detected. The resulting suspension was filered, and the filter cake was washed three times with water (3 x 5 mL). The solid residue was dried under vacuum for 24 h to yield 5.44 g of the title compound (13.5 mmol, 98% isolated yield) as colourless solid.

^{1}H NMR (acetone-d6, 400 MHz, δ in ppm): 9.12 (s, 1H, NC*H*N), 7.75 (m, 1H, C*H*CH), 4.41 (m, 1H, CHC*H*), 4.06 (q, $^{3}J(^{1}H,^{1}H)$ = 7.43 Hz, 2H, CH_2), 3.33 (s, 1H, NCH_3), 0.92 (t, $^{3}J(^{1}H,^{1}H)$ = 7.44 Hz, 3H, CH_3CH$_2$).

$^{13}C\{^{1}H\}$ NMR (acetone-d6, 126 MHz, δ in ppm): 137.2 (s, 1C, N*C*HN), 113.0 (tt, $^{1}J(^{19}F,^{13}C)$ = 297.8 Hz, $^{3}J(^{19}F,^{13}C)$ = 25.1 Hz, 4C, S*C*F$_2$), 110.0 (tp, $^{1}J(^{19}F,^{13}C)$ = 272.5 Hz, $^{3}J(^{19}F,^{13}C)$ = 25.5Hz, 2C, C*C*F$_2$C) 123.9 (s, 1C, CH*C*H), 122.2 (s, 1C, *C*HCH), 44.9 (s, 1C, *C*H$_2$), 35.7 (s, 1C, N*C*^{19}F NMR (acetone-d6, 471 MHz, δ in ppm): −120.6 (s, 4F, SCF_2), −127.0 (s, 2F, CCF_2C).

HRMS ((+)-ESI): *m/z* (isotropic abundance) for $C_6H_{11}N_2$ calcd.: 111.09 (100.0), 112.09 (7.39), 113.09 (0.24); found: 111.09 (100.0), 112.10 (6.55).

HRMS ((−)-ESI): *m/z* (isotropic abundance) for $C_3F_6NO_4S_2$: calcd.: 291.92 (100.0), 293.91 (9.0), 292.92 (5.0); found: 291.92 (100.0), 293.91 (8.9), 292.92 (3.2).

Elemental analysis calcd. (%) for $C_9H_{11}F_6N_3O_4S_2$: C 26.80, H 2.75, N 10.42, S 15.90; found: C 26.85, H 2.47, N 10.46, S 15.85.

[BMIm]4cPFSI

[BMIm]Cl (7.711 g, 44.15 mmol) and [NH_4]**4cPFSI** (7.59 g, 36.12 mmol) gave 7.36 g of the title compound (22.2 mmol, 61% yield) as a colourless liquid.

^{1}H NMR (DMSO-d6 capillary, 400 MHz, δ in ppm): 8.03 (s, 1H, NC*H*N), 6.95 (m, 1H, NC*H*CHN), 6.89 (m, 1H, NCHC*H*N), 3.65 (t, $^{3}J(^{1}H,^{1}H)$ = 7.43 Hz, 2H, NCH_2CH$_2$) 3.37 (s, 3H, NCH_3), 1.31 (m, 2H, NCH$_2$CH_2), 0.78 (m, 2H, CH$_3$CH_2), 0.35 (t, $^{3}J(^{1}H,^{1}H)$ = 7.52 Hz, 3H, CH_3CH$_2$).

^{1}H NMR (acetone-d6, 400 MHz, δ in ppm): 8.89 (s, 1H, NC*H*N), 7.50 (m, 1H, NC*H*CHN), 7.36 (m, 1H, NC*H*CHN), 4.06 (t, $^{3}J(^{1}H,^{1}H)$ = 7.40 Hz, 2H, NCH_2CH$_2$) 3.30 (s, 3H, NCH_3), 1.60 (m, 2H, NCH$_2$CH_2), 1.15 (m, 2H, CH$_3$CH_2), 0.53 (t, $^{3}J(^{1}H,^{1}H)$ = 7.47 Hz, 3H, CH_3CH$_2$).

^{13}C{^{1}H} NMR (DMSO-d6 capillary, 126 MHz, δ in ppm): 135.2 (s, 1C, N*C*HN), 132.3 (m, 1C, *C*F$_2$), 122.7 (s, 1C, *C*HCH), 121.4 (s, 1C, CH*C*H), 48.6 (s, 1C, N*C*H$_2$), 35.1 (s, 1C, N*C*30.7 (s, 1C, NCH$_2$*C*H$_2$) ^{13}C{^{1}H} NMR (acetone-d6, 101 MHz, δ in ppm): 137.0 (s, 1C, N*C*HN), 132.3 (t, $^{1}J(^{19}F,^{13}C)$ = 366.4 Hz 1C, *C*F$_2$), 124.0 (s, 1C, *C*HCH), 121.7 (s, 1C, CH*C*H), , 49.6 (s, 1C, N*C*H$_2$), 35.2 (s, 1C, N*C*31.3 (s, 1C, NCH$_2$*C*H$_2$), ^{19}F NMR (DMSO-d6 capillary, 471 MHz, δ in ppm): −88.2 (s, 2F).

^{19}F NMR (acetone-d6, 377 MHz, δ in ppm): −88.2 (s, 2F).

^{15}N NMR (DMSO-(DMSO-d6 capillary, 471 MHz, δ in ppm): −210.5, −197.9, −175.4 (s, 1N, *N*(SO$_2$)$_2$)).

HRMS ((+)-ESI): *m/z* (isotropic abundance) for $C_8H_{15}N_2$ calcd.: 139.12 (100.0), 140.13 (8.8); found: 139.12 (100.0), 140.13 (8.9).

HRMS ((−)-ESI): *m/z* (isotropic abundance) for $CF_2NO_4S_2$ calcd.: 191.92 (100.0), 193.92 (9.1), 192.92 (2.0); found: 191.92 (100.0), 193.92 (9.1), 192.92 (1.4).

Elemental analysis calcd. (%) for $C_9H_{15}F_2N_3O_4S_2$: C 32.62, H 4.56, N 12.68, S 19.35; found: C 32.74, H 4.80, N 12.98, S 19.50.

[BMIm]5cPFSI

[BMIm]Cl (4.94 g, 28.3 mmol) and K**5cPFSI** (6.62 g, 23.5 mmol) gave 6.89 g of the title compound (18.1 mmol, 78% yield) as a colourless liquid.

^{1}H NMR (DMSO-d6 capillary, 400 MHz, δ in ppm): 7.90 (s, 1H, NC*H*N), 6.84 (m, 1H, NC*H*CH/NCHC*H*), 6.77 (m, 1H, NCHC*H*/NC*H*CH), 3.55 (t, $^{3}J(^{1}H,^{1}H)$ = 7.45 Hz, 2H, NCH_2CH$_2$) 3.27 (s, 3H, NCH_3), 1.24 (m, 2H, NCH$_2$CH_2), 0.73 (m, 2H, CH$_3$CH_2), 0.29 (t, $^{3}J(^{1}H,^{1}H)$ = 7.51 Hz, 3H, CH_3CH$_2$).

^{1}H NMR (acetone-d6, 400 MHz, δ in ppm): 8.85 (s, 1H, NC*H*N), 7.40 (m, 1H, NC*H*CHN), 7.32 (m, 1H, NC*H*CHN), 3.95 (t, $^{3}J(^{1}H,^{1}H)$ = 7.40 Hz, 2H, NCH_2CH$_2$) 3.29 (s, 3H, NCH_3), 1.50 (m, 2H, NCH$_2$CH_2), 1.07 (m, 2H, CH$_3$CH_2), 0.51 (t, $^{3}J(^{1}H,^{1}H)$ = 7.47 Hz, 3H, CH_3CH$_2$).

^{13}C{^{1}H} NMR (DMSO-d6 capillary, 126 MHz, δ in ppm): 135.0 (s, 1C, N*C*HN), 122.5 (s, 1C, *C*HCH), 121.2 (s, 1C, CH*C*H), 113.4 (tt, $^{1}J(^{19}F,^{13}C)$ = 307.2 Hz, $^{3}J(^{19}F,^{13}C)$ = 22.7 Hz, 2C, C_2F_4), 48.4 (s, 1C, N*C*H$_2$), 34.8 (s, 1C, N*C*30.6 (s, 1C, NCH$_2$*C*H$_2$) ^{13}C{^{1}H} NMR (acetone-d6, 101 MHz, δ in ppm): 137.2 (s, 1C, N*C*HN), 124.4 (s, 1C, *C*HCH), 121.9 (s, 1C, CH*C*H), 112.7 (tt, $^{1}J(^{19}F,^{13}C)$ = 307.3 Hz, $^{3}J(^{19}F,^{13}C)$ = 22.5 Hz, 2C, C_2F_4), 50.0 (s, 1C, N*C*H$_2$), 35.0 (s, 1C, N*C*32.5 (s, 1C, NCH$_2$*C*H$_2$), ^{19}F NMR (DMSO-d6 capillary, 471 MHz, δ in ppm): −115.8 (s, 4F).

^{19}F NMR (acetone-d6, 377 MHz, δ in ppm): −115.9 (s, 4F).

HRMS ((+)-ESI): *m/z* (isotropic abundance) for $C_8H_{15}N_2$ calcd.: 139.12 (100.0), 140.13 (8.8); found: 139.12 (100.0), 140.13 (9.1).

HRMS ((−)-ESI): *m/z* (isotropic abundance) for $C_2F_4NO_4S_2$ calcd.: 241.92 (100.0), 242.92 (4.29), 243.92 (9.9); found: 241.92 (100.0), 242.92 (1.4), 243.9 (8.8).

Elemental analysis calcd. (%) for $C_{10}H_{15}F_4N_3O_4S_2$: C 31.50, H 3.96, N 11.02, S 16.81; found: C 31.54, H 3.98, N 11.44, S 16.75.

[BMIm]6cPFSI

[BMIm]Cl (3.11 g, 17.8 mmol) and H**6cPFSI** (4.12 g, 14.1 mmol) yielded 5.38 g of the title compound (12.47 mmol, 89% yield) as a colourless liquid.

^{1}H NMR (DMSO-d6 capillary, 400 MHz, δ in ppm): 7.97 (s, 1H, NC*H*N), 6.86 (m, 1H, NC*H*CHN), 6.79 (m, 1H, NCHC*H*N), 3.59 (t, $^3J(^1H,^1H)$ = 7.44 Hz, 2H, NC*H*$_2$CH$_2$) 3.31 (s, 3H, NC*H*$_3$), 1.27 (m, 2H, NCH$_2$C*H*$_2$), 0.75 (m, 2H, CH$_3$C*H*$_2$), 0.32 (t, $^3J(^1H,^1H)$ = 7.51 Hz, 3H, C*H*$_3$CH$_2$).

^{1}H NMR (acetone-d6, 400 MHz, δ in ppm): 8.98 (s, 1H, NC*H*N), 7.72 (m, 1H, NC*H*CHN), 7.66 (m, 1H, NC*H*CHN), 4.33 (t, $^3J(^1H,^1H)$ = 7.29 Hz, 2H, NC*H*$_2$CH$_2$) 4.02 (s, 3H, NC*H*$_3$), 1.90 (m, 2H, NCH$_2$C*H*$_2$), 1.37 (m, 2H, CH$_3$C*H*$_2$), 0.93 (t, $^3J(^1H,^1H)$ = 7.38 Hz, 3H, C*H*$_3$CH$_2$).

^{13}C{^{1}H} NMR (DMSO-d6 capillary, 126 MHz, δ in ppm): 135.4 (s, 1C, N*C*HN), 122.8 (s, 1C, *C*HCH), 121.5 (s, 1C, CH*C*H), 112.3 (tt, $^1J(^{19}F,^{13}C)$ = 298.5 Hz, $^3J(^{19}F,^{13}C)$ = 25.3 Hz, 2C, S*C*F$_2$), 109.1 (tp, $^1J(^{19}F,^{13}C)$ = 273.8 Hz, $^3J(^{19}F,^{13}C)$ = 25.5 Hz, 1C, C*C*F$_2$C), 48.8 (s, 1C, N*C*H$_2$), 35.0 (s, 1C, N*C*31.0 (s, 1C, NCH$_2$*C*H$_2$) ^{13}C{^{1}H} NMR (acetone-d6, 101 MHz, δ in ppm): 137.3 (s, 1C, N*C*HN), 124.7 (s, 1C, *C*HCH), 123.3 (s, 1C, CH*C*H), 113.8 (tt, $^1J(^{19}F,^{13}C)$ = 297.7 Hz, $^3J(^{19}F,^{13}C)$ = 25.2 Hz, 2C, S*C*F$_2$), 110.7 (tp, $^1J(^{19}F,^{13}C)$ = 274.0 Hz, $^3J(^{19}F,^{13}C)$ = 25.6 Hz, 1C, C*C*F$_2$C), 50.2 (s, 1C, N*C*H$_2$), 36.6 (s, 1C, N*C*32.6 (s, 1C, NCH$_2$*C*H$_2$), ^{15}N NMR (DMSO-(DMSO-d6 capillary, 471 MHz, δ in ppm): −197.8, −210.8, −231.6 (s, 1N, *N*(SO$_2$)$_2$)).

^{19}F NMR (DMSO-d6 capillary, 471 MHz, δ in ppm): −120.9 (s, 4F, SC*F*$_2$), −127.4 (s, 2F, CC*F*$_2$C).

^{19}F NMR (acetone-d6, 377 MHz, δ in ppm): −120.6 (s, 4F, SC*F*$_2$), −126.9 (s, 2F, CC*F*$_2$C).

HRMS ((+)-ESI): *m/z* (isotropic abundance) for $C_8H_{15}N_2$ calcd.: 139.12 (100.0), 140.13 (8.8); found: 139.12 (100.0), 140.13 (8.9).

HRMS ((−)-ESI): *m/z* (isotropic abundance) for $C_3F_6NO_4S_2$: calcd.: 291.92 (100.0), 293.91 (9.0), 292.92 (5.0); found: 291.92 (100.0), 293.91 (9.3), 292.92 (3.1).

Elemental analysis calcd. (%) for $C_{11}H_{15}F_6N_3O_4S_2$: C 30.63, H 3.51, N 9.74, S 14.86; found: C 30.92, H 3.41, N 10.19, S 14.81.

[BMPL]4cPFSI

A solution of [BMPL]Cl (9.63 g, 54.2 mmol) in water (14 mL) and a solution of K**4cPFSI** (9.59 g, 41.5 mmol) in water (50 mL) were combined and stirred for 5 min. Dichloromethane (5 mL) was added to the mixture. The organic phase was separated and washed nine times with water (9 x 2 mL). The solvent of the organic phase was removed under reduced pressure. The residue was dried under vacuum while stirring for 24 h to result in 8.74 g of the title compound (26.1 mmol, 63% yield) as a colourless liquid.

^{1}H NMR (acetone-d6, 377 MHz, δ in ppm): 3.72 (m, 4H,ring NC*H*$_2$), 3.54 (m, 2H, chain NC*H*$_2$), 3.25 (s, 3H, NC*H*$_3$), 2.32 (m, 4H, ring NCH$_2$C*H*$_2$), 1.91 (m, 2H, chain NC*H*$_2$), 1.43 (m, 2H, CH$_3$C*H*$_2$), 0.98 (t, $^3J(^1H,^1H)$ = 7.31 Hz, C*H*$_3$CH$_2$).

^{13}C{^{1}H} NMR (acetone-d6, 101 MHz, δ in ppm): 134.0 (t, $^1J(^{19}F,^{13}C)$ = 367.4 Hz, 1C, *C*F$_2$), 65.2 (t, $^1J(^{14}N,^{13}C)$ = 3.2 Hz, 2C, ring N*C*H$_2$), 65.0 (t, $^1J(^{14}N,^{13}C)$ = 3.0 Hz, 1C, chain N*C*H$_2$), 49.0 (t, $^1J(^{14}N,^{13}C)$ =

4.1 Hz, 1C, N*C*H$_3$), 26.3 (s, 2C, ring NCH$_2$*C*H$_2$), 22.4 (s, 1C, chain NCH$_2$*C*H$_2$), 20.4 (m, 1C, *C*H$_2$CH$_3$), 14.1 (s, 1C, CH$_2$*C*H$_3$).

^{19}F NMR (acetone-d6, 377 MHz, δ in ppm): −89.5 (s, 2F).

HRMS ((+)-ESI): *m/z* (isotropic abundance) for $C_9H_{20}N$ calcd.: 142.16 (100.0), 143.16 (9.7); found: 142.16 (100.0), 143.162 (9.6).

HRMS ((−)-ESI): *m/z* (isotropic abundance) for $CF_2NO_4S_2$ calcd.: 191.92 (100.0), 193.92 (9.1), 192.92 (2.0); found: 191.92 (100.0), 193.92 (9.1), 192.92 (1.4).

Elemental analysis calcd. (%) for $C_{10}H_{20}F_2N_2O_4S_2$: C 35.92, H 6.03, N 8.38, S 19.17; found: C 36.29, H 6.17, N 8.68, S 19.19.

[BMPL]5cPFSI

[BMPL]Cl (4.05 g, 22.8 mmol) and K**5cPFSI** (5.02 g, 17.8 mmol) yielded 5.24 g of the title compound (13.6 mmol, 76% yield) as a pale beige liquid.

^{1}H NMR (DMSO-d6 capillary, 400 MHz, δ in ppm): 3.00 (m, 4H, ring NC*H$_2$*), 2.82 (m, 2H, chain NC*H$_2$*), 2.52 (s, 3H, NC*H$_3$*), 1.72 (m, 4H, ring NCH$_2$C*H$_2$*), 1.27 (m, 2H, CH$_3$CH$_2$C*H$_2$*), 0.91 (m, 2H, CH$_3$C*H$_2$*), 0.50 (t, ^3J(^{1}H,^{1}H) = 7.36 Hz, C*H$_3$*CH$_2$).

^{1}H NMR (acetone-d6, 400 MHz, δ in ppm): 3.68 (m, 4H, ring NC*H$_2$*), 3.49 (m, 2H, chain NC*H$_2$*), 3.20 (s, 3H, NC*H$_3$*), 2.29 (m, 4H, ring NCH$_2$C*H$_2$*), 1.87 (m, 2H, CH$_3$CH$_2$C*H$_2$*), 1.42 (m, 2H, CH$_3$C*H$_2$*), 0.97 (t, ^3J(^{1}H,^{1}H) = 7.36 Hz, C*H$_3$*CH$_2$).

^{13}C{^{1}H} NMR (DMSO-d6 capillary, 126 MHz, δ in ppm): 114.6 (tt, ^1J(^{19}F,^{13}C) = 307.0 Hz, ^3J(^{19}F,^{13}C) = 22.7 Hz, 2C, *C*$_2$F$_4$), 64.1 (m, 2C, chain N*C*H$_2$ and ring N*C*H$_2$), 47.9 (s, 1C, N*C*H$_3$), 25.2 (s, 2C, ring NCH$_2$C*H$_2$*), 19.2 (s, 1C, , *C*H$_2$CH$_3$), 12.8 (s, 1C, CH$_2$*C*H$_3$).

^{15}N NMR (DMSO-d6 capillary, 471 MHz, δ in ppm): −223.4.6 (s, 1N, *N*(SO$_2$)$_2$)), −308.23 (s, 1N, *N*CH$_3$).^{19}F NMR (DMSO-d6 capillary, 377 MHz, δ in ppm): −115.7 (s, 4F).

^{19}F NMR (acetone-d6, 377 MHz, δ in ppm): −115.8 (s, 4F).

HRMS ((+)-ESI): *m/z* (isotropic abundance) for $C_9H_{20}N$ calcd.: 142.159 (100.0), 143.162 (9.7); found: 142.159 (100.0), 143.162 (9.6).

HRMS ((−)-ESI): *m/z* (isotropic abundance) for $C_2F_4NO_4S_2$ calcd.: 241.92 (100.0), 243.917 (9.0); found: 241.921 (100.0), 243.916 (8.9).

Elemental analysis calcd. (%) for $C_{11}H_{20}F_4N_2O_4S_2$: C 34.37, H 5.24, N 7.29, S 16.68; found: C 34.62, H 5.40, N 7.55, S 16.61.

[BMPL]6cPFSI

A solution of [BMPL]Cl (3.16 g, 17.8 mmol) in water (6 mL) and a solution of H**6cPFSI** (3.99 g, 13.6 mmol) in water (4 mL) were combined and stirred for 20 min. Dichloromethane (1 mL) was added to the mixture. The organic phase was separated and washed nine times with water (9 x 2 mL). No halide was found then testing the pH-neutral last washing water with concentrated aqueous silver nitrate solution. The solvent of the organic phase was removed under reduced pressure. Drying the residue in high vacuum while stirring for 24 h yielded 5.13 g of the title compound (11.8 mmol, 87% yield) as colourless liquid.

^{1}H NMR (DMSO-d6 capillary, 400 MHz, δ in ppm): 2.89 (m, 4H, ring NCH_2), 2.72 (m, 2H, chain NCH_2), 2.42 (s, 3H, NCH_3), 1.61 (m, 4H, ring NCH_2CH_2), 1.17 (m, 2H, $CH_3CH_2CH_2$), 0.81 (m, 2H, CH_3CH_2), 0.39 (t, $^{3}J(^{1}H,^{1}H)$ = 7.35 Hz, CH_3CH_2).

^{1}H NMR (acetone-d6, 400 MHz, δ in ppm): 3.72 (m, 4H, ring NCH_2), 3.58 (m, 2H, chain NCH_2), 3.26 (s, 3H, NCH_3), 2.33 (m, 4H, ring NCH_2CH_2), 1.90 (m, 2H, $CH_3CH_2CH_2$), 1.46 (m, 2H, CH_3CH_2), 1.01 (t, $^{3}J(^{1}H,^{1}H)$ = 7.35 Hz, CH_3CH_2).

^{19}F NMR (DMSO-d6 capillary, 471 MHz, δ in ppm): −120.9 (s, 4F, SCF_2), −127.4 (s, 2F, CCF_2C).

^{19}F NMR (acetone-d6, 377 MHz, δ in ppm): −120.6 (s, 4F, SCF_2), −126.9 (s, 2F, CCF_2C).

^{13}C{^{1}H} NMR (DMSO-d6 capillary, 126 MHz, δ in ppm): 112.2 (tt, $^{1}J(^{19}F,^{13}C)$ = 298.4 Hz, $^{3}J(^{19}F,^{13}C)$ = 25.5 Hz, 2C, SCF_2), 108.9 (tp, $^{1}J(^{19}F,^{13}C)$ = 273.9 Hz, $^{3}J(^{19}F,^{13}C)$ = 25.7 Hz, 1C, CCF_2C), 64.4 (m, 2C, chain NCH_2 and ring NCH_2), 48.0 (s, 1C, NCH_3), 25.5 (s, 2C, ring NCH_2CH_2), 19.6 (s, 1C, , CH_2CH_3), 12.9 (s, 1C, CH_2CH_3).

^{13}C{^{1}H} NMR (acetone-d6, 101 MHz, δ in ppm): 114.6 (tt, $^{1}J(^{19}F,^{13}C)$ = 298.4 Hz, $^{3}J(^{19}F,^{13}C)$ = 25.6 Hz, 2C, SCF_2), 113.2 (tp, $^{1}J(^{19}F,^{13}C)$ = 273.9 Hz, $^{3}J(^{19}F,^{13}C)$ = 25.8 Hz, 1C, CCF_2C), 65.2 (m, 2C, chain NCH_2 and ring NCH_2), 48.7 (s, 1C, NCH_3), 26.2 (s, 2C, ring NCH_2CH_2), 19.8 (s, 1C, , CH_2CH_3), 13.0 (s, 1C, CH_2CH_3).

HRMS ((+)-ESI): *m/z* (isotropic abundance) for $C_9H_{20}N$ calcd.: 142.159 (100.0), 143.162 (9.7); found: 142.159 (100.0), 143.162 (9.7).

HRMS ((−)-ESI): *m/z* (isotropic abundance) for $C_3F_6NO_4S_2$: calcd.: 291.92 (100.0), 293.91 (9.0), 292.92 (5.0); found: 291.92 (100.0), 293.91 (9.1), 292.92 (3.9).

Elemental analysis calcd. (%) for $C_{12}H_{20}F_6N_2O_4S_2$: C 33.18, H 4.64, N 6.45, S 14.76; found: C 33.53, H 4.53, N 6.76, S 14.68.

References

1. C. B. Hübschle, G. M. Sheldrick and B. Dittrich, *J. Appl. Crystallogr.*, 2011, **44**, 1281-1284.
2. O. V. Dolomanov, L. J. Bourhis, R. J. Gildea, J. A. K. Howard and H. Puschmann, *J. Appl. Crystallogr.*, 2009, **42**, 339-341.
3. G. M. Sheldrick, *Acta Crystallographica Section A Foundations and Advances*, 2015, **71**, 3-8.
4. G. M. Sheldrick, *Acta Crystallographica Section C Structural Chemistry*, 2015, **71**, 3-8.
5. C. B. Hübschle, G. M. Sheldrick and B. Dittrich, *J. Appl. Crystallogr.*, 2011, **44**, 1281-1284.
6. K. Brandenburg, *Journal*, 2022.
7. P. R. Spackman, M. J. Turner, J. J. McKinnon, S. K. Wolff, D. J. Grimwood, D. Jayatilaka and M. A. Spackman, *J. Appl. Crystallogr.*, 2021, **54**, 1006-1011.
8. H. E. Gottlieb, V. Kotlyar and A. Nudelman, *J. Org. Chem.*, 1997, **62**, 7512-7515.
9. W. Kohn and L. J. Sham, *Physical Review*, 1965, **140**, A1133-A1138.
10. C. Adamo and V. Barone, *The Journal of Chemical Physics*, 1999, **110**, 6158-6170.
11. F. Weigend and R. Ahlrichs, *Physical Chemistry Chemical Physics*, 2005, **7**, 3297.
12. S. G. Balasubramani, G. P. Chen, S. Coriani, M. Diedenhofen, M. S. Frank, Y. J. Franzke, F. Furche, R. Grotjahn, M. E. Harding, C. Hättig, A. Hellweg, B. Helmich-Paris, C. Holzer, U. Huniar, M. Kaupp, A. Marefat Khah, S. Karbalaei Khani, T. Müller, F. Mack, B. D. Nguyen, S. M. Parker, E. Perlt, D. Rappoport, K. Reiter, S. Roy, M. Rückert, G. Schmitz, M. Sierka, E. Tapavicza, D. P. Tew, C. Van Wüllen, V. K. Voora, F. Weigend, A. Wodyński and J. M. Yu, *The Journal of Chemical Physics*, 2020, **152**, 184107.
13. K. Goloviznina, J. N. Canongia Lopes, M. Costa Gomes and A. A. H. Pádua, *Journal of Chemical Theory and Computation*, 2019, **15**, 5858-5871.
14. K. Goloviznina, Z. Gong and A. A. H. Padua, *WIREs Computational Molecular Science*, 2022, **12**.
15. K. Shimizu, D. Almantariotis, M. F. C. Gomes, A. A. H. Pádua and J. N. Canongia Lopes, *The Journal of Physical Chemistry B*, 2010, **114**, 3592-3600.
16. E. Heid, A. Szabadi and C. Schröder, *Physical Chemistry Chemical Physics*, 2018, **20**, 10992-10996.
17. A. A. H. Pádua, *The Journal of Chemical Physics*, 2017, **146**, 204501.
18. F. Philippi, D. Rauber, O. Palumbo, K. Goloviznina, J. McDaniel, D. Pugh, S. Suarez, C. C. Fraenza, A. Padua, C. W. M. Kay and T. Welton, *Chem. Sci.*, 2022, **13**, 9176-9190.
19. S. Plimpton, *Journal of Computational Physics*, 1995, **117**, 1-19.
20. M. Brehm and B. Kirchner, *Journal of Chemical Information and Modeling*, 2011, **51**, 2007-2023.
21. M. Brehm, M. Thomas, S. Gehrke and B. Kirchner, *The Journal of Chemical Physics*, 2020, **152**, 164105.
22. F. Philippi, K. Goloviznina, Z. Gong, S. Gehrke, B. Kirchner, A. A. H. Pádua and P. A. Hunt, *Physical Chemistry Chemical Physics*, 2022, **24**, 3144-3162.
23. S. Koutsoukos, F. Philippi, D. Rauber, D. Pugh, C. W. M. Kay and T. Welton, *Physical Chemistry Chemical Physics*, 2022, **24**, 6453-6468.
24. A. D. Bond, *Chem. Commun.*, 2003, DOI: 10.1039/b208904a, 250-251.
25. K. Vojinović, U. Losehand and N. W. Mitzel, *Dalton Trans.*, 2004, DOI: 10.1039/b405684a, 2578-2581.
26. M. T. Kirchner, D. Bläser and R. Boese, *Chemistry - A European Journal*, 2010, **16**, 2131-2146.
27. M. Bujak, H.-G. Stammler, S. Blomeyer and N. W. Mitzel, *Chem. Commun.*, 2019, **55**, 175-178.
28. M. A. Viswamitra and K. K. Kannan, *Nature*, 1966, **209**, 1016-1017.

29. M. Bujak, H.-G. Stammler and N. W. Mitzel, *Crystal Growth & Design*, 2020, **20**, 3217-3223.
30. G. H. Ralf Jüschke, Peter Sartori, *Z. Naturforsch.* , 1997, **52 b**, 359-366.